Title
On the interactions and phase behavior of indirect excitons in semiconductor materials

Author
Wrona, Paul Ryan

Publication Date
2022

Peer reviewed|Thesis/dissertation

On the interactions and phase behavior of indirect excitons in semiconductor materials

by

Paul R. Wrona

A dissertation submitted in partial satisfaction of the

requirements for the degree of

Doctor of Philosophy

in

Chemistry

in the

Graduate Division

of the

University of California, Berkeley

Committee in charge:

Professor Phillip L. Geissler, Co-chair
Professor Eran Rabani, Co-chair
Professor Joel E. Moore

Spring 2022

On the interactions and phase behavior of indirect excitons in semiconductor materials

Abstract

On the interactions and phase behavior of indirect excitons in semiconductor materials

by

Paul R. Wrona

Doctor of Philosophy in Chemistry

University of California, Berkeley

Professor Phillip L. Geissler, Co-chair

Professor Eran Rabani, Co-chair

Understanding the interactions of excitons has been central to the development of technologies such as solar cells and light-emitting diodes. To improve quantum yields and design materials with desired optoelectronic properties, researchers require an understanding of how multiple electron-hole pairs interact. From a fundamental perspective, excitons display rich phase behavior; as composite bosons, they can support both Bose-Einstein condensation as well as quantum Fermi liquids such as Keldysh's electron-hole liquid. Additionally, since they are analogous to hydrogen atoms, excitons can form molecules in the form of biexcitons and ions in the form of trions.

Recent studies on the interactions and phase behavior of excitons have considered indirect excitons whose constituents are constrained to reside in distinct planes separated by a distance d. By separating the electrons from the holes, both radiative and non-radiative recombination lifetimes are extended by orders of magnitude, making it easier to study and probe their equilibrium phase behavior. Additionally, indirect excitons possess permanent electric dipole moments, introducing a repulsion between particles. This interaction inhibits the formation of biexcitons and provides more favorable conditions for Bose-Einstein condensation. Furthermore, there is experimental and theoretical evidence for new emergent phases not previously observed when considering spatially-direct excitons, such as a classical liquid of individual excitons.

In this dissertation, we use a broad range of theoretical techniques to study the phase behavior of indirect excitons. First, we examine the interaction between two indirect excitons using diffusion Monte Carlo, finding long-range dipole-dipole repulsion in addition to short-range attraction for relatively small d. In order to study the effects of introducing a third exciton, we construct basis sets for indirect excitons and apply the full configuration interaction method, typically used for three-dimensional electronic systems. For very small d,

the lowest energy state of the triexciton is a weakly-bound exciton-biexciton van der Waals complex. Because the three-body potential is so weak and not pair-wise decomposable, we find no evidence for a driving force towards the classical condensation of indirect excitons.

In order to explain recent observations of a condensed phase of indirect excitons, we consider Keldysh's electron-hole liquid in a bilayer geometry. Working within the random-phase approximation, we calculate the ground state energy of a dense degenerate phase of unbound carriers, finding good agreement with experimental measurements. Taking the Green's-function approach to finite temperatures, we evaluate free energies for electrons and holes in a bilayer geometry using the linked-cluster expansion. By solving the law of mass action, we investigate how the exciton Mott transition from bound excitons to free carriers varies with d. Finally, using Maxwell equal-area constructions, we map the quantum liquid-gas phase diagram in the plane of temperature and total carrier density. These diagrams are in close agreement with the aforementioned experimental observations.

To all of my teachers.

"Tiger got to hunt, bird got to fly;
Man got to sit and wonder 'why, why, why?'
Tiger got to sleep, bird got to land;
Man got to tell himself he understand."
– Kurt Vonnegut, *Cat's Cradle*

Contents

List of Figures

List of Tables

Acknowledgments

Throughout my graduate studies, I have been fortunate enough to find an academic home in two groups. This means I have approximately twice as many people to thank as well as twice as many people to accidentally omit. There have been many colleagues and friends that have shaped my growth as a scientist and a human, and I sincerely thank everyone with whom I've crossed paths. I apologize if I forget to mention you by name.

First, I want to thank Professors Phill Geissler and Eran Rabani for their guidance and support. I have learned an incredible amount of physics and chemistry from both of them, and they have shaped the way I visualize and think about the complex and elegant microscopic world. I truly appreciate all of the lessons they have taught me and the scientific perspective they have shared. I especially thank Phill for the pedagogical knowledge he shared with me when I was his GSI for Chem220B. I am grateful for his feedback on my lecture and answers to my general questions surrounding teaching.

When I started my Ph.D., I found great role models from senior graduate students in both groups. In particular, I acknowledge John Philbin, Lyran Kidon, Layne Frechette, and Julia Rogers for helping me navigate the beginning of graduate school, teaching me random bits of science, and being great colleagues and friends. I also want to acknowledge the newer group members: Daniel Weinberg, Tommy Lin, Bokang Hou, Leopoldo Mejía, Srinath Ranya, Sam Oaks-Leaf, Katherine Delevaux, Amr Dodin, and Kritanjan Polley. They have made returning to the office post-COVID a pleasure, and I will sincerely miss the daily Pitzer Center lunches. I must also acknowledge Leslie Dietterick for keeping the Pitzer Center up and running, providing delicious home-made baked goods, and helping me ensure that I got paid correctly as I jumped from one funding source to another.

I want to thank my friends for always finding a way to make me laugh and reminding me to stop and smell the roses: Valerie McGraw ("m'lady"), the Pauli matrices (Dipti Jasrasaria, Elliot Rossomme, and Lucie Liu), Stephen Bierschenk, Collin Steen, Kaydren Orcutt, Eric Arsenault, Avishek Das, Jenna Tan, Zach Heim, Bryan Place, Isabel Bogacz, Elliot Martin, and Joey DeGrandchamp. I am particularly grateful to my partner Collin Steen. As both of us discovered, it can be difficult supporting a partner in graduate school, where the work hours can seem never-ending and the problems are rarely clearly defined. I am glad we found ways to encourage and inspire each other and keep each other sane. I was very lucky to have found a hard-working, kind, and loving partner such as Collin.

I must give a special shoutout to Dipti Jasrasaria, who has served as an incredible friend, colleague, and mentor. I deeply appreciate her support from a personal and professional side; I'm not sure if I would have finished graduate school without her. I am so impressed with how much she has accomplished in spite of her taking the time to help me with so many things. I look forward to seeing her further develop as a scientist, mentor, and role model to others, and I hope we can catch up over coffee and pumpkin cake every now and then.

Finally, from the bottom of my heart, thank you to my family, and especially my parents, for all of their support throughout graduate school and prior. I deeply appreciate everything they have taught, given, and done for me.

Chapter 1

Introduction

1.1 Excitons: fleeting and fascinating

Excitons, or bound electron-hole pairs, are observed in a diverse array of materials and are responsible for many important and compelling phenomena [1-2]. In semiconducting polymers, electronic excitations are typically localized to one chromophore- a region of several conjugated repeating units- and can "jump" to another through Förster energy transfer [3]. Within the light harvesting complexes of plants and algae, excitons transport optical energy absorbed by chromophores to the reaction center where energy is eventually stored in the form of chemical bonds [3]. Furthermore, in narrow-gap semiconductors or semimetals, if the exciton binding energy is larger than the band gap between the valence and conduction band, then the material will form an unconventional insulating ground state called an excitonic insulator [5-6].

Our understanding of excitons in semiconductors is responsible for the development of many important types of technology such as light-emitting diodes [7] and solar cells [8-9]. For instance, recent research on solar cells has focused on utilizing multiple exciton generation [10] as well as enhancing exciton diffusion lengths [11] to increase quantum efficiencies and/or output photocurrents. Other approaches have centered around minimizing non-radiative decay through applied strain [12] or simply by operating under low excitation power. In this latter case, the collection of excitons may be approximated by a low-density non-interacting gas. While this can yield high power conversion efficiencies, the amount of output power is low. One outstanding challenge in this field is how to support and effectively utilize a dense assembly of excitons. Thus, understanding how excitons interact individually and collectively can lead to better design principles.

Beyond the pragmatic technological advantages, excitons are fundamentally interesting, displaying fascinating properties, phenomena, and phases. Since an electron-hole pair is closely analogous to a hydrogen atom, two excitons can bind to form an excitonic molecule called a biexciton [13-14]. Similarly, an exciton and a free carrier can create hydrogenic ions called trions [15]. These composite species form with a high probability when thermal

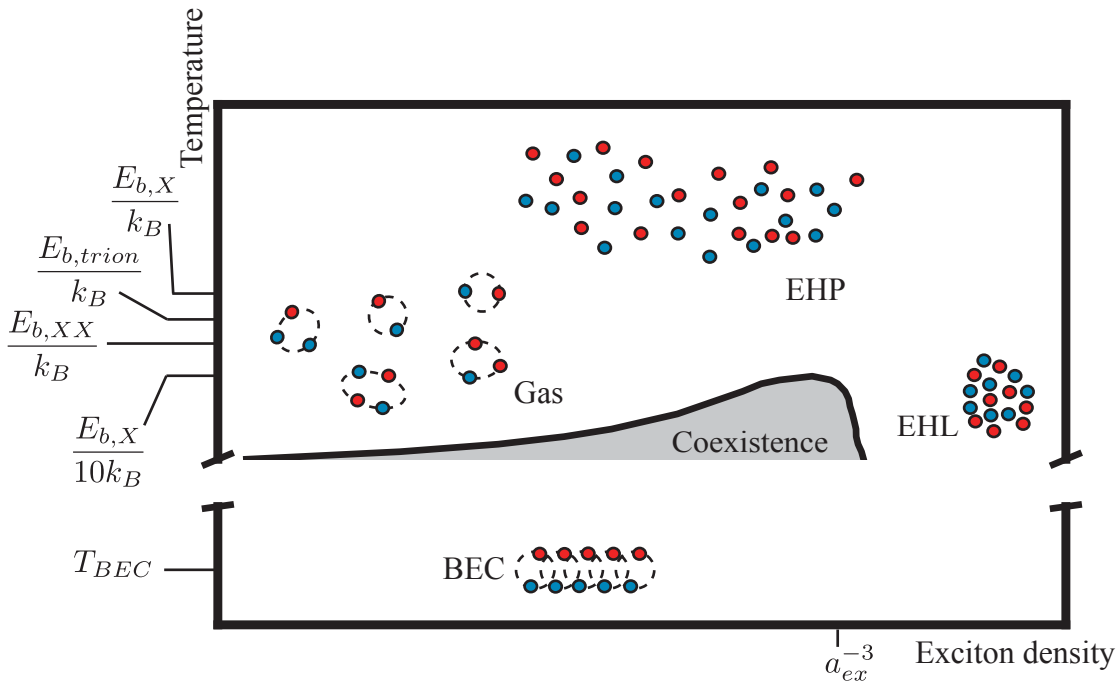

Figure 1.1: Sketch of a phase diagram for excitons in the density-temperature plane.

energy is less than their binding energy ($E_{b,X}$, $E_{b,trion}$, and $E_{b,XX}$ for excitons, trions, and biexcitons, respectively). These regimes are sketched in Figure 1.1. Transformations between these phases are not sudden, but rather continuous like the chemical equilibrium between hydrogen atoms and molecules. From their Stark effect [16] to their fine structure [17], excitons encompass the wealth of physics surrounding hydrogen.

At very low temperatures, the influence of quantum statistics becomes apparent. Unlike fermions (*e.g.*, electrons and holes), bosons (*e.g.*, excitons and biexcitons) do not obey an exclusion principle, allowing a macroscopic number of particles to occupy the same state and create a Bose-Einstein condensate (BEC). In three dimensions, the critical temperature for non-interacting bosons is [18]

$$T_{BEC} = \frac{3.31\hbar^2 n^{2/3}}{\xi^{2/3} m k_B} \tag{1.1}$$

where $\hbar$ is the reduced Planck constant, n is the density, ξ is the degeneracy of the lowest energy single-particle state, m is the particle's mass, and k_B is the Boltzmann constant. At first glance, one may expect experiments to operate at high excitation densities in order to raise this degeneracy temperature. However, excitons are stabilized by forming biexcitons with a larger mass, so in practice, the densities must be low enough such that the excitons are approximately non-interacting (see Figure 1.1). A BEC of excitons was first proposed a decade before a BEC of spin-aligned hydrogen atoms [19-20]. However, the hydrogenic BEC

was the first to be experimentally realized [21-23].

In the opposite regime, if thermal energy (*i.e.*, k_BT) is greater than the exciton binding energy, excitons dissociate and create an electron-hole plasma. Formation of this new phase occurs gradually when driven exclusively by thermal effects. However, this transformation can also occur suddenly if one increases the density and makes exchange and screening effects more significant. When the inter-exciton distance is on the order of the exciton's size (*e.g.*, the thermal de Broglie wavelength given in Eq. (3.104)), a first-order Mott transition can occur from a gas of bound excitons to an ionized fluid. Originally meant to describe the transition from an insulator to a metal under high doping concentrations [24], a modified form of this theory has successfully described this transition from an insulating exciton gas to a conductive electron-hole plasma.

Other phases have been predicted and subsequently observed in the intermediate regime between BECs and plasmas. As composite bosons, excitons display rich phase behavior characteristic of both bosons and fermions. At temperatures slightly above T_{BEC}, excitons can condense into a metallic electron-hole liquid (EHL). First hypothesized by L. V. Keldsyh in 1968 [25], this degenerate state is stabilized by exchange and screening effects [26]. Experiments in the following decades revealed some of its intriguing properties, such as high mobility, simple mechanical control through applied stress, and quantized droplets [27-31]. Figure 1.1 shows the coexistence region for the EHL and gas. For many materials and geometries [32-33], the critical temperature is

$$T_C \approx \frac{0.1E_{b,X}}{k_B} \tag{1.2}$$

Above the critical point lies a supercritical fluid phase: the electron-hole plasma.

Perhaps the biggest complication involved in studying the equilibrium phase behavior of excitons is their finite lifetime. One way to extend their recombination lifetimes is by creating indirect excitons (IXs) whose constituents are located in different regions of space. To separate the attractive carriers, one can utilize electric fields [34] or a type-II band alignment [35]. As shown in Figure 1.2, coupled quantum wells (CQW) use the former to confine carriers to separate quantum wells. In doing so, the excitons acquire permanent dipole moments proportional to the quantum wells' separation, d, drastically changing their interactions and collective behavior. With their extended lifetimes and mutual repulsion, indirect excitons have been observed to traverse distances orders of magnitude larger than their size [36]. Furthermore, a number of novel exciton phases have been proposed, such as a spin-density wave [37], a crystal [38-39], and a high-temperature superfluid [40].

One of the most interesting hypothesized phases of indirect excitons is a classical (*i.e.*, non-degenerate) liquid [41]. This state is impossible to assemble with spatially-direct excitons as they are stabilized in the form of biexcitons. However, the dipole moments of IXs weaken the exciton-exciton bond, opening up the possibility of a liquid of individual excitons. Recent experiments conducted by Bar-Joseph and co-workers studied the phase diagram of indirect excitons in GaAs at intermediate temperatures: a few degrees above T_{BEC} [42-43]. Below a critical temperature and above a threshold laser power, they observed a phase boundary

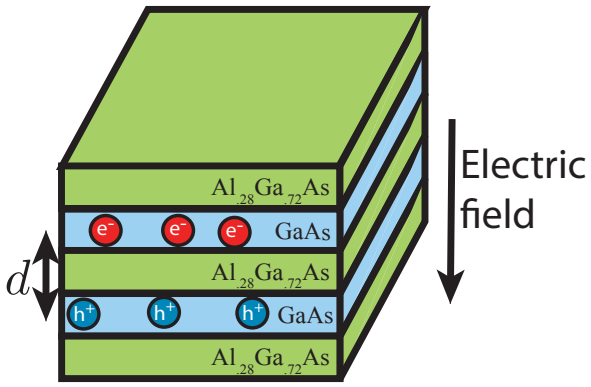

Figure 1.2: Schematic of a coupled quantum well. d is the separation between the centers of the quantum wells.

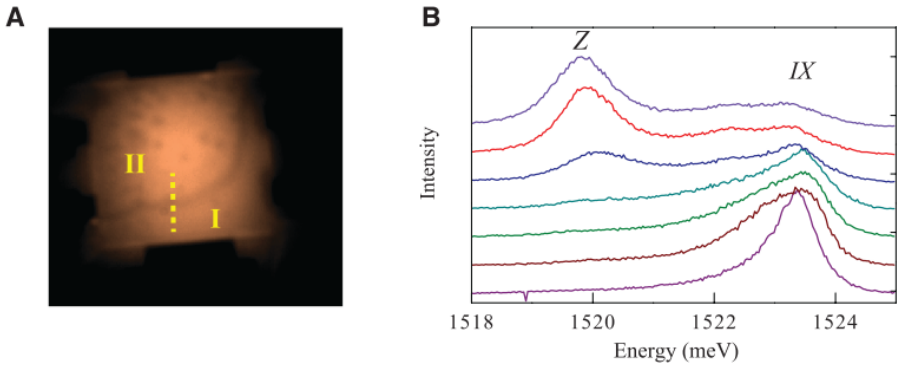

Figure 1.3: The left panel is a photoluminescence image of coupled quantum wells from a top-down view. The right panel consists of spatially-resolved spectra taken across the dashed yellow line shown in the image. Region I contained the emission from indirect excitons (IX) and was interpreted as a gas of IXs. Region II featured a red-shifted peak (Z) and was interpreted as a classical liquid of IXs [42,43].

in their photoluminescence (PL) images (see Figure 1.3). By acquiring spatially-resolved PL spectra across the boundary, they noticed that the emission from the new phase was red-shifted by 4 meV. The authors interpreted this state as a classical liquid of IXs. In contrast, earlier studies concluded that a high-density IX phase was Keldysh's electron-hole liquid realized in a bilayer geometry [44-45]. Indeed, others have cast doubt on the validity of the classical liquid of IXs [46], but there has been little concrete evidence for or against this newly considered phase thus far.

In this dissertation, we investigate the stability of various phases of indirect excitons. In the remainder of this chapter, we establish the overarching theoretical framework. We

first consider the possibility of a classical liquid of indirect excitons in Chapter 2. Classical liquids are typically stabilized by attractive interactions, so we first seek an attraction among multiple IXs. Additionally, we investigate whether there is any regime of quantum well separations d in which the many-body potential can be approximately decomposed as a sum of two-body pair potentials. We begin by reviewing diffusion Monte Carlo studies of the interactions between two IXs. In order to study a third IX, we borrow techniques from quantum chemistry and extend the full configuration interaction method from three-dimensional electronic systems to bilayer excitonic systems. We ultimately find no evidence of a driving force towards the classical condensation of indirect excitons in realistic CQWs.

In Chapter 3, we apply field theoretic techniques to study Keldysh's electron-hole liquid in a bilayer geometry. We find that the energy difference between a gas of excitons and the electron-hole liquid is approximately equal to the red-shift measured in [42]. Encouraged by this result, we then calculate free energies and chemical potentials for a collection of degenerate electrons and holes and identify instabilities which prompt a transition to a condensed state.

In Chapter 4, we synthesize the results of Chapters 2 and 3 to study the effects of electrons and holes binding to form excitons and determine how the exciton Mott transition depends on the distance between quantum wells, d. Finally, we use Maxwell equal-area constructions to map the liquid-gas phase diagram for indirect excitons and analyze how the critical point varies with d as well as the electron-hole mass ratio.

1.2 Overarching theoretical framework

Excitons are difficult to study theoretically since they are bound states of quasielectrons and quasiholes [47]. A rigorous approach to calculating the properties of these latter primary elementary excitations involves solving for the many-body one-particle Green's function [48]. Then, to incorporate the quasielectron and quasihole interaction, one solves the Bethe-Salpeter equation for the two-particle Green's function [49]. This framework has successfully described Auger recombination [50] and exciton-phonon coupling [51] in semiconductor nanostructures. However, due to their complexity and computational cost, these methods have been restricted to studying phenomena involving at most two excitons [52].

In light of this, we work within the effective mass approximation [47]. Because we are interested in thermally-equilibrated states located at the band edge, we are safe in assuming a parabolic band structure. Specifically, we consider isotropic conduction and valence bands and take the effective masses for electrons and holes in GaAs to be $m_e = 0.063m_0$ and $m_h = 0.51m_0$ respectively, where m_0 is the rest mass of the electron. Because we assume a single conduction and valence band, the system is symmetric under the exchange of electron and hole masses. That is, two systems with electron-hole mass ratios $\sigma = m_e/m_h$ and σ^{-1} are equivalent. Without loss of generality, we restrict our studies to $0 \leq \sigma \leq 1$.

We use excitonic units throughout this dissertation. Our length scale is the exciton Bohr

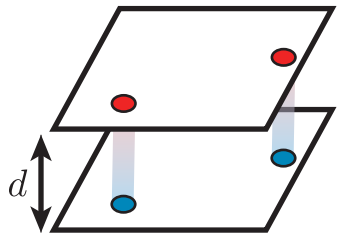

Figure 1.4: Bilayer model with the bilayer separation d indicated.

radius

$$a_{ex} = \frac{4\pi\epsilon_0\epsilon\hbar^2}{m_{red}e^2} \tag{1.3}$$

$$= \frac{\epsilon m_0}{m_{red}} a_0 \tag{1.4}$$

$$\approx 12\text{nm} \quad \text{GaAs} \tag{1.5}$$

where ϵ_0 is the vacuum permittivity, ϵ is the static dielectric constant (12.9 for GaAs), $m_{red}^{-1} = m_e^{-1} + m_h^{-1}$ is the electron-hole reduced mass, e is the elementary charge, and a_0 is the Bohr radius. Similarly, our energy scale is the exciton Rybderg

$$Ry_{ex} = \frac{m_{red}e^4}{2(4\pi\epsilon_0\epsilon)^2\hbar^2} \tag{1.6}$$

$$= \frac{e^2}{2(4\pi\epsilon_0\epsilon)a_{ex}} \tag{1.7}$$

$$= \frac{m_{red}}{\epsilon^2 m_0} Ry \tag{1.8}$$

$$\approx 5\text{meV} \quad \text{GaAs} \tag{1.9}$$

where Ry is the Rydberg constant.

We follow most theoretical work on indirect excitons by approximating coupled quantum wells with an ideal bilayer model shown in Figure 1.4. Here, the electron and hole planes are assumed to be infinitely thin, thus neglecting fluctuations in the transverse direction. As hinted by their name, the widths of most quantum wells are smaller than $1a_{ex}$, so the carriers experience quantum confinement effects. To a good approximation, the wavefunction in the z-direction is given by the ground state of a particle-in-a-box, whose probability density is largest at the center of the wells. Indeed, exact numerical calculations of an exciton in a realistic coupled quantum well system reveal that the carriers are predominantly located at the center of the wells, even under the influence of an electric field [53]. Thus, we will map the bilayer separation d to the separation between the wells' centers.

Chapter 2

Few-body interactions of indirect excitons

2.1 Introduction

In this Chapter we consider the possibility of a classical liquid of indirect excitons as hypothesized in [41-43]. By classical we mean that the excitons are non-degenerate, so their typical separation from each other is larger than their thermal de Broglie wavelength. A necessary ingredient in forming a condensed, non-crystalline phase is an attractive force among particles.[1] A distinguishing feature of indirect excitons is their permanent electric dipole moment. As bound excitons are charge-neutral, their dipole moments dictate their long-range electrostatic interaction. Since these moments are aligned in the same direction as one another, IXs are purely repulsive on the basis of classical electrostatics. Due to the overwhelming evidence of an attraction between two indirect excitons [54-57], we must examine the problem quantum mechanically.

Even within the simplifying framework of the effective mass approximation, it remains difficult to compute the interactions between two excitons due to their composite nature. Okumura and Ogawa [58] were the first to study the so-called "composite-particle effect," or the deviation of an exciton's statistics from that of an ideal boson. Using second-quantization, they derived a bosonized Hamiltonian and computed interaction potentials for two excitons, noting that "these interaction potentials agree with the result of the Heitler-London theory" [58]. Building on this work, Schindler and Zimmermann [55] calculated spin-dependent potentials for two-dimensional and bilayer systems using the Heitler-London approximation in addition to solving the Schrödinger equation numerically with the Lanczos algorithm. This latter approach gave improved results, but required them to treat the holes as infinitely massive.

[1] It is well-known that a collection of hard spheres in three dimensions crystallizes at high densities. The situation is murkier in lower dimensions due to the Mermin-Wagner theorem, which states that continuous symmetries cannot be spontaneously broken in one or two dimensions. While this prohibits the existence of a crystal with long-range positional order, there is evidence of a hexatic phase with orientational order.

The most accurate studies of two indirect excitons utilize diffusion Monte Carlo (DMC) [56,59]. This method yields the ground state wavefunction and energy by solving the imaginary-time Schrödinger equation by propagating Monte Carlo "walkers" according to a diffusion-like equation. These walkers sample the wavefunction like a probability distribution, which is valid for positive-definite, nodeless wavefunctions. Because there are only two electrons and two holes in a biexciton, the ground state spin configuration for both the electrons and holes is a singlet and DMC is exact in principle. In practice, statistical error is accrued due to sampling the wavefunction, but this can be minimized by biasing the walkers according to a guiding or trial function. While the final energy and wavefunction are independent of the trial function, the statistical errors are significantly reduced using an appropriate function. Additionally, DMC is exact in the limit that the propagation time step $d\tau$ goes to zero; in practice one first calculates the desired observable using multiple time steps and then extrapolates to $d\tau = 0$.

2.2 Diffusion Monte Carlo studies of two indirect excitons

The Hamiltonian in atomic units ($\hbar = e = m_0 = 4\pi\epsilon_0 = 1$) for two indirect excitons is

$$H = -\frac{1}{2m_e}\left(\nabla_1^2 + \nabla_2^2\right) - \frac{1}{2m_h}\left(\nabla_a^2 + \nabla_b^2\right) + \frac{1}{\epsilon|\mathbf{r}_1 - \mathbf{r}_2|} + \frac{1}{\epsilon|\mathbf{r}_a - \mathbf{r}_b|} - \sum_{i=1,2}\sum_{\alpha=a,b}\frac{1}{\epsilon\sqrt{|\mathbf{r}_i - \mathbf{r}_\alpha|^2 + d^2}} \tag{2.1}$$

1 and 2 refer to the electrons, and a and b refer to the holes. The first four terms are the kinetic energy of the electrons and holes, the next two terms are the statically-screened Coulomb repulsion between identical particles, and the last four terms are the statically-screened Coulomb attraction between dissimilar particles. All vectors are two-dimensional.

Following [56], we solved Eq. (2.1) using DMC with a trial wavefunction of

$$\psi_T(\mathbf{r}_{e1}, \mathbf{r}_{e2}, \mathbf{r}_{h1}, \mathbf{r}_{h2}) = \exp[-|\mathbf{r}_{e1} - \mathbf{r}_{h1} + d\hat{z}|]\exp[-|\mathbf{r}_{e2} - \mathbf{r}_{h2} + d\hat{z}|]\exp[-|\mathbf{r}_{e1} - \mathbf{r}_{h2} + d\hat{z}|] \times \exp[-|\mathbf{r}_{e2} - \mathbf{r}_{h1} + d\hat{z}|]\exp\left[\frac{0.5|\mathbf{r}_{e1} - \mathbf{r}_{e2}|}{1 + |\mathbf{r}_{e1} - \mathbf{r}_{e2}|}\right]\exp\left[\frac{0.5|\mathbf{r}_{h1} - \mathbf{r}_{h2}|}{1 + |\mathbf{r}_{h1} - \mathbf{r}_{h2}|}\right] \tag{2.2}$$

The first four terms are inspired by the exciton ground state wavefunction (an exponential), and the last two terms are Jastrow factors. The latter factors incorporate electron-electron and hole-hole correlations, and they obey the Kato cusp condition [60-61] which guarantees that the Hamiltonian is non-singular when two electrons or holes coalesce.

Upon solving Eq. (2.1) for the 4-particle biexciton energy E_{XX}, we compute the biexciton binding energy

$$E_{b,XX} = 2E_X - E_{XX} \tag{2.3}$$

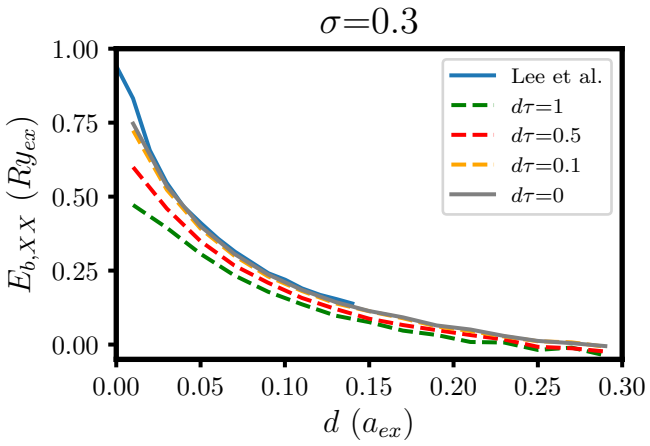

Figure 2.1: Biexciton binding energy $E_{b,XX}$ as a function of the bilayer separation d. The electron-hole mass ratio is $\sigma = m_e/m_h = 0.3$. Lee *et al.* comes from [56].

where E_X is the ground state energy of a single indirect exciton. In [59], Needs and co-workers computed $E_X(d)$ as a function of the bilayer separation d by solving the radial the Schrödinger equation for an IX:

$$-\frac{1}{r}\frac{\partial}{\partial r}\left(r\frac{\partial \Phi}{\partial r}\right) - \frac{2}{\sqrt{r^2+d^2}}\Phi = E_X\Phi \tag{2.4}$$

When $d = 0$, the equation can be solved exactly to give $E_X(0) = -4Ry_{ex}$. For $d > 0$, they used 4^{th} Runge-Kutta integration to solve Eq. (2.4). The result was fit to

$$E_X = -\frac{4 + Ad + Bd^2 + Cd^3}{1 + Dd + Ed^2 + Fd^3 + Gd^4} \tag{2.5}$$

where A=154.363, B=648.9, C=225.005, D=46.4263, E=384.976, F=628.158, and G=129.672. This fit gives a maximum error of $0.0028Ry_{ex}$. When expressed in Ry_{ex}, E_X is independent of the electron-hole mass ratio $\sigma = m_e/m_h$. Figure 2.1 shows how the biexciton binding energy changes with the bilayer separation. Multiple time steps are shown in addition to the extrapolated $d\tau = 0$ result. As expected, the binding energy decreases as the electrons and holes are increasingly separated from each other. We can equivalently attribute this destabilization to the growing dipole moments of the indirect excitons.

By identifying the bilayer separation where $E_{b,XX} = 0$ for various d and σ, Lee *et al.* mapped the region of biexciton stability shown in Figure 2.2. Indirect biexcitons are the most stable when $\sigma = 0$. When the holes are infinitely-massive classical point charges, the electrons can localize around them which increases the electron-hole attraction while decreasing electron-electron and hole-hole repulsion.

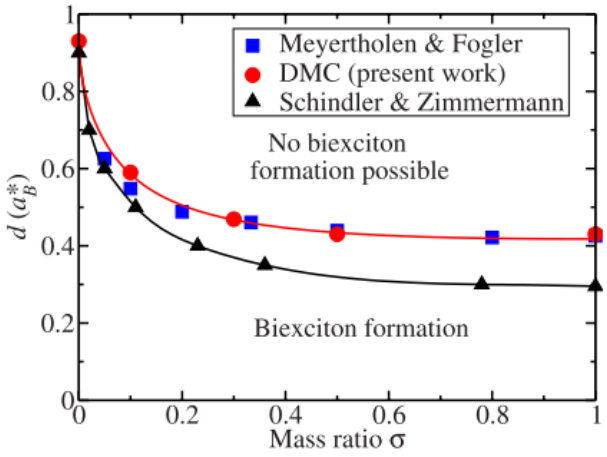

Figure 2.2: Region of biexciton stability from [56].

To calculate the interaction potential between two indirect excitons, Needs and co-workers [56] transformed Eq. (2.1) into

$$H = -\frac{1}{2m_{red}}\left(\nabla_{X1}^2 + \nabla_{X2}^2\right) + \frac{1}{\epsilon|\mathbf{R} + \frac{m_{red}}{m_e}\left(\mathbf{r}_{X1} - \mathbf{r}_{X2}\right)|} + \frac{1}{\epsilon|\mathbf{R} + \frac{m_{red}}{m_h}\left(\mathbf{r}_{X2} - \mathbf{r}_{X1}\right)|} - \frac{1}{\epsilon r_{X1}} - \frac{1}{\epsilon r_{X2}} - \frac{1}{\epsilon|\mathbf{R} - \frac{m_{red}}{m_h}\mathbf{r}_{X1} - \frac{m_{red}}{m_e}\mathbf{r}_{X2}|} - \frac{1}{\epsilon|\mathbf{R} + \frac{m_{red}}{m_e}\mathbf{r}_{X1} + \frac{m_{red}}{m_h}\mathbf{r}_{X2}|} \tag{2.6}$$

where $\mathbf{r}_{X1(X2)}$ is the electron-hole separation for exciton 1 (2) and $\mathbf{R}$ is the separation between the excitons' centers-of-mass. In this form, $R = |\mathbf{R}|$ can be treated as a fixed parameter, allowing one to evaluate the biexciton energy as a function of the exciton-exciton separation. Since the electrons are distinguished in these coordinates, this transformation is only valid for relatively large R where the excitons remain bound.

To compute accurate interaction potentials, especially in the limit of large d, we require a more accurate trial wavefunction than Eq. (2.2). In this case, we used

$$\psi_T = \psi_{ee}\psi_{hh}\psi_{eh} \tag{2.7}$$

where

$$\psi_{ee} = \exp\left[\frac{c_1 r_{12}}{1 + c_2 r_{12}}\right] \tag{2.8}$$

$$\psi_{hh} = \exp\left[\frac{c_3 r_{ab}}{1 + c_4 r_{ab}}\right] \tag{2.9}$$

$$\psi_{eh} = \exp\left[\frac{c_5 r_{1a} + c_6 r_{1a}^2}{1 + c_7 r_{1a}} + \frac{c_5 r_{1b} + c_8 r_{1b}^2}{1 + c_9 r_{1b}} + \frac{c_5 r_{2a} + c_8 r_{2a}^2}{1 + c_9 r_{2a}} + \frac{c_5 r_{2b} + c_6 r_{2b}^2}{1 + c_7 r_{2b}}\right] + \exp\left[\frac{c_5 r_{1a} + c_8 r_{1a}^2}{1 + c_9 r_{1a}} + \frac{c_5 r_{1b} + c_6 r_{1b}^2}{1 + c_7 r_{1b}} + \frac{c_5 r_{2a} + c_6 r_{2a}^2}{1 + c_7 r_{2a}} + \frac{c_5 r_{2b} + c_8 r_{2b}^2}{1 + c_9 r_{2b}}\right] \tag{2.10}$$

Eq. (2.2) is recovered if $c_1 = c_3 = 0.5$, $c_2 = c_4 = 1$, $c_5 = -1$, and $c_6 = c_7 = c_8 = c_9 = 0$. We optimized these variational parameters using variational Monte Carlo within the CASINO program [62].

The exciton-exciton interaction potential is defined as

$$V_{X-X}(R) = E_{XX}(R) - 2E_X \tag{2.11}$$

Figure 2.3 shows an interaction potential for $d = 0.6a_{ex}$ and $\sigma = 0$ after extrapolating to $d\tau = 0$. When the excitons are far from each other, their interaction is described by classical electrostatics. Since they do not have a net charge, their interaction to lowest order is dipole-dipole. In excitonic units,

$$V_{X-X}(R) = \frac{2d^2}{R^3} \quad R \gg 1a_{ex} \tag{2.12}$$

This interaction is shown in dotted lines. Figure 2.4 shows the heavy-hole two-body interaction potentials for $d = 0.8$ and $0.9a_{ex}$. At these large values of d, the well depth is on the order of 10^{-3}–$10^{-2}Ry_{ex}$, and the equilibrium separation between the excitons is extended to $3a_{ex}$.

Because the electron and hole effective masses are less than the rest mass of an electron, there are significant zero-point effects. This causes the true exciton-exciton binding energy to be less than the well depth (*i.e.*, the minimum value) of V_{X-X}. If we naively assume that interaction potentials are independent of the electron-hole mass ratio, we can use heavy-hole ($\sigma = 0$) potentials to estimate the change in biexciton binding energy. Figure 2.5 shows a fit of the $d = 0$ heavy-hole potential to the Morse potential

$$V(r) = D(1 - \exp[-a * r])^2 - D \tag{2.13}$$

Setting the dissociation energy to the zero-point energy [63],

$$D = \sqrt{\frac{2D}{m_{red}}}\frac{a}{2} - \frac{a^2}{8m_{red}} \tag{2.14}$$

We solve this equation to find the smallest reduced mass m_{red} that yields bound states of the Morse oscillator. Following this procedure for various d and finding the σ at which excitons remain bound, we map biexciton stability and compare it in Figure 2.6 to the previous DMC results. Using the $\sigma = 0$ potentials causes us to overestimate the region of stability, but the agreement is still quite good.

What do these indirect exciton pair potentials imply for the experiments of [42,43,45] which observe a condensed phase of IXs? The coupled quantum wells under investigation

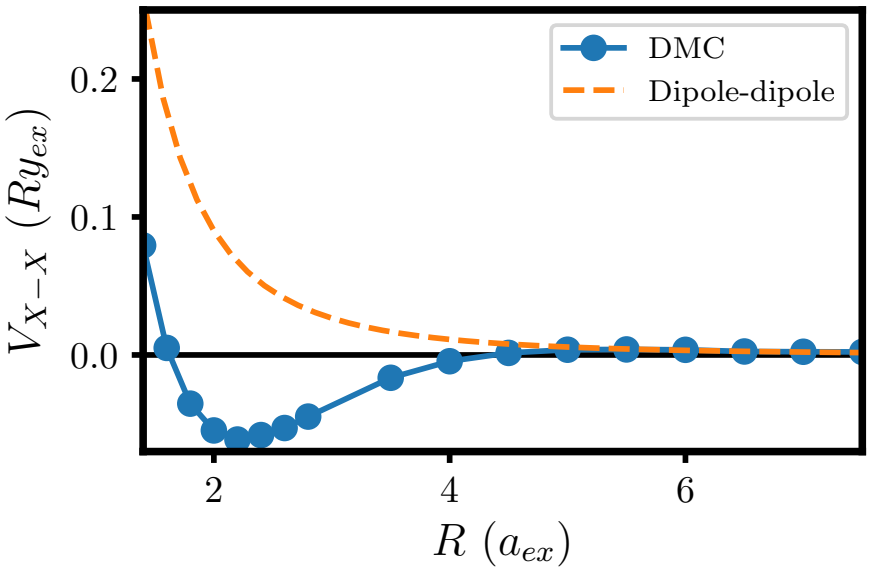

Figure 2.3: Exciton-exciton interaction potential for $d = 0.6$ and $\sigma = 0$ calculated using DMC. Shown in the dotted line is the dipole-dipole repulsion given by Eq. (2.12).

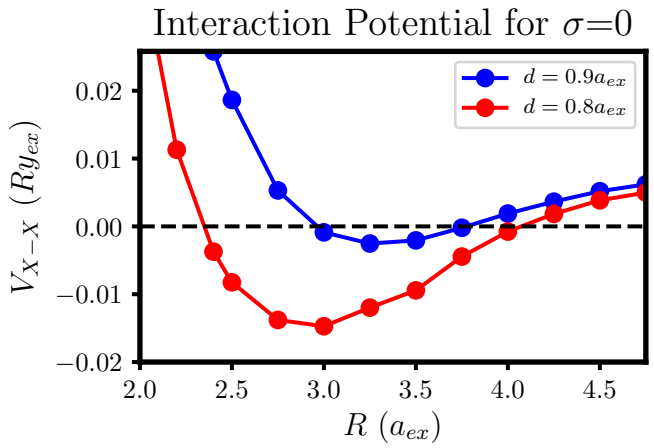

Figure 2.4: Interaction potentials for $d = 0.8$ and 0.9 a_{ex} and $\sigma = 0$ using DMC.

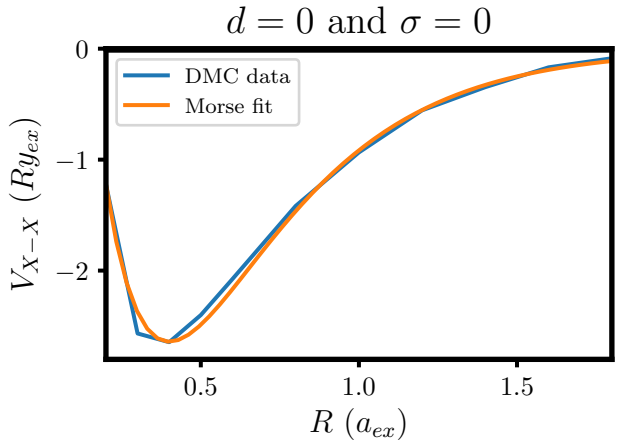

Figure 2.5: Exciton-exciton interaction potential $V_{X-X}(R)$ for $d = 0$ and $\sigma = 0$ calculated using DMC. Also shown is a fit to the Morse potential, Eq. (2.13).

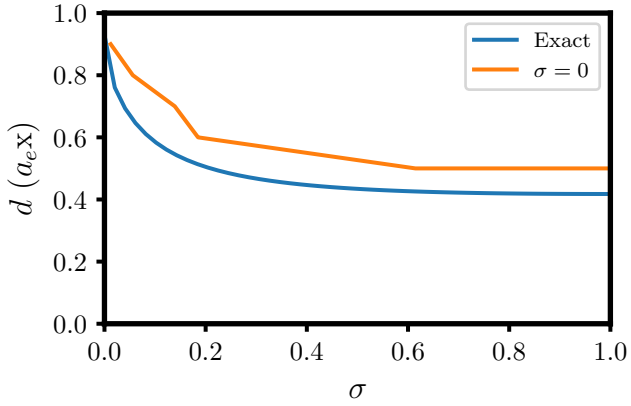

Figure 2.6: Critical bilayer separation for bound biexcitons as a function of electron-hole mass ratio. "Exact" refers to diffusion Monte Carlo calculations for two electrons and 2 holes. "$\sigma = 0$" refers to diffusion Monte Carlo calculations for 2 electrons with infinitely heavy holes. See main text for more details.

have a center-to-center well separation of $d \geq 1a_{ex}$. Although the carriers of a single indirect exciton are most likely found in the centers of the wells [53], it is possible that interactions with other indirect excitons lead to the carriers being pulled closer to one another. The electron-hole mass ratio for GaAs is $\sigma \approx 0.1$, so the effective bilayer separation must be cut in half ($d < 0.6a_{ex}$ according to Figure 2.6) in order to observe any attraction between two indirect excitons.

Furthermore, there is no reason to believe that the many-body potential is pair-wise decomposable. In three and two dimensions ($d = 0$), the ground state of three hydrogen atoms is a van der Waals complex consisting of a hydrogen molecule and an atom; two atoms are strongly bound in close proximity due to their covalent bond and the third is loosely held a large distance away. Since the hydrogenic analogy breaks down for $d \neq 0$, it is possible that the indirect excitons' dipole moments inhibit the exchange interaction which underlies the "excitonic bond." While we doubt that the aforementioned experiments observe a classical liquid of excitons as they investigate large quantum well separations, it remains fundamentally interesting and significant if there is some regime of bilayer separations for which the many-body potential is accurately described by a pair-decomposable form. Therefore, we wish to calculate the three-body interaction potential for indirect excitons.

Unfortunately, diffusion Monte Carlo is no longer exact when applied to systems whose wavefunctions have nodes such as triexcitons. However, this method can provide insight into how to further proceed. In addition to obtaining the ground state energy, diffusion Monte Carlo also yields the ground state wavefunction. Figure 2.7 shows biexciton electronic probability distributions projected along the hole-hole axis for $\sigma = 0$ and $d = 0.9$. When the holes are far apart ($R = 4.5a_{ex}$), the electronic distribution is peaked directly above the holes. However, as R decreases, the electrons are pulled inwards towards the other hole, reminiscent of the formation of a covalent bond. In a hydrogen molecule, the electrons are shared between both nuclei. As the electrons delocalize over both nuclei, the electron-nuclear attraction increases and the electrons' kinetic energy decreases. Molecular orbital theory describes this delocalization using linear combinations of atomic orbitals.

To test if indirect biexciton formation can be captured by an orbital-based approach, we first obtained the wavefunction for a single exciton. Figure 2.8 shows the corresponding electronic density projected along the x-axis for $d = 0.9a_{ex}$. We then added together two exciton wavefunctions centered above the holes and computed the resulting electronic distribution. In Figure 2.9, we compare the exact biexciton electronic distribution to the sum of two non-interacting exciton states. Surprisingly, we find quite good agreement, suggesting that this orbital picture can accurately describe the interactions between excitons, even for $d \neq 0$. Moving forward, we will push the exciton-hydrogen atom analogy as far as possible.

2.3 Building a Gaussian basis for indirect excitons

Since diffusion Monte Carlo samples the ground state wavefunction like a probability distribution, the method is best suited for systems with nodeless wavefunctions, such as those

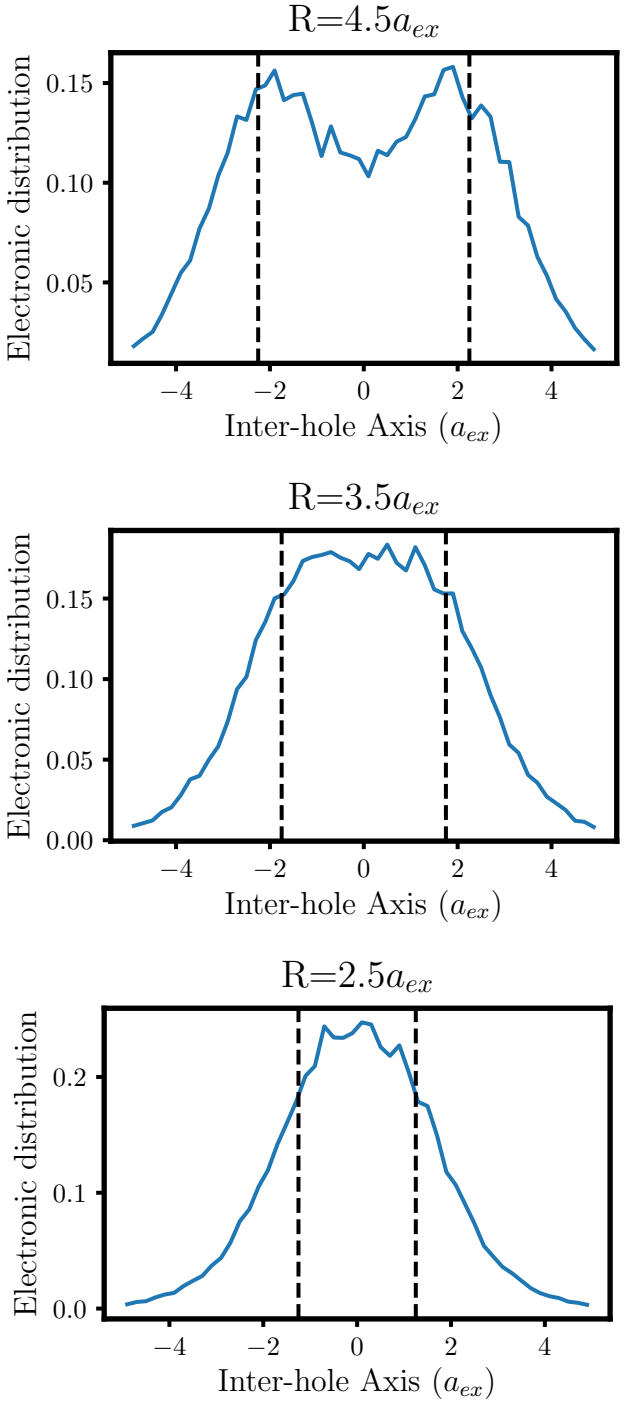

Figure 2.7: Plots of electronic density projected along the hole-hole axis for $\sigma = 0$, $d = 0.9a_{ex}$ and three different hole-hole separations. Dashed lines show placement of the holes on the lower plane.

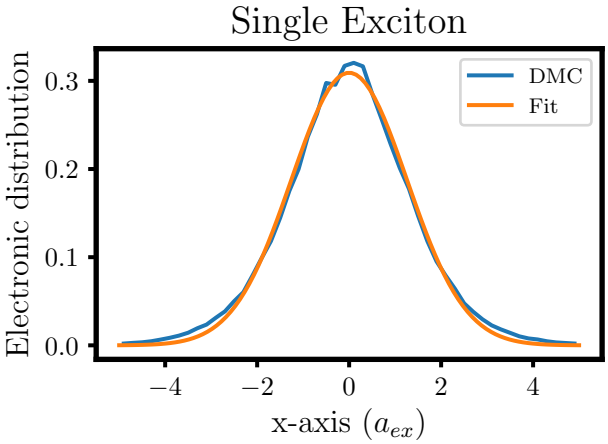

Figure 2.8: Single exciton wavefunction for $d = 0.9$ and $\sigma = 0$. The fit is to a Gaussian with zero mean and a variance of $1.583 a_{ex}^2$.

with two electrons (and/or two holes). DMC can be applied to systems with more electrons if one invokes approximations like the fixed-node approximation [64], but these depend on the quality of the trial wavefunction. Over the past several decades, quantum chemists have developed a plethora of techniques to solve the Schrödinger equation for molecules with many electrons. These have relied on building many different three-dimensional atomic basis sets. Even for the slightly more common case of a strictly two-dimensional ($d = 0$) system, there are no commonly-used basis sets.

Because we're interested in multiple indirect excitons residing in a variety of bilayer separations, we must first solve the single IX Hamiltonian (in atomic units)

$$H = -\frac{1}{2m_{red}}\nabla^2 - \frac{1}{\epsilon\sqrt{r^2 + d^2}} \tag{2.15}$$

where r is a two-dimensional vector describing the lateral separation between the electron and hole. When $d = 0$, the system is equivalent to the hydrogen atom; the ground state energy is $-4Ry_{ex}$ and the corresponding normalized eigenstate is

$$\phi_{d=0}(r) = \sqrt{\frac{2}{\pi}}\exp[-r] \tag{2.16}$$

For $d \neq 0$, the Hamiltonian does not appear to be analytic.

From Figure 2.8, the electronic density of an indirect exciton for relatively large d is well-described by a single Gaussian. As a first approach, we solve Eq. (2.15) variationally using

$$g(r;\sigma^2) = \frac{1}{\sqrt{\pi\sigma^2}}\exp\Big[-\frac{r^2}{2\sigma^2}\Big] \tag{2.17}$$

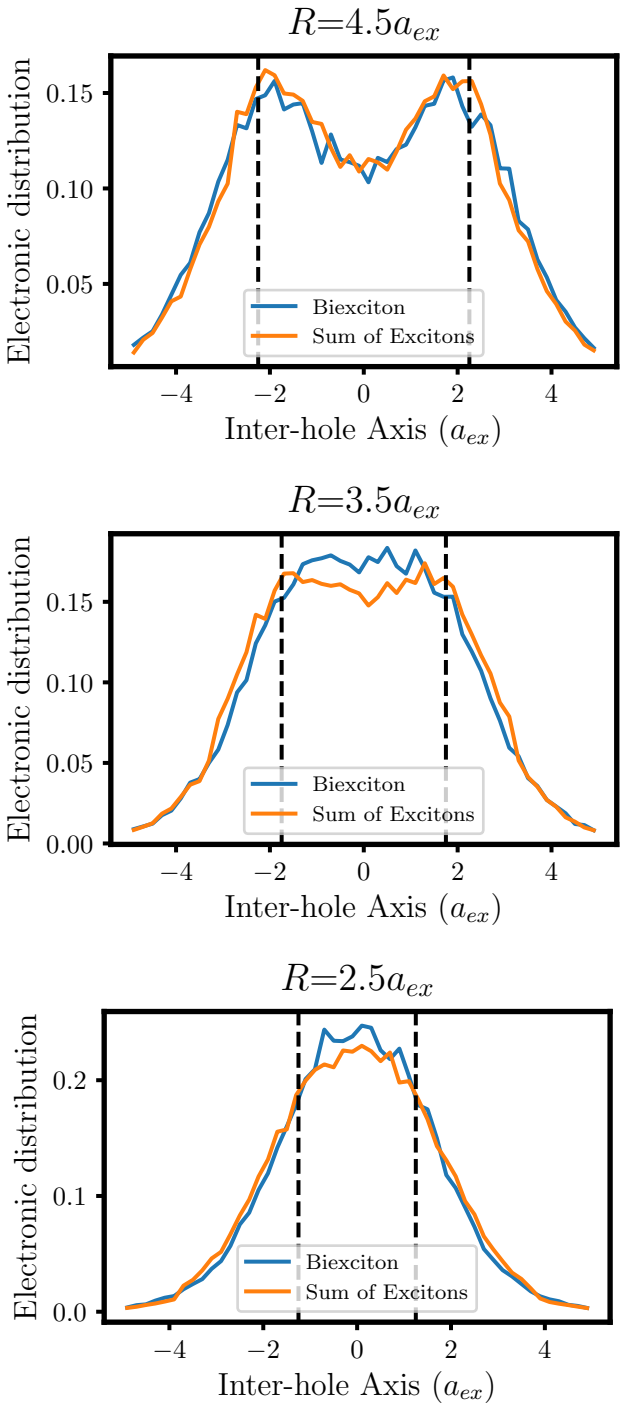

Figure 2.9: Comparing electronic densities of a biexciton with two excitons placed above the holes.

as the trial wavefunction and the variance σ^2 as the variational parameter. (For the remainder of this Chapter, σ will refer to a standard deviation of some Gaussian. Our solutions to the indirect exciton Hamiltonian hold for all electron-hole mass ratios since we use center-of-mass coordinates. In contrast, we will solve the biexciton and triexciton Hamiltonians within the infinitely heavy hole limit.)

The matrix elements for the kinetic and potential energy operator can be computed exactly in a Gaussian basis. Derivations are included in the appendix, and the results (in hartrees, $E_h = 2Ry_{ex}$) are

$$\int d\mathbf{r} g(r;\sigma^2)\Big(-\frac{1}{2m_{red}}\nabla^2\Big)g(r;\sigma^2) = \frac{1}{2m_{red}\sigma^2} \tag{2.18}$$

$$\int d\mathbf{r} g(r;\sigma^2)\Big(-\frac{1}{\kappa\sqrt{r^2+d^2}}\Big)g(r;\sigma^2) = -\sqrt{\frac{\pi}{\sigma^2}}\exp\big[\frac{d^2}{\sigma^2}\big]\mathrm{erfc}\big[\frac{d}{\sigma}\big] \tag{2.19}$$

The indirect exciton energy (in E_h) is thus

$$E(\sigma) = \frac{1}{2m_{red}\sigma^2} - \sqrt{\frac{\pi}{\sigma^2}}\exp\big[\frac{d^2}{\sigma^2}\big]\mathrm{erfc}\big[\frac{d}{\sigma}\big] \tag{2.20}$$

We differentiate this with respect to σ to find its optimal value. Figure 2.10 shows the resulting energy as a function of bilayer separation compared to the exact value given by Eq. (2.5). The ground state wavefunction at $d = 0$ is known to be an exponential, which explains why the Gaussian trial wavefunction gives a 25% relative error in this case.

The error in the energy decreases with increasing d, suggesting that the indirect exciton wavefunction becomes better described by a Gaussian. In truth, an indirect exciton resembles a harmonic oscillator at large bilayer separations. The multipole expansion of the Coulomb interaction is

$$-\frac{e^2}{\epsilon\sqrt{r^2+d^2}} = \frac{e^2}{\epsilon d}\big[-1+\frac{1}{2}\big(\frac{r}{d}\big)^2+\mathcal{O}\big(\frac{r}{d}\big)^4\big] \tag{2.21}$$

$$\approx -\tilde{E}+\frac{\tilde{E}}{2}\big(\frac{r}{d}\big)^2 \quad \frac{r}{d}\ll 1 \tag{2.22}$$

where $\tilde{E} = e^2/(\epsilon d)$ is the basic scale of the electrostatic attraction. The oscillator's characteristic frequency is thus

$$\omega = \sqrt{\frac{\tilde{E}}{d^2 m_{red}}} \tag{2.23}$$

$$= \sqrt{\frac{e^2}{\epsilon d^3 m_{red}}} \tag{2.24}$$

The ground state wavefunction of a harmonic oscillator is

$$\psi_{\text{oscillator}}(x) = \Big(\frac{m_{red}\omega}{\pi\hbar}\Big)^{1/4}\exp\Big[-\frac{m_{red}\omega x^2}{2\hbar}\Big] \tag{2.25}$$

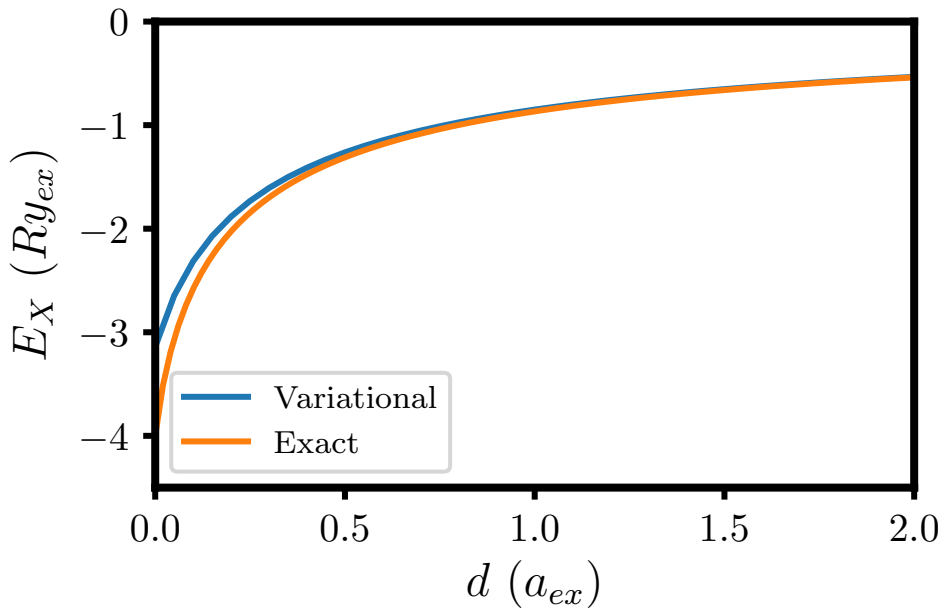

Figure 2.10: Ground state energy of an indirect exciton as a function of the bilayer separation. "Variational" refers to using a single Gaussian with the optimal variance. "DMC" refers to exact diffusion Monte Carlo results.

so its spatial extent (*i.e.*, its standard deviation) is

$$l = \sqrt{\frac{\hbar}{m_{red}\omega}} \tag{2.26}$$

Measured in exciton Bohr radii $a_{ex} = \hbar^2\epsilon/(m_{red}e^2)$, we get

$$\frac{l}{a_{ex}} = \left(\frac{d}{a_{ex}}\right)^{3/4} \tag{2.27}$$

We compare this expected value to the results of the variational approach in Figure 2.11. The electron and hole planes must be separated by hundreds of exciton Bohr radii before the exciton behaves like an oscillator.

To improve our variational wavefunction, we first naively added more Gaussians. In this case, we computed the exciton energy on a grid of σ^2 and chose the set which yielded the lowest energy. However, there is no straightforward way to obtain excited states which are typically used to incorporate electron-electron correlations. Therefore, we return to the single IX Hamiltonian, Eq. (2.15), and solve the time-independent Schrödinger equation

$$\left(-\frac{1}{2m_{red}}\nabla^2 - \frac{1}{\epsilon\sqrt{r^2+d^2}}\right)\phi(r,\theta) = E\phi(r,\theta) \tag{2.28}$$

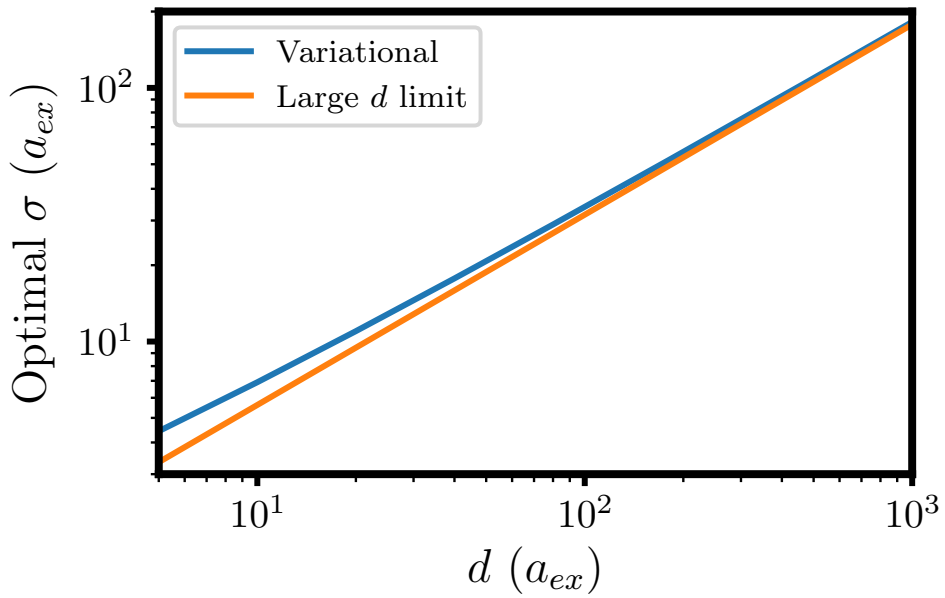

Figure 2.11: Comparing the optimal standard deviation of a single Gaussian modeling an indirect exciton to the large-d behavior of a harmonic oscillator.

We first separate variables and write

$$\phi(r,\theta) = R(r)\Theta(\theta) \tag{2.29}$$

The solution to the resultant angular equation is

$$\Theta(\theta) = \frac{1}{\sqrt{2\pi}}\exp[im\theta] \tag{2.30}$$

where m is the angular quantum number. Similar to atomic states in three dimensions, $m \leq n$, where n is the eigenvalue index for the radial component given by

$$-\frac{1}{2r}\frac{d}{dr}\left(r\frac{dR}{dr}\right) + \left(\frac{m^2}{2r^2} - \frac{1}{\sqrt{r^2+d^2}}\right)R(r) = E_{n,m}R(r) \tag{2.31}$$

We solved for the eigenvalues and eigenfunctions of Eq. (2.31) using a real-space grid and the Arnoldi method. Figure 2.12 compares the resulting ground state energy as a function of the bilayer separation to Eq. (2.5), a fit to the energy calculated using 4^{th}-order Runge-Kutta integration [59]. In Figure 2.13, we show the radial wavefunctions of the 1s state for various bilayer separations. These are normalized according to

$$1 = \int_0^\infty r|R(r)|^2 dr \tag{2.32}$$

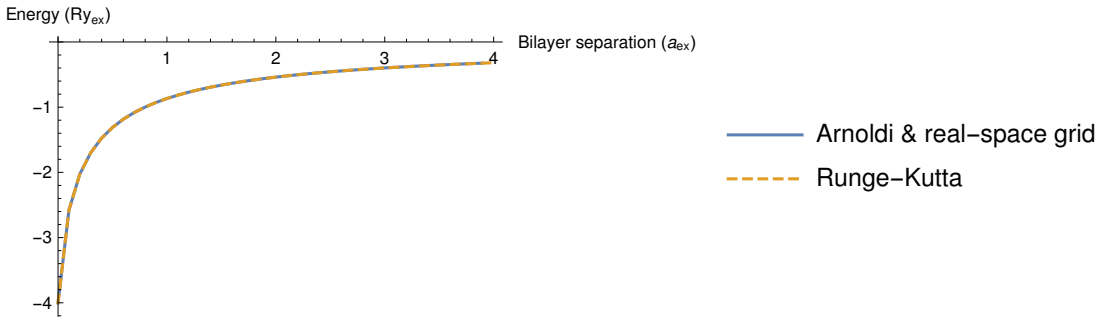

Figure 2.12: Ground state energy of an indirect exciton as a function of bilayer separation. "Arnoldi & real-space grid" refers to this work and "Runge-Kutta" comes from [59].

For $d > 0$, there is no longer a singularity in the Coulomb potential. Therefore, the cusp at $r = 0$ is smoothed as d increases. Additionally, the exciton becomes more delocalized as the bilayers separate as the electron experiences less of an attraction to the hole. Also shown in Figure 2.13 are radial wavefunctions for exemplary 2p and 3d states. Since these wavefunctions are zero at $r = 0$ and peaked away from the hole, they experience less of an effect with increasing d.

For the hydrogen atom in any number of dimensions, the Runge-Lenz vector is a conserved quantity, guaranteeing that the eigenvalues are independent of m. In the context of our bilayer model, this means $E_{n,m} \equiv E_n$ for $d = 0$. However, for $d > 0$, this symmetry is broken and the degeneracy with respect to m is lifted. Figure 2.14 shows how the indirect exciton spectrum changes with the bilayer separation. The spectrum compresses as d increases, and states with higher angular momentum are lower in energy.

To expedite the multi-exciton calculations, we rewrote the single exciton states as Gaussian contractions (*i.e.*, linear combinations of Gaussians) since they offer analytic matrix elements. However, as seen in Figure 2.13, states with $m > 0$ are not peaked at $r = 0$. Instead of fitting Gaussians to $R(r)$, we factor out r^{-m} and fit to

$$f(r) = r^{-m} R(r) \tag{2.33}$$

Similar to three-dimensional atomic states, these new functions $f(r)$ are peaked at $r = 0$, as shown in Figure 2.15. We subsequently minimize

$$\int_0^\infty r\left[f(r) - \sum_{i=1}^{N_g} c_i g(r, \sigma_i^2)\right]^2 dr \tag{2.34}$$

with respect to the Gaussians' variances σ_i^2 and their coefficients c_i. N_g is the number of Gaussians in our basis set. Figure 2.16 shows the relative error between the energy computed using these contracted states and the exact eigenvalues $E_{n,m}$. In order to describe

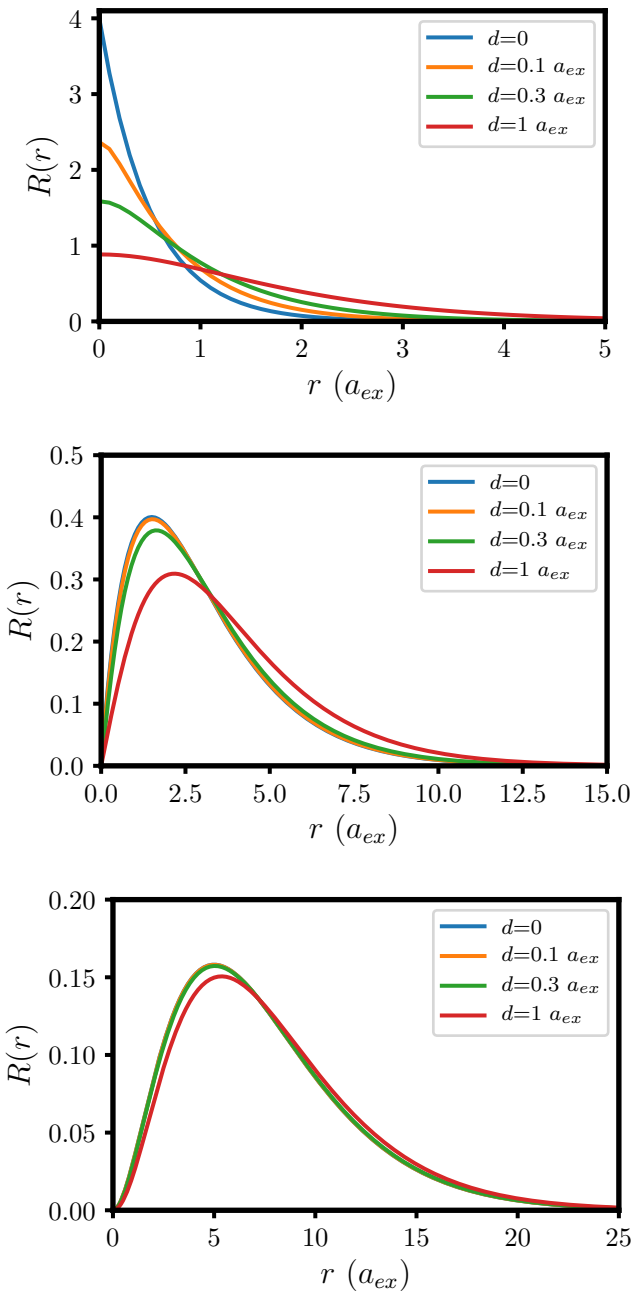

Figure 2.13: Radial wavefunctions, $R(r)$, for the 1s, 2p, and 3d states of an indirect exciton for various bilayer separations d.

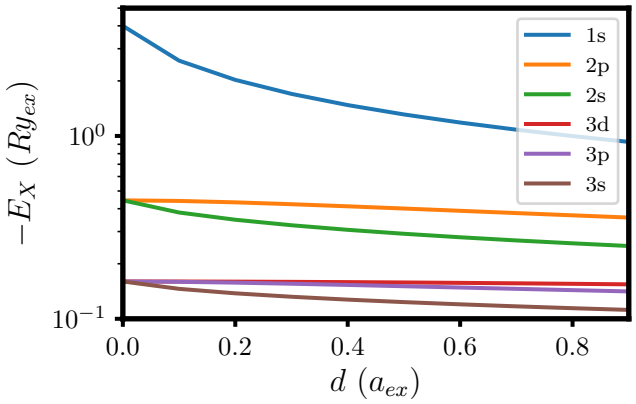

Figure 2.14: The first several eigenvalues as a function of bilayer separation. The degeneracy associated with the angular quantum number m is lifted for $d > 0$.

the attraction between excitons, we want this relative error to be at least less than the fraction of biexciton energy used in bonding:

$$\text{threshold} = \frac{V_{X-X}(R_{eq})}{E_{XX}(R_{eq})} \tag{2.35}$$

where R_{eq} is the equilibrium biexciton bond length. Using five Gaussians, the states up to 4s are under the $d = 0.9a_{ex}$ threshold for $0.5 \leq \frac{d}{a_{ex}} \leq 0.9$, and all of the states are under the $d = 0.4a_{ex}$ threshold.

2.4 Interactions between two indirect excitons using the full configuration interaction method

To test the validity of this orbital approach, we revisit the exciton-exciton interaction. Equipped with a basis for single excitons, we can use any method available in the quantum chemistry toolbox at the expense of working within the Born-Oppenheimer approximation (*i.e.*, taking the mass of the holes to infinity). This regime gives the strongest exciton-exciton attraction, and thus should provide the best conditions for exciton condensation.

Because the biexciton binding energy decreases with increasing bilayer separation, we seek an accurate method that captures as much electron-electron correlation as possible. We only consider a handful of electrons at a time, so we can afford the accurate but computationally expensive full configuration interaction (FCI) method. This approach includes all electron-electron correlation available within a given basis by diagonalizing the N-electron Hamiltonian in the basis of all possible N-electron states

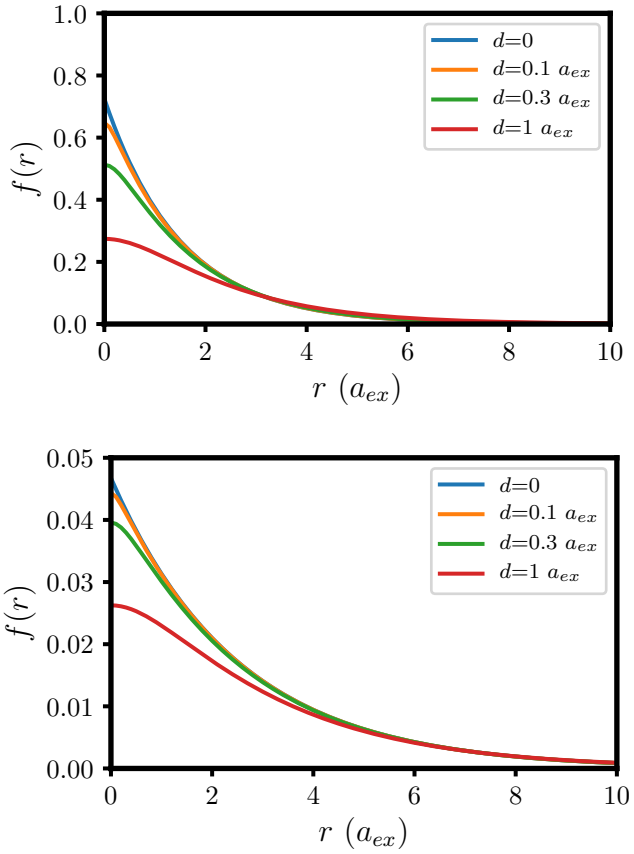

Figure 2.15: Plots of $f(r)$– radial wavefunctions multiplied by r^{-m}– for the 2p and 3d states of an indirect exciton for various bilayer separations d.

For $N = 2$, our Hamiltonian is Eq. (2.1) if we take $m_h \to \infty$. The matrix elements in terms of Gaussian states are derived in Section 2.6. The ground state spin configuration for the hydrogen molecule is a singlet, so we write the spin wavefunction for our biexciton as an antisymmetric singlet, as well. Consequently, our spatial wavefunction must be symmetric with respect to exchange of the electrons so that the overall wavefunction is antisymmetric. Our biexciton FCI wavefunction is

$$\Psi_{XX}(\mathbf{r}_1, \mathbf{r}_2) = \sum_{i,j=1}^{N_{orbitals}} c_{ij}\big(\phi_i(\mathbf{r}_1)\phi_j(\mathbf{r}_2) + \phi_j(\mathbf{r}_1)\phi_i(\mathbf{r}_2)\big) \tag{2.36}$$

ϕ_i is a Gaussian contraction of the single exciton orbital i (*e.g.*, 1s, 2p, *etc.*) located in the electrons' plane directly above one of the holes. This is a generalization of the generalized valence bond (GVB) wavefunction [65]. The Heitler-London wavefunction studied by both Okumura and Zimmerman [55,58] is a specific case of the GVB wavefunction.

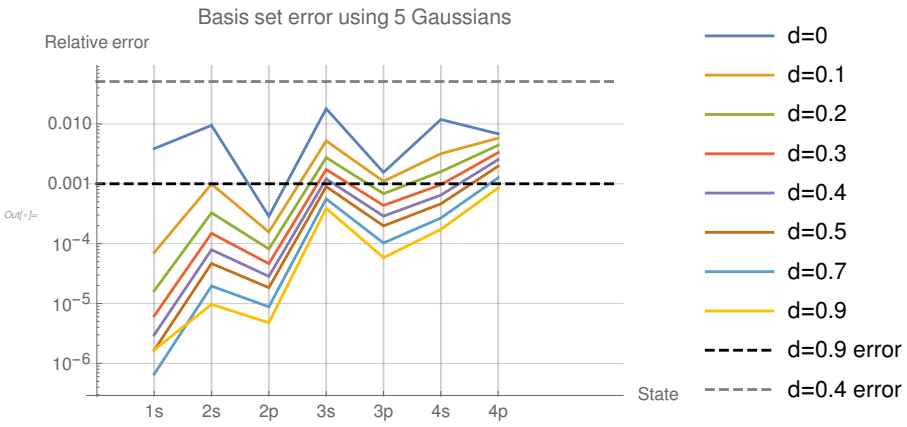

Figure 2.16: The relative error of our 5-Gaussian basis set for the first several states and several bilayer separations d. The dashed lines are the thresholds given in Eq. (2.35).

Figure 2.17 shows interaction potentials for $d = 0$. As we increase our basis set from {1s} to {1s,2s,2p}, we converge towards the exact diffusion Monte Carlo result. However, we observe slow convergence. While our single IX basis is complete, we can only afford a handful of states at a time. Therefore, we optimized our basis sets. Inspired by Dunning's "correlation-consistent" basis sets [66], we scaled the size of our orbitals to account for electron-electron repulsion. Specifically, we minimized the biexciton energy at the equilibrium geometry by dividing the standard deviations of the Gaussians by ξ:

$$g_{\text{scaled}}(r; \sigma^2, \xi) = g(r; (\sigma/\xi)^2) \tag{2.37}$$

The optimal scaling factor depends on the separation between the holes, but we fixed ξ for all configurations for simplicity as we are mainly interested in describing the attractive force between excitons. This leads to an artificial repulsion at large exciton-exciton separations, as shown in Figure 2.17.

For $d = 0$, the 1s states were scaled by $\xi_{1s} = 1.3$, leading to a substantial increase in the interaction potential as shown in Figure 2.17. Similar to the three-dimensional hydrogen molecule, shrunken 1s orbitals reduce the electron-electron repulsion. For $0.1 \leq \frac{d}{a_{ex}} \leq 0.3$, the optimal ξ_{1s} decreased to 1.2 and 1.1, and $\xi_{1s} = 1$ for $d > 0.4a_{ex}$. As d increases, the single-particle states delocalize (see Figure 2.13) and the growing dipole moments of the IXs increases their equilibrium separation. These two factors cause the natural, unscaled 1s orbitals to afford the largest electron-hole attraction and minimal electron-electron repulsion.

For $d \leq 0.5a_{ex}$, we observe exciton-exciton attraction using only scaled 1s orbitals, whereas more states are required for larger bilayer separations. Coincidentally, the energy difference between the 1s and 2p states falls below $1Ry_{ex}$ for $d > 0.5a_{ex}$. Thus, for these larger bilayer separations, electron-electron correlations "push" the electrons to higher-energy orbitals in order to form an indirect biexciton. Figure 2.18 shows the interaction potential for

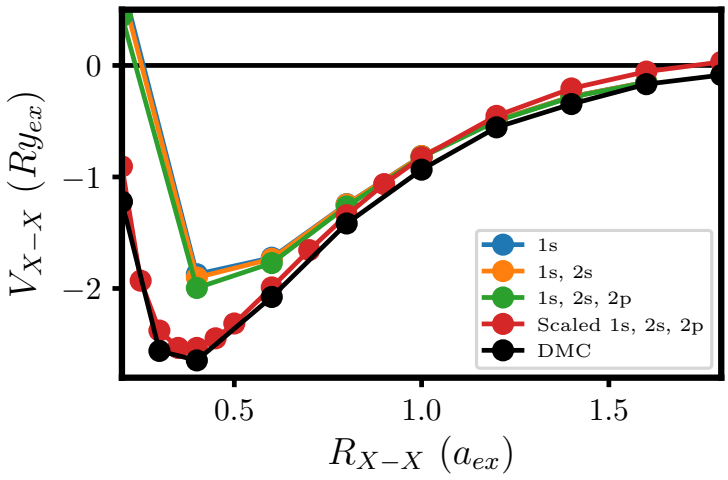

Figure 2.17: Exciton-exciton interaction potential for $d = 0$ and $\sigma = 0$ calculated using our FCI approach. Also shown is the exact DMC result.

$d = 0.6a_{ex}$. The 2p states needed to be optimized in order to observe the exciton-exciton attraction. While we only capture half of the well depth by optimizing the 1s, 2s, and 2p orbitals, our biexciton energy E_{XX} has a relative error of 1%. A table containing the optimal scaling factors is included in Section 2.7.

Figure 2.19 compares exciton-exciton interaction potentials for d=0, 0.1, and $0.5a_{ex}$. As expected from diffusion Monte Carlo results, the equilibrium hole-hole separation increases and the exciton-exciton attraction decreases as d grows. (Recall that the $d = 0$ potential does not go to zero at large R_{X-X} because we fix ξ. In reality, the orbitals relax (*i.e.*, $\xi \to 1$) as the excitons are separated.)

Using optimized 1s, 2s, 2p, and 3d orbitals is insufficient to capture the exciton-exciton attraction for $0.7 \leq \frac{d}{a_{ex}} < 1$. While the biexciton energy would continue to decrease as we include more orbitals, it is unknown how many states would be needed to observe an attraction. Furthermore, the experiments of Bar-Joseph [42,43] study coupled quantum wells with a center-to-center distance of $1.5a_{ex}$ and an electron-hole mass ratio of $\sigma = 0.1$. As shown in Figure 2.6, biexcitons are only stable up to d=1 a_{ex} for $\sigma = 0$. So, classical condensation of IXs– if possible– would occur between repulsive entities, for which there is little evidence. Instead of converging our biexciton calculations for large d, we next turn to triexciton calculations. Our goal will be to assess, for any d, whether the three-body potential can be approximately described by pair potentials and whether multiple indirect excitons will be energetically stable.

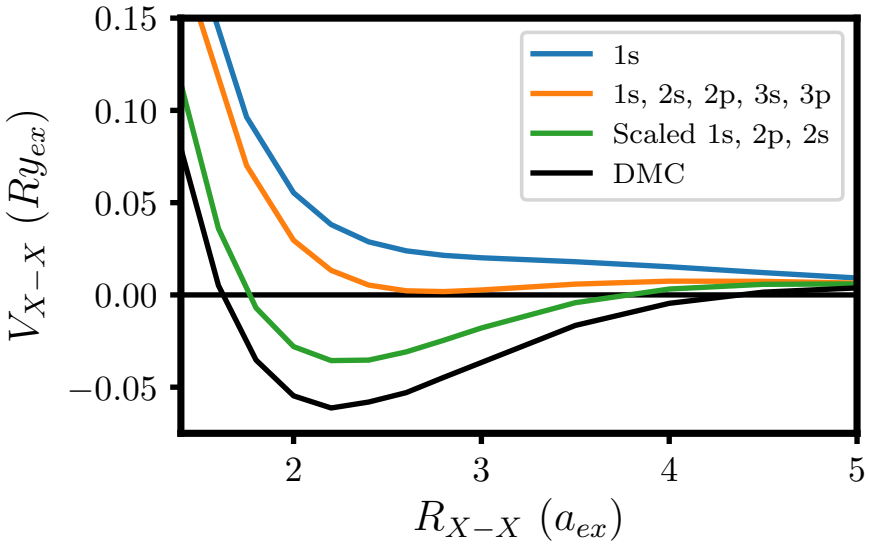

Figure 2.18: Exciton-exciton interaction potential for $d = 0.6a_{ex}$ and $\sigma = 0$ calculated using our FCI approach.

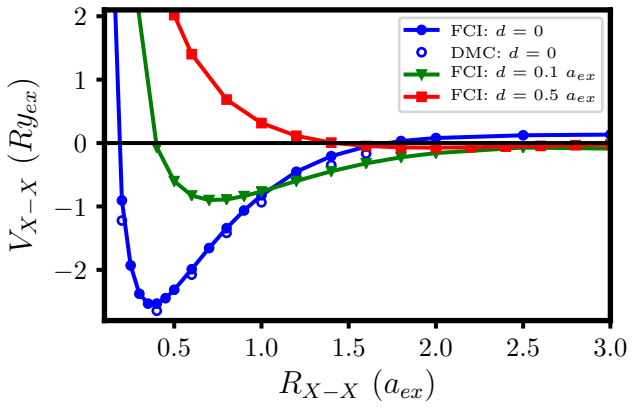

Figure 2.19: Various exciton-exciton interaction potentials.

2.5 Interactions among three indirect excitons using the full configuration interaction method

Extending our approach from Section 2.4, we now consider three indirect excitons in the heavy-hole limit. The Hamiltonian is

$$H = -\frac{1}{2m_e}\left(\nabla_1^2+\nabla_2^2+\nabla_3^2\right)+\frac{1}{2}\sum_{i=1,2,3}\sum_{j\neq i}\frac{1}{\epsilon|\mathbf{r}_i-\mathbf{r}_j|}+\frac{1}{2}\sum_{\alpha=a,b,c}\sum_{\beta\neq\alpha}\frac{1}{\epsilon|\mathbf{r}_\alpha-\mathbf{r}_\beta|} - \sum_{i=1,2,3}\sum_{\alpha=a,b,c}\frac{1}{\epsilon\sqrt{|\mathbf{r}_i-\mathbf{r}_\alpha|^2+d^2}} \tag{2.38}$$

Writing the triexciton wavefunction is not as straightforward as the biexciton case. To enforce the antisymmetry of the electrons, we start from a Slater determinant:

$$\Psi_{XXX}(\mathbf{r}_1,\mathbf{r}_2,\mathbf{r}_3,\omega_1,\omega_2,\omega_3)=\begin{vmatrix}\phi_a(\mathbf{r}_1)\alpha(\omega_1) & \phi_b(\mathbf{r}_1)\beta(\omega_1) & \phi_c(\mathbf{r}_1)\alpha(\omega_1)\\ \phi_a(\mathbf{r}_2)\alpha(\omega_2) & \phi_b(\mathbf{r}_2)\beta(\omega_2) & \phi_c(\mathbf{r}_2)\alpha(\omega_2)\\ \phi_a(\mathbf{r}_3)\alpha(\omega_3) & \phi_b(\mathbf{r}_3)\beta(\omega_3) & \phi_c(\mathbf{r}_3)\alpha(\omega_3)\end{vmatrix} \tag{2.39}$$

ϕ_a is a single-particle spatial orbital, α and β are spin functions, and ω_i is the spin variable for electron i. This wavefunction is not an eigenstate of the total spin operator

$$\hat{S}^2 = \hat{S}_-\hat{S}_+ + \hat{S}_z + \hat{S}_z^2 \tag{2.40}$$

$$= \hat{P}_{\alpha\beta} + \frac{1}{4}\left(2N + (N_\alpha - N_\beta)^2\right) \tag{2.41}$$

where $\hat{S}_\pm = \sum_{i=1}^N \hat{s}_\pm$ are ladder operators, $\hat{P}_{\alpha\beta} = \sum_{i\neq j}^N\sum_{j=1}^N \hat{s}_-(i)\hat{s}_+(j)$ permutes the spin orbitals, N is the total number of electrons, and N_α (N_β) is the number of spin up (down) particles [67]. Operating Eq. (2.41) on Eq. (2.39) yields

$$\begin{aligned}\hat{S}^2\Psi_{XXX} = &\begin{vmatrix}\phi_a(\mathbf{r}_1)\alpha(\omega_1) & \phi_b(\mathbf{r}_1)\alpha(\omega_1) & \phi_c(\mathbf{r}_1)\beta(\omega_1)\\ \phi_a(\mathbf{r}_2)\alpha(\omega_2) & \phi_b(\mathbf{r}_2)\alpha(\omega_2) & \phi_c(\mathbf{r}_2)\beta(\omega_2)\\ \phi_a(\mathbf{r}_3)\alpha(\omega_3) & \phi_b(\mathbf{r}_3)\alpha(\omega_3) & \phi_c(\mathbf{r}_3)\beta(\omega_3)\end{vmatrix}\\ &+\frac{7}{4}\begin{vmatrix}\phi_a(\mathbf{r}_1)\alpha(\omega_1) & \phi_b(\mathbf{r}_1)\beta(\omega_1) & \phi_c(\mathbf{r}_1)\alpha(\omega_1)\\ \phi_a(\mathbf{r}_2)\alpha(\omega_2) & \phi_b(\mathbf{r}_2)\beta(\omega_2) & \phi_c(\mathbf{r}_2)\alpha(\omega_2)\\ \phi_a(\mathbf{r}_3)\alpha(\omega_3) & \phi_b(\mathbf{r}_3)\beta(\omega_3) & \phi_c(\mathbf{r}_3)\alpha(\omega_3)\end{vmatrix}\\ &+\begin{vmatrix}\phi_a(\mathbf{r}_1)\beta(\omega_1) & \phi_b(\mathbf{r}_1)\alpha(\omega_1) & \phi_c(\mathbf{r}_1)\alpha(\omega_1)\\ \phi_a(\mathbf{r}_2)\beta(\omega_2) & \phi_b(\mathbf{r}_2)\alpha(\omega_2) & \phi_c(\mathbf{r}_2)\alpha(\omega_2)\\ \phi_a(\mathbf{r}_3)\beta(\omega_3) & \phi_b(\mathbf{r}_3)\alpha(\omega_3) & \phi_c(\mathbf{r}_3)\alpha(\omega_3)\end{vmatrix}\end{aligned} \tag{2.42}$$

which is clearly not equal to Eq. (2.39).

To obtain an eigenstate of $\hat{S}^2$, we can project Eq. (2.39) onto the desired spin state. This requires us to know the transformation between the uncoupled and coupled bases. While this

generally involves Clebsch-Gordon coefficients, our system of three electrons is easy enough to solve directly. Without loss of generality, we pair the spins of electrons 1 and 2 into a singlet and couple the spin of the third electron which we choose to be up. In the uncoupled basis, we have

$$|\text{doublet}\rangle = \Big(\frac{|\uparrow\downarrow\rangle_{1,2} - |\downarrow\uparrow\rangle_{1,2}}{\sqrt{2}}\Big)\,|\uparrow\rangle_3 = \frac{|\uparrow\downarrow\uparrow\rangle_{1,2,3} - |\downarrow\uparrow\uparrow\rangle_{1,2,3}}{\sqrt{2}} \tag{2.43}$$

Since singlet states have zero spin, we know that in the coupled basis,

$$|\text{doublet}\rangle = |\frac{1}{2};+\frac{1}{2}\rangle \tag{2.44}$$

Finally, we project Eq. (2.39) onto Eq. (2.43) to obtain

$$\begin{aligned}
&|\frac{1}{2};+\frac{1}{2}\rangle \Big(\frac{\langle\uparrow\downarrow\uparrow| - \langle\downarrow\uparrow\uparrow|}{\sqrt{2}}\Big) \begin{vmatrix} \phi_a(\mathbf{r}_1)\,|\uparrow\rangle & \phi_b(\mathbf{r}_1)\,|\downarrow\rangle & \phi_c(\mathbf{r}_1)\,|\uparrow\rangle \\ \phi_a(\mathbf{r}_2)\,|\uparrow\rangle & \phi_b(\mathbf{r}_2)\,|\downarrow\rangle & \phi_c(\mathbf{r}_2)\,|\uparrow\rangle \\ \phi_a(\mathbf{r}_3)\,|\uparrow\rangle & \phi_b(\mathbf{r}_3)\,|\downarrow\rangle & \phi_c(\mathbf{r}_3)\,|\uparrow\rangle \end{vmatrix} \\
&= \Big(\phi_a(\mathbf{r}_1)\phi_b(\mathbf{r}_2)\phi_c(\mathbf{r}_3) - \phi_c(\mathbf{r}_1)\phi_b(\mathbf{r}_2)\phi_a(\mathbf{r}_3) \\
&- \phi_b(\mathbf{r}_1)\phi_c(\mathbf{r}_2)\phi_a(\mathbf{r}_3) + \phi_b(\mathbf{r}_1)\phi_a(\mathbf{r}_2)\phi_c(\mathbf{r}_3)\Big)\frac{1}{\sqrt{2}}\,|\frac{1}{2};+\frac{1}{2}\rangle
\end{aligned} \tag{2.45}$$

Summing over all possible orbitals, the full configuration interaction wavefunction reads

$$\begin{aligned}
\Psi_{XXX}(\mathbf{r}_1,\mathbf{r}_2,\mathbf{r}_3) = \sum_{i,j}^{N_{orbitals}} \sum_{k\neq i}^{N_{orbitals}} &\Big(\phi_i(\mathbf{r}_1)\phi_j(\mathbf{r}_2)\phi_k(\mathbf{r}_3) + \phi_j(\mathbf{r}_1)\phi_i(\mathbf{r}_2)\phi_k(\mathbf{r}_3) \\
&- \phi_k(\mathbf{r}_1)\phi_j(\mathbf{r}_2)\phi_i(\mathbf{r}_3) - \phi_j(\mathbf{r}_1)\phi_k(\mathbf{r}_2)\phi_i(\mathbf{r}_3)\Big)
\end{aligned} \tag{2.46}$$

After surveying the potential energy surface, we determined that the collinear configuration yields the lowest energy for all bilayer separations. Furthermore, the lowest energy is always attained when two indirect excitons are separated by the equilibrium biexciton "bond length," similar to the van der Waals complex of H_3. Figure 2.20 shows exciton-biexciton interaction potentials for various bilayer separations. As in the case for the two-body potentials, the equilibrium separation increases and the binding energy decreases with increasing d. However, unlike the pair potentials, these well depths are 1000 times smaller. Furthermore, an indirect triexciton complex is only energetically stable for $d \leq 0.1a_{ex}$. Finding no evidence supporting the condensation of multiple IXs, we conclude that the condensed phase observed in [42,43,45] is not a classical liquid of excitons.

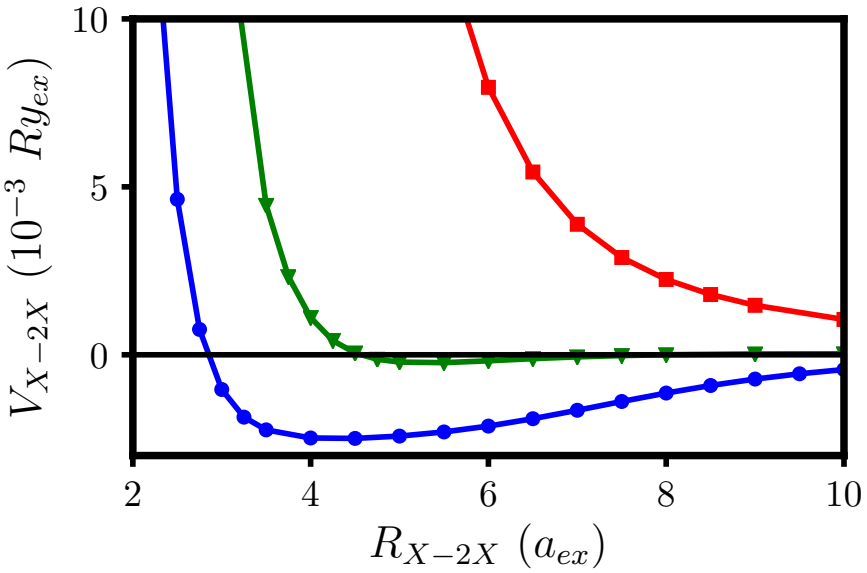

Figure 2.20: Exciton-biexciton interaction potentials for various bilayer separations computed using our FCI approach. The three excitons are collinear, and the distance between the two closest excitons is the equilibrium biexciton bond length. R_{X-2X} is the distance between the center of mass of the biexciton and the third exciton.

2.6 Appendix: matrix elements for full configuration interaction calculations

2.6.1 s orbitals

2.6.1.1 Overlap matrix elements

It is well-known that the product of two Gaussians is a third Gaussian [65]. Defining

$$g(\vec{r}-\vec{r}_A) = \exp\left[-\alpha|\vec{r}-\vec{r}_A|^2\right] \tag{2.47}$$

we have

$$g(\vec{r}-\vec{r}_A)g(\vec{r}-\vec{r}_B) = Kg(\vec{r}-\vec{r}_P) \tag{2.48}$$

where

$$K = \exp\left[-\frac{\alpha\beta}{(\alpha+\beta)}|\vec{r}_A-\vec{r}_B|^2\right] \tag{2.49}$$

$$\vec{r}_P = \frac{\alpha\vec{r}_A+\beta\vec{r}_B}{\alpha+\beta} \tag{2.50}$$

and the new exponent is

$$p = \alpha + \beta \tag{2.51}$$

Starting from

$$\frac{1}{\pi\sigma_i\sigma_j}\int \exp\big[-\frac{|\vec{r}_e-\vec{r}_A|^2}{2\sigma_i^2}\big]\exp\big[-\frac{|\vec{r}_e-\vec{r}_B|^2}{2\sigma_j^2}\big]d\vec{r}_e \tag{2.52}$$

we combine the two Gaussians into a single Gaussian.

$$(2.52) = \frac{\exp\Big[-\frac{|\vec{r}_A-\vec{r}_B|^2}{2\sigma_i^2+2\sigma_j^2}\Big]}{\pi\sigma_i\sigma_j}\int \exp\Big[-\big(\frac{1}{2\sigma_i^2}+\frac{1}{2\sigma_j^2}\big)|\vec{r}_e-\frac{\vec{r}_A/(2\sigma_i^2)+\vec{r}_B/(2\sigma_j^2)}{\frac{1}{2\sigma_i^2}+\frac{1}{2\sigma_j^2}}|^2\Big]d\vec{r}_e \tag{2.53}$$

Centering this new Gaussian,

$$(2.52) = \frac{\exp\Big[-\frac{|\vec{r}_A-\vec{r}_B|^2}{2\sigma_i^2+2\sigma_j^2}\Big]}{\pi\sigma_i\sigma_j}\int \exp\Big[-\big(\frac{1}{2\sigma_i^2}+\frac{1}{2\sigma_j^2}\big)r_e^2\Big]d\vec{r}_e \tag{2.54}$$

The angular integral yields 2π, and the radial integral is evaluated using

$$\int_0^\infty x\exp[-\alpha x^2]dx = \frac{1}{2\alpha} \tag{2.55}$$

The result is

$$(2.52) = \frac{2\exp\Big[-\frac{|\vec{r}_A-\vec{r}_B|^2}{2\sigma_i^2+2\sigma_j^2}\Big]}{\sigma_i\sigma_j\big(\frac{1}{\sigma_i^2}+\frac{1}{\sigma_j^2}\big)} \tag{2.56}$$

For four Gaussians, we start from

$$\begin{aligned}\frac{1}{\pi^2\sigma_i\sigma_j\sigma_k\sigma_l}\int\int \exp\big[-\frac{|\vec{r}_{e1}-\vec{r}_A|^2}{2\sigma_i^2}\big]\exp\big[-\frac{|\vec{r}_{e2}-\vec{r}_C|^2}{2\sigma_k^2}\big]\\ \times\exp\big[-\frac{|\vec{r}_{e1}-\vec{r}_B|^2}{2\sigma_j^2}\big]\exp\big[-\frac{|\vec{r}_{e2}-\vec{r}_B|^2}{2\sigma_l^2}\big]d\vec{r}_{e1}d\vec{r}_{e2}\end{aligned} \tag{2.57}$$

we combine the two pairs of Gaussians and center them to get

$$\begin{aligned}(2.57) =&\frac{\exp\Big[-\frac{|\vec{r}_A-\vec{r}_C|^2}{2\sigma_i^2+2\sigma_k^2}-\frac{|\vec{r}_B-\vec{r}_D|^2}{2\sigma_j^2+2\sigma_l^2}\Big]}{\pi^2\sigma_i\sigma_j\sigma_k\sigma_l}\\ &\times\int\int\exp\Big[-\big(\frac{1}{2\sigma_i^2}+\frac{1}{2\sigma_k^2}\big)r_{e1}^2-\big(\frac{1}{2\sigma_j^2}+\frac{1}{2\sigma_l^2}\big)r_{e2}^2\Big]d\vec{r}_{e1}d\vec{r}_{e2}\end{aligned} \tag{2.58}$$

The result is

$$(2.57) = \frac{4\exp\Big[-\frac{|\vec{r}_A-\vec{r}_C|^2}{2\sigma_i^2+2\sigma_k^2}-\frac{|\vec{r}_B-\vec{r}_D|^2}{2\sigma_j^2+2\sigma_l^2}\Big]}{\sigma_i\sigma_j\sigma_k\sigma_l\big(\frac{1}{\sigma_i^2}+\frac{1}{\sigma_k^2}\big)\big(\frac{1}{\sigma_j^2}+\frac{1}{\sigma_l^2}\big)} \tag{2.59}$$

2.6.1.2 Kinetic energy matrix element

Starting from

$$-\frac{1}{2m\pi\sigma_i\sigma_k}\int \exp\big[-\frac{|\vec{r}_e-\vec{r}_A|^2}{2\sigma_i^2}\big]\nabla_e^2\exp\big[-\frac{|\vec{r}_e-\vec{r}_B|^2}{2\sigma_k^2}\big]d\vec{r}_e \tag{2.60}$$

we center the Gaussian on the right to get

$$(2.60)=-\frac{1}{2m\pi\sigma_i\sigma_k}\int \exp\big[-\frac{|\vec{r}_e+\vec{r}_B-\vec{r}_A|^2}{2\sigma_i^2}\big]\nabla_e^2\exp\big[-\frac{r_e^2}{2\sigma_k^2}\big]d\vec{r}_e \tag{2.61}$$

Evaluating the polar Laplacian,

$$(2.60)=-\frac{1}{2m\pi\sigma_i\sigma_k}\int \exp\big[-\frac{|\vec{r}_e+\vec{r}_B-\vec{r}_A|^2}{2\sigma_i^2}\big]\Big[\frac{r_e^2}{\sigma_k^4}\exp\big[-\frac{r_e^2}{2\sigma_k^2}\big]-\frac{2}{\sigma_k^2}\exp\big[-\frac{r_e^2}{2\sigma_k^2}\big]\Big]d\vec{r}_e \tag{2.62}$$

Letting $\vec{r}_C=\vec{r}_B-\vec{r}_A$, we distribute the Gaussian and combine the pairs to get

$$\begin{aligned}(2.60)=&-\frac{\exp\Big[-\frac{r_C^2}{2\sigma_i^2+2\sigma_k^2}\Big]}{2m\pi\sigma_i\sigma_k}\Big\{\frac{1}{\sigma_k^4}\int r_e^2\exp\Big[-\big(\frac{\sigma_i^2+\sigma_k^2}{2\sigma_i^2\sigma_k^2}\big)|\vec{r}_e+\frac{\sigma_k^2\vec{r}_C}{\sigma_i^2+\sigma_k^2}|^2\Big]d\vec{r}_e\\&-\frac{2}{\sigma_k^2}\int r_e^2\exp\Big[-\big(\frac{\sigma_i^2+\sigma_k^2}{2\sigma_i^2\sigma_k^2}\big)|\vec{r}_e+\frac{\sigma_k^2\vec{r}_C}{\sigma_i^2+\sigma_k^2}|^2\Big]d\vec{r}_e\Big\}\end{aligned} \tag{2.63}$$

We again center the Gaussians to get

$$\begin{aligned}(2.60)=&-\frac{\exp\Big[-\frac{r_C^2}{2\sigma_i^2+2\sigma_k^2}\Big]}{2m\pi\sigma_i\sigma_k}\Big\{\frac{1}{\sigma_k^4}\int |\vec{r}_e-\frac{\sigma_k^2\vec{r}_C}{\sigma_i^2+\sigma_k^2}|^2\exp\Big[-\big(\frac{\sigma_i^2+\sigma_k^2}{2\sigma_i^2\sigma_k^2}\big)r_e^2\Big]d\vec{r}_e\\&-\frac{2}{\sigma_k^2}\int r_e^2\exp\Big[-\big(\frac{\sigma_i^2+\sigma_k^2}{2\sigma_i^2\sigma_k^2}\big)r_e^2\Big]d\vec{r}_e\Big\}\end{aligned} \tag{2.64}$$

We evaluate the second integral and expand the norm in the first term.

$$\begin{aligned}(2.60)=&-\frac{\exp\Big[-\frac{r_C^2}{2\sigma_i^2+2\sigma_k^2}\Big]}{2m\pi\sigma_i\sigma_k}\Big\{\frac{1}{\sigma_k^4}\int\big(r_e^2-2\frac{\sigma_k^2}{\sigma_i^2+\sigma_k^2}r_e r_C\cos\theta+\frac{\sigma_k^4}{(\sigma_i^2+\sigma_k^2)^2}r_C^2\big)\\&\times\exp\Big[-\big(\frac{\sigma_i^2+\sigma_k^2}{2\sigma_i^2\sigma_k^2}\big)r_e^2\Big]d\vec{r}_e-\frac{4\pi}{\sigma_k^2}\frac{\sigma_i^2\sigma_k^2}{(\sigma_i^2+\sigma_k^2)}\Big\}\end{aligned} \tag{2.65}$$

where θ is the angle between $\vec{r}_e$ and $\vec{r}_C$. The second integrand is the only term with angular dependence, and luckily that angular integral yields 0. After completing the other integrals, we get

$$(2.60)=-\frac{\exp\Big[-\frac{r_C^2}{2\sigma_i^2+2\sigma_k^2}\Big]}{2m\pi\sigma_i\sigma_k}\Big\{\frac{1}{\sigma_k^4}\big(\frac{4\pi\sigma_i^4\sigma_k^4}{(\sigma_i^2+\sigma_k^2)^2}+\frac{2\pi\sigma_i^2\sigma_k^6 r_C^2}{(\sigma_i^2+\sigma_k^2)^3}\big)-\frac{4\pi\sigma_i^2\sigma_k^2}{\sigma_k^2(\sigma_i^2+\sigma_k^2)}\Big\} \tag{2.66}$$

$$=-\frac{\exp\Big[-\frac{r_C^2}{2\sigma_i^2+2\sigma_k^2}\Big]\sigma_i^2}{m\sigma_i\sigma_k(\sigma_i^2+\sigma_k^2)}\Big\{\frac{2\sigma_i^2}{\sigma_i^2+\sigma_k^2}+\frac{\sigma_k^2 r_C^2}{(\sigma_i^2+\sigma_k^2)^2}-2\Big\} \tag{2.67}$$

2.6.1.3 Electron-hole matrix element

We start from

$$-\frac{1}{\pi\sigma_i\sigma_j}\int \exp\big[-\frac{|\vec{r}_e-\vec{r}_A|^2}{2\sigma_i^2}\big]\frac{1}{\sqrt{|\vec{r}_e-\vec{r}_B|^2+d^2}}\exp\big[-\frac{|\vec{r}_e-\vec{r}_C|^2}{2\sigma_j^2}\big]d\vec{r}_e \tag{2.68}$$

Combining the 2 Gaussians, we get

$$(2.68)=-\frac{\exp\big[-\frac{|\vec{r}_A-\vec{r}_C|^2}{2\sigma_i^2+2\sigma_j^2}\big]}{\pi\sigma_i\sigma_j}\int \exp\Big[-\frac{\sigma_i^2+\sigma_j^2}{2\sigma_i^2\sigma_j^2}|\vec{r}_e-\frac{\sigma_j^2\vec{r}_A+\sigma_i^2\vec{r}_C}{\sigma_i^2+\sigma_j^2}|^2\Big]\frac{1}{\sqrt{|\vec{r}_e-\vec{r}_B|^2+d^2}}d\vec{r}_e \tag{2.69}$$

Taking $\vec{r}_e-\vec{r}_B\to\vec{r}_e$,

$$(2.68)=-\frac{\exp\big[-\frac{|\vec{r}_A-\vec{r}_C|^2}{2\sigma_i^2+2\sigma_j^2}\big]}{\pi\sigma_i\sigma_j}\int \exp\Big[-\frac{\sigma_i^2+\sigma_j^2}{2\sigma_i^2\sigma_j^2}|\vec{r}_e+\vec{r}_B-\frac{\sigma_j^2\vec{r}_A+\sigma_i^2\vec{r}_C}{\sigma_i^2+\sigma_j^2}|^2\Big]\frac{1}{\sqrt{r_e^2+d^2}}d\vec{r}_e \tag{2.70}$$

We rewrite the Coulomb potential in terms of its inverse Fourier transform:

$$\frac{1}{\sqrt{r^2+d^2}}=\frac{1}{2\pi}\int d^2\vec{k}\frac{\exp[-kd]}{k}\exp[-i\vec{k}\cdot\vec{r}] \tag{2.71}$$

Thus,

$$\begin{aligned}(2.68)=-\frac{\exp\big[-\frac{|\vec{r}_A-\vec{r}_C|^2}{2\sigma_i^2+2\sigma_j^2}\big]}{2\pi^2\sigma_i\sigma_j}\int d^2\vec{k}\frac{\exp[-kd]}{k}\int d^2\vec{r}_e\exp[-i\vec{k}\cdot\vec{r}_e]\\ \times\exp\Big[-\frac{\sigma_i^2+\sigma_j^2}{2\sigma_i^2\sigma_j^2}|\vec{r}_e+\vec{r}_B-\frac{\sigma_j^2\vec{r}_A+\sigma_i^2\vec{r}_C}{\sigma_i^2+\sigma_j^2}|^2\Big]\end{aligned} \tag{2.72}$$

After transforming $\vec{r}_e+\vec{r}_B-\frac{\sigma_j^2\vec{r}_A+\sigma_i^2\vec{r}_C}{\sigma_i^2+\sigma_j^2}\to\vec{r}_e$, we evaluate the $\vec{r}_e$ integral by taking the Fourier transform of the Gaussian.

$$\begin{aligned}(2.68)&=-\frac{\exp\big[-\frac{|\vec{r}_A-\vec{r}_C|^2}{2\sigma_i^2+2\sigma_j^2}\big]}{2\pi^2\sigma_i\sigma_j}\int d^2\vec{k}\frac{\exp[-kd]}{k}\exp[-i\vec{k}\cdot\big\{\frac{\sigma_j^2\vec{r}_A+\sigma_i^2\vec{r}_C}{\sigma_i^2+\sigma_j^2}-\vec{r}_B\big\}]\\ &\times\frac{2\pi\sigma_i^2\sigma_j^2}{\sigma_i^2+\sigma_j^2}\exp\Big[-\frac{\sigma_i^2\sigma_j^2}{2(\sigma_i^2+\sigma_j^2)}k^2\Big]\end{aligned} \tag{2.73}$$

$$\begin{aligned}&=-\frac{\exp\big[-\frac{|\vec{r}_A-\vec{r}_C|^2}{2\sigma_i^2+2\sigma_j^2}\big]}{\pi\sigma_i\sigma_j}\frac{\sigma_i^2\sigma_j^2}{\sigma_i^2+\sigma_j^2}\int d^2\vec{k}\frac{\exp[-kd]}{k}\exp\Big[-\frac{\sigma_i^2\sigma_j^2}{2(\sigma_i^2+\sigma_j^2)}k^2\Big]\\ &\times\exp[-ik\Big|\frac{\sigma_j^2\vec{r}_A+\sigma_i^2\vec{r}_C}{\sigma_i^2+\sigma_j^2}-\vec{r}_B\Big|\cos\theta]\end{aligned} \tag{2.74}$$

Using the definition of the Bessel function of order 0 (which includes a factor of 2π), we get

$$(2.68) = -\frac{2\sigma_i\sigma_j \exp\big[-\frac{|\vec{r}_A-\vec{r}_C|^2}{2\sigma_i^2+2\sigma_j^2}\big]}{\sigma_i^2+\sigma_j^2}\int_0^\infty dk \exp\big[-kd-\frac{\sigma_i^2\sigma_j^2}{2(\sigma_i^2+\sigma_j^2)}k^2\big]\mathrm{J}_0\Big[k\Big|\frac{\sigma_j^2\vec{r}_A+\sigma_i^2\vec{r}_C}{\sigma_i^2+\sigma_j^2}-\vec{r}_B\Big|\Big] \tag{2.75}$$

2.6.1.4 Electron-electron matrix element

Starting from

$$\frac{1}{\pi^2\sigma_i\sigma_j\sigma_k\sigma_l}\int\int \exp\big[-\frac{|\vec{r}_{e1}-\vec{r}_A|^2}{2\sigma_i^2}\big]\exp\big[-\frac{|\vec{r}_{e1}-\vec{r}_C|^2}{2\sigma_k^2}\big]\frac{1}{\vec{r}_{e1}-\vec{r}_{e2}} \times \exp\big[-\frac{|\vec{r}_{e2}-\vec{r}_B|^2}{2\sigma_j^2}\big]\exp\big[-\frac{|\vec{r}_{e2}-\vec{r}_D|^2}{2\sigma_l^2}\big]d\vec{r}_{e1}d\vec{r}_{e2} \tag{2.76}$$

we combine the two pairs of Gaussians and insert the Fourier transform of the Coulomb potential to get

$$(2.76) = \frac{\exp\big[-\frac{|\vec{r}_A-\vec{r}_C|^2}{2(\sigma_i^2+\sigma_k^2)}-\frac{|\vec{r}_B-\vec{r}_D|^2}{2(\sigma_j^2+\sigma_l^2)}\big]}{\pi^2\sigma_i\sigma_j\sigma_k\sigma_l}\int\int \exp\Big[-\big(\frac{1}{2\sigma_i^2}+\frac{1}{2\sigma_k^2}\big)|\vec{r}_{e1}-\frac{\sigma_k^2\vec{r}_A+\sigma_i^2\vec{r}_C}{\sigma_i^2+\sigma_k^2}|^2\Big] \times \exp\Big[-\big(\frac{1}{2\sigma_j^2}+\frac{1}{2\sigma_l^2}\big)|\vec{r}_{e2}-\frac{\sigma_l^2\vec{r}_B+\sigma_j^2\vec{r}_D}{\sigma_j^2+\sigma_l^2}|^2\Big]\frac{1}{2\pi}\int\frac{\exp[-i\vec{k}\cdot(\vec{r}_{e1}-\vec{r}_{e2})]}{k}d\vec{k}d\vec{r}_{e1}d\vec{r}_{e2} \tag{2.77}$$

Let

$$X = \frac{\exp\big[-\frac{|\vec{r}_A-\vec{r}_C|^2}{2(\sigma_i^2+\sigma_k^2)}-\frac{|\vec{r}_B-\vec{r}_D|^2}{2(\sigma_j^2+\sigma_l^2)}\big]}{\pi^2\sigma_i\sigma_j\sigma_k\sigma_l} \tag{2.78}$$

We now take the Fourier transforms of both Gaussians to get

$$(2.76) = 2\pi X\frac{\sigma_i^2\sigma_k^2}{\sigma_i^2+\sigma_k^2}\frac{\sigma_j^2\sigma_l^2}{\sigma_j^2+\sigma_l^2}\int d\vec{k}\frac{1}{k} \times \exp\big[-\frac{k^2}{2}\big(\frac{\sigma_i^2\sigma_k^2}{\sigma_i^2+\sigma_k^2}+\frac{\sigma_j^2\sigma_l^2}{\sigma_j^2+\sigma_l^2}\big)\big]\exp\Big[-i\vec{k}\cdot\big(\frac{\sigma_k^2\vec{r}_A+\sigma_i^2\vec{r}_C}{\sigma_i^2+\sigma_k^2}-\frac{\sigma_l^2\vec{r}_B+\sigma_j^2\vec{r}_D}{\sigma_j^2+\sigma_l^2}\big)\Big] \tag{2.79}$$

$$= 2\pi X\frac{\sigma_i^2\sigma_k^2}{\sigma_i^2+\sigma_k^2}\frac{\sigma_j^2\sigma_l^2}{\sigma_j^2+\sigma_l^2}\int_0^\infty dk \exp\big[-\frac{k^2}{2}\big(\frac{\sigma_i^2\sigma_k^2}{\sigma_i^2+\sigma_k^2}+\frac{\sigma_j^2\sigma_l^2}{\sigma_j^2+\sigma_l^2}\big)\big] \times \int_0^{2\pi}d\theta\exp\Big[-ik\Big|\frac{\sigma_k^2\vec{r}_A+\sigma_i^2\vec{r}_C}{\sigma_i^2+\sigma_k^2}-\frac{\sigma_l^2\vec{r}_B+\sigma_j^2\vec{r}_D}{\sigma_j^2+\sigma_l^2}\Big|\cos\theta\Big] \tag{2.80}$$

The angular integral is a Bessel function, so

$$(2.76) = \frac{4\pi^2 X(\sigma_i\sigma_j\sigma_k\sigma_l)^2}{(\sigma_i^2+\sigma_k^2)(\sigma_j^2+\sigma_l^2)} \int_0^\infty dk \exp\big[-\frac{k^2}{2}\big(\frac{\sigma_i^2\sigma_k^2}{\sigma_i^2+\sigma_k^2}+\frac{\sigma_j^2\sigma_l^2}{\sigma_j^2+\sigma_l^2}\big)\big] \times \mathrm{J}_0\Big[k\Big|\frac{\sigma_k^2\vec{r}_A+\sigma_i^2\vec{r}_C}{\sigma_i^2+\sigma_k^2}-\frac{\sigma_l^2\vec{r}_B+\sigma_j^2\vec{r}_D}{\sigma_j^2+\sigma_l^2}\Big|\Big] \tag{2.81}$$

This is just a Gaussian integral, so the answer is

$$(2.76) = \frac{4\pi^2 X(\sigma_i\sigma_j\sigma_k\sigma_l)^2}{(\sigma_i^2+\sigma_k^2)(\sigma_j^2+\sigma_l^2)} \exp\left[-\frac{(\sigma_i^2+\sigma_k^2)(\sigma_j^2+\sigma_l^2)\left|\frac{\sigma_k^2\vec{r}_A+\sigma_i^2\vec{r}_C}{\sigma_i^2+\sigma_k^2}-\frac{\sigma_l^2\vec{r}_B+\sigma_j^2\vec{r}_D}{\sigma_j^2+\sigma_l^2}\right|^2}{4(\sigma_i^2\sigma_j^2\sigma_k^2+\sigma_i^2\sigma_j^2\sigma_l^2+\sigma_i^2\sigma_k^2\sigma_l^2+\sigma_j^2\sigma_k^2\sigma_l^2)}\right] \times \sqrt{\frac{\pi(\sigma_i^2+\sigma_k^2)(\sigma_j^2+\sigma_l^2)}{2(\sigma_i^2\sigma_j^2\sigma_k^2+\sigma_i^2\sigma_j^2\sigma_l^2+\sigma_i^2\sigma_k^2\sigma_l^2+\sigma_j^2\sigma_k^2\sigma_l^2)}} \times \mathrm{I}_0\left[\frac{(\sigma_i^2+\sigma_k^2)(\sigma_j^2+\sigma_l^2)\left|\frac{\sigma_k^2\vec{r}_A+\sigma_i^2\vec{r}_C}{\sigma_i^2+\sigma_k^2}-\frac{\sigma_l^2\vec{r}_B+\sigma_j^2\vec{r}_D}{\sigma_j^2+\sigma_l^2}\right|^2}{4(\sigma_i^2\sigma_j^2\sigma_k^2+\sigma_i^2\sigma_j^2\sigma_l^2+\sigma_i^2\sigma_k^2\sigma_l^2+\sigma_j^2\sigma_k^2\sigma_l^2)}\right] \tag{2.82}$$

where I_0 is a modified Bessel function of the first kind.

2.6.2 General orbitals

For states with $m > 0$, the single-particle orbitals are polynomials of x or y multiplied by Gaussians. The matrix elements are computed using moment generating functions. For the simplest case,

$$\hat{x}\cdot(\vec{r}_e-\vec{r}_a)\exp[-\frac{|\vec{r}_e-\vec{r}_a|^2}{2\sigma_i^2}] = \frac{d}{d\gamma}\Big(\exp[\sigma_i^2\gamma^2/2]\exp\big[-\frac{|\vec{r}_e-\vec{r}_a-\sigma_i^2\gamma\hat{x}|^2}{2\sigma_i^2}\big]\Big)\Big|_{\gamma=0} \tag{2.83}$$

2.6.2.1 Overlap matrix elements

The most general overlap matrix element between two orbitals is

$$\frac{1}{\pi\sigma_i\sigma_j}\int (x_e-x_a)^a\exp[-\frac{|\vec{r}_e-\vec{r}_a|^2}{2\sigma_i^2}](y_e-y_b)^b\exp[-\frac{|\vec{r}_e-\vec{r}_b|^2}{2\sigma_j^2}]d\vec{r}_e = \frac{d^a}{d\gamma_1^a}\frac{d^b}{d\gamma_2^b}\Big(\frac{2\exp[(\sigma_i^2\gamma_1^2+\sigma_j^2\gamma_2^2)/2]}{\sigma_i\sigma_j(\sigma_i^{-2}+\sigma_j^{-2})}\exp\Big[-\frac{|\vec{r}_a+\sigma_i^2\gamma_1\hat{x}-\vec{r}_b-\sigma_j^2\gamma_2\hat{y}|^2}{2\sigma_i^2+2\sigma_j^2}\Big]\Big)\Big|_{\gamma_1=\gamma_2=0} \tag{2.84}$$

For 2 p_x orbitals,

$$\frac{1}{\pi\sigma_i\sigma_j}\int (x_e-x_a)\exp[-\frac{|\vec{r}_e-\vec{r}_a|^2}{2\sigma_i^2}](x_e-x_b)\exp[-\frac{|\vec{r}_e-\vec{r}_b|^2}{2\sigma_j^2}]d\vec{r}_e = \frac{2\sigma_i^3\sigma_j^3(\sigma_i^2+\sigma_j^2-(x_a-x_b)^2)}{(\sigma_i^2+\sigma_j^2)^3}\exp[-\frac{|\vec{r}_a-\vec{r}_b|^2}{2\sigma_i^2+2\sigma_j^2}] \tag{2.85}$$

For p_x and p_y orbitals,

$$\frac{1}{\pi\sigma_i\sigma_j}\int (x_e-x_a)\exp[-\frac{|\vec{r}_e-\vec{r}_a|^2}{2\sigma_i^2}](y_e-y_b)\exp[-\frac{|\vec{r}_e-\vec{r}_b|^2}{2\sigma_j^2}]d\vec{r}_e = \frac{2\sigma_i^3\sigma_j^3(x_a-x_b)(y_a-y_b)}{(\sigma_i^2+\sigma_j^2)^3}\exp[-\frac{|\vec{r}_a-\vec{r}_b|^2}{2\sigma_i^2+2\sigma_j^2}] \tag{2.86}$$

For 2 s orbitals,

$$\frac{1}{\pi\sigma_i\sigma_j}\int \exp[-\frac{|\vec{r}_e-\vec{r}_a|^2}{2\sigma_i^2}]\exp[-\frac{|\vec{r}_e-\vec{r}_b|^2}{2\sigma_j^2}]d\vec{r}_e = \frac{2\sigma_i\sigma_j}{\sigma_i^2+\sigma_j^2}\exp[-\frac{|\vec{r}_a-\vec{r}_b|^2}{2\sigma_i^2+2\sigma_j^2}] \tag{2.87}$$

For s and p_x orbitals,

$$\frac{1}{\pi\sigma_i\sigma_j}\int \exp[-\frac{|\vec{r}_e-\vec{r}_a|^2}{2\sigma_i^2}](x_e-x_b)\exp[-\frac{|\vec{r}_e-\vec{r}_b|^2}{2\sigma_j^2}]d\vec{r}_e = \frac{2\sigma_i\sigma_j^3(x_a-x_b)}{(\sigma_i^2+\sigma_j^2)^2}\exp[-\frac{|\vec{r}_a-\vec{r}_b|^2}{2\sigma_i^2+2\sigma_j^2}] \tag{2.88}$$

For the overlap between four exciton orbitals, we start from

$$\begin{aligned}
&\frac{1}{\pi^2\sigma_i\sigma_j\sigma_k\sigma_l}\int (x_{e1}-x_a)^a\exp[-\frac{|\vec{r}_{e1}-\vec{r}_a|^2}{2\sigma_i^2}](y_{e1}-y_b)^b\exp[-\frac{|\vec{r}_{e1}-\vec{r}_b|^2}{2\sigma_j^2}](x_{e2}-x_c)^c\\
&\times\exp[-\frac{|\vec{r}_{e2}-\vec{r}_c|^2}{2\sigma_k^2}](y_{e2}-y_d)^d\exp[-\frac{|\vec{r}_{e2}-\vec{r}_d|^2}{2\sigma_l^2}]d\vec{r}_{e1}d\vec{r}_{e2}\\
&=\frac{d^a}{d\gamma_1^a}\frac{d^b}{d\gamma_2^b}\frac{d^c}{d\gamma_3^c}\frac{d^d}{d\gamma_4^d}\Big(\frac{4\exp[(\sigma_i^2\gamma_1^2+\sigma_j^2\gamma_2^2+\sigma_k^2\gamma_3^2+\sigma_l^2\gamma_4^2)/2]}{\sigma_i\sigma_j\sigma_k\sigma_l(\sigma_i^{-2}+\sigma_j^{-2})(\sigma_k^{-2}+\sigma_l^{-2})}\\
&\times\exp\Big[-\frac{|\vec{r}_a+\sigma_i^2\gamma_1\hat{x}-\vec{r}_b-\sigma_j^2\gamma_2\hat{y}|^2}{2\sigma_i^2+2\sigma_j^2}-\frac{|\vec{r}_c+\sigma_k^2\gamma_3\hat{x}-\vec{r}_d-\sigma_l^2\gamma_4\hat{y}|^2}{2\sigma_k^2+2\sigma_l^2}\Big]\Big)\Big|_{\gamma_1=\gamma_2=\gamma_3=\gamma_4=0}
\end{aligned} \tag{2.89}$$

2.6.2.2 Kinetic energy matrix element

The most general kinetic energy matrix element is

$$\begin{aligned}
&-\frac{1}{2m\pi\sigma_i\sigma_j}\int (x_e-x_a)^a\exp[-\frac{|\vec{r}_e-\vec{r}_a|^2}{2\sigma_i^2}]\nabla_e^2\Big\{(y_e-y_b)^b\exp[-\frac{|\vec{r}_e-\vec{r}_b|^2}{2\sigma_j^2}]\Big\}d\vec{r}_e\\
&=\frac{d^a}{d\gamma_1^a}\frac{d^b}{d\gamma_2^b}\Big(-\frac{\sigma_i^2\exp[(\sigma_i^2\gamma_1^2+\sigma_j^2\gamma_2^2)/2]}{m\sigma_i\sigma_j(\sigma_i^2+\sigma_j^2)}\exp\Big[-\frac{|\vec{r}_a+\sigma_i^2\gamma_1\hat{x}-\vec{r}_b-\sigma_j^2\gamma_2\hat{y}|^2}{2\sigma_i^2+2\sigma_j^2}\Big]\\
&\times\Big\{\frac{2\sigma_i^2}{\sigma_i^2+\sigma_j^2}+\frac{\sigma_j^2|\vec{r}_a+\sigma_i^2\gamma_1\hat{x}-\vec{r}_b-\sigma_j^2\gamma_2\hat{y}|^2}{(\sigma_i^2+\sigma_j^2)^2}-2\Big\}\Big)\Big|_{\gamma_1=\gamma_2=0}
\end{aligned} \tag{2.90}$$

For 2 p_x orbitals,

$$
\begin{aligned}
&-\frac{1}{2m\pi\sigma_i\sigma_j}\int (x_e-x_a)\exp[-\frac{|\vec{r}_e-\vec{r}_a|^2}{2\sigma_i^2}]\nabla_e^2\Big\{(x_e-x_b)\exp[-\frac{|\vec{r}_e-\vec{r}_b|^2}{2\sigma_j^2}]\Big\}d\vec{r}_e\\
&=\frac{\sigma_i^3\sigma_j^3}{m(\sigma_i^2+\sigma_j^2)^5}\exp\big[-\frac{|\vec{r}_a-\vec{r}_b|^2}{2\sigma_i^2+2\sigma_j^2}\big]\\
&\times\Big\{4(\sigma_i^2+\sigma_j^2)^2+(x_a-x_b)^2|\vec{r}_a-\vec{r}_b|^2-(\sigma_i^2+\sigma_j^2)\big(7(x_a-x_b)^2+(y_a-y_b)^2\big)\Big\}
\end{aligned}
\tag{2.91}
$$

For 2 p_y orbitals, we can replace every instance of $(x_a - x_b)$ with $(y_a - y_b)$ and vice versa. For p_x and p_y orbitals,

$$
\begin{aligned}
&-\frac{1}{2m\pi\sigma_i\sigma_j}\int (x_e-x_a)\exp[-\frac{|\vec{r}_e-\vec{r}_a|^2}{2\sigma_i^2}]\nabla_e^2\Big\{(y_e-y_b)\exp[-\frac{|\vec{r}_e-\vec{r}_b|^2}{2\sigma_j^2}]\Big\}d\vec{r}_e\\
&=\frac{\sigma_i^3\sigma_j^3}{m(\sigma_i^2+\sigma_j^2)^5}\exp\big[-\frac{|\vec{r}_a-\vec{r}_b|^2}{2\sigma_i^2+2\sigma_j^2}\big](x_a-x_b)(y_a-y_b)(|\vec{r}_a-\vec{r}_b|^2-6\sigma_i^2-6\sigma_j^2)
\end{aligned}
\tag{2.92}
$$

For 2 s orbitals,

$$
\begin{aligned}
&-\frac{1}{2m\pi\sigma_i\sigma_j}\int \exp[-\frac{|\vec{r}_e-\vec{r}_a|^2}{2\sigma_i^2}]\nabla_e^2\Big\{\exp[-\frac{|\vec{r}_e-\vec{r}_b|^2}{2\sigma_j^2}]\Big\}d\vec{r}_e\\
&=-\frac{\sigma_i}{m\sigma_j(\sigma_i^2+\sigma_j^2)}\exp\big[-\frac{|\vec{r}_a-\vec{r}_b|^2}{2\sigma_i^2+2\sigma_j^2}\big]\Big(\frac{2\sigma_i^2}{\sigma_i^2+\sigma_j^2}+\frac{\sigma_j^2|\vec{r}_a-\vec{r}_b|^2}{(\sigma_i^2+\sigma_j^2)^2}-2\Big)
\end{aligned}
\tag{2.93}
$$

For s and p_x orbitals,

$$
\begin{aligned}
&-\frac{1}{2m\pi\sigma_i\sigma_j}\int \exp[-\frac{|\vec{r}_e-\vec{r}_a|^2}{2\sigma_i^2}]\nabla_e^2\Big\{(x_e-x_b)\exp[-\frac{|\vec{r}_e-\vec{r}_b|^2}{2\sigma_j^2}]\Big\}d\vec{r}_e\\
&=-\frac{\sigma_i\sigma_j^3}{(\sigma_i^2+\sigma_j^2)^4}\exp\big[-\frac{|\vec{r}_a-\vec{r}_b|^2}{2\sigma_i^2+2\sigma_j^2}\big](x_a-x_b)(|\vec{r}_a-\vec{r}_b|^2-4\sigma_i^2-4\sigma_j^2)
\end{aligned}
\tag{2.94}
$$

Again, for s and p_y orbitals, we can replace the $(x_a - x_b)$ with $(y_a - y_b)$.

2.6.2.3 Electron-hole matrix element

The most general electron-hole matrix element is

$$
\begin{aligned}
&-\frac{1}{\pi\sigma_i\sigma_j}\int (x_e-x_a)^a \exp[-\frac{|\vec{r}_e-\vec{r}_a|^2}{2\sigma_i^2}]\Big(|\vec{r}_e-\vec{r}_b|^2+d^2\Big)^{-1/2}(y_e-y_c)^c \exp[-\frac{|\vec{r}_e-\vec{r}_c|^2}{2\sigma_j^2}]d\vec{r}_e \\
&\qquad = \frac{d^a}{d\gamma_1^a}\frac{d^c}{d\gamma_2^c}\left\{-\frac{2\sigma_i\sigma_j\exp[(\sigma_i^2\gamma_1^2+\sigma_j^2\gamma_2^2)/2]}{\sigma_i^2+\sigma_j^2}\exp\Big[-\frac{|\vec{r}_a+\sigma_i^2\gamma_1\hat{x}-\vec{r_c}-\sigma_j^2\gamma_2\hat{y}|^2}{2\sigma_i^2+2\sigma_j^2}\Big]\right. \\
&\times\int_0^\infty \exp\Big[-kd-\frac{\sigma_i^2\sigma_j^2k^2}{2\sigma_i^2+2\sigma_j^2}\Big]J_0\Big(k\left|\frac{\sigma_j^2(\vec{r}_a+\sigma_i^2\gamma_1\hat{x})+\sigma_i^2(\vec{r}_c+\sigma_j^2\gamma_2\hat{y})}{\sigma_i^2+\sigma_j^2}-\vec{r}_b\right|\Big)\Big\}_{\gamma_1=\gamma_2=0}
\end{aligned}
\tag{2.95}
$$

We can evaluate the last integral with Gauss-Laguerre quadrature:

$$
\int_0^\infty \exp[-x]f(x)dx \approx \sum_{i=1}^N w_i f(x_i) \tag{2.96}
$$

where x_i is the i^{th} root of the Laguerre polynomial $L_N(x)$ and the weight w_i is

$$
w_i = \frac{x_i}{(N+1)^2\big(L_{N+1}(x_i)\big)^2} \tag{2.97}
$$

For 2 p_x orbitals,

$$
\begin{aligned}
&-\frac{1}{\pi\sigma_i\sigma_j}\int (x_e-x_a)\exp[-\frac{|\vec{r}_e-\vec{r}_a|^2}{2\sigma_i^2}]\Big(|\vec{r}_e-\vec{r}_b|^2+d^2\Big)^{-1/2}(x_e-x_c)\exp[-\frac{|\vec{r}_e-\vec{r}_c|^2}{2\sigma_j^2}]d\vec{r}_e \\
&=\int_0^\infty dk\frac{\sigma_i^3\sigma_j^3}{(\sigma_i^2+\sigma_j^2)^3}\exp\Big[-\frac{\sigma_i^2\sigma_j^2k^2+2d(\sigma_i^2+\sigma_j^2)k+|\vec{r}_a-\vec{r}_c|^2}{2\sigma_i^2+2\sigma_j^2}\Big] \\
&\Big\{-2(\sigma_i^2+\sigma_j^2)J_0(k\xi)+2(x_a-x_c)^2J_0(k\xi)-\frac{2k\sigma_i^2\sigma_j^2}{\xi^{3/2}}\left(\frac{\sigma_j^2x_a+\sigma_i^2x_c}{\sigma_i^2+\sigma_j^2}-x_b\right)^2J_1(k\xi) \\
&+\frac{2k\sigma_i^2\sigma_j^2}{\xi}J_1(k\xi)+\frac{2k(\sigma_j^2-\sigma_i^2)(x_a-x_c)\big(\sigma_i^2(x_c-x_b)+\sigma_j^2(x_a-x_b)\big)}{(\sigma_i^2+\sigma_j^2)\xi}J_1(k\xi) \\
&+\frac{k^2\sigma_i^2\sigma_j^2\big(J_0(k\xi)-J_2(k\xi)\big)}{\xi^2}\left(\frac{\sigma_j^2x_a+\sigma_i^2x_c}{\sigma_i^2+\sigma_j^2}-x_b\right)^2\Big\}
\end{aligned}
\tag{2.98}
$$

where

$$
\xi = \left|\frac{\sigma_j^2\vec{r}_a+\sigma_i^2\vec{r}_c}{\sigma_i^2+\sigma_j^2}-\vec{r}_b\right| \tag{2.99}
$$

For 2 p_y orbitals, we replace x_i with y_i, for $i \in \{a,b,c\}$. If $\vec{r}_a$, $\vec{r}_b$, and $\vec{r}_c$ are all at the origin, we can't use (15); it would contain numerous indeterminate forms. The correct simplified expression is

$$-\frac{1}{\pi\sigma_i\sigma_j}\int(x_e-x_a)\exp[-\frac{|\vec{r}_e-\vec{r}_a|^2}{2\sigma_i^2}]\Big(|\vec{r}_e-\vec{r}_b|^2+d^2\Big)^{-1/2}(x_e-x_c)\exp[-\frac{|\vec{r}_e-\vec{r}_c|^2}{2\sigma_j^2}]d\vec{r}_e$$
$$=\int_0^\infty dk\frac{k^2\sigma_i^5\sigma_j^5-2(\sigma_i^3\sigma_j^5+\sigma_i^5\sigma_j^3)}{(\sigma_i^2+\sigma_j^2)^3}\exp\Big[-dk-\frac{\sigma_i^2\sigma_j^2}{2(\sigma_i^2+\sigma_j^2)}k^2\Big] \tag{2.100}$$

For p_x and p_y orbitals,

$$-\frac{1}{\pi\sigma_i\sigma_j}\int(x_e-x_a)\exp[-\frac{|\vec{r}_e-\vec{r}_a|^2}{2\sigma_i^2}]\Big(|\vec{r}_e-\vec{r}_b|^2+d^2\Big)^{-1/2}(y_e-y_c)\exp[-\frac{|\vec{r}_e-\vec{r}_c|^2}{2\sigma_j^2}]d\vec{r}_e$$
$$=\int_0^\infty dk\frac{\sigma_i^3\sigma_j^3}{(\sigma_i^2+\sigma_j^2)^3}\exp\Big[-\frac{\sigma_i^2\sigma_j^2k^2+2d(\sigma_i^2+\sigma_j^2)k+|\vec{r}_a-\vec{r}_c|^2}{2\sigma_i^2+2\sigma_j^2}\Big]$$
$$\{2(x_a-x_c)(y_a-y_c)J_0(k\xi)-\frac{2k\sigma_i^2\sigma_j^2}{\xi^{3/2}}\left(\frac{\sigma_j^2x_a+\sigma_i^2x_c}{\sigma_i^2+\sigma_j^2}-x_b\right)\left(\frac{\sigma_j^2y_a+\sigma_i^2y_c}{\sigma_i^2+\sigma_j^2}-y_b\right)J_1(k\xi)$$
$$+\frac{2kJ_1(k\xi)}{(\sigma_i^2+\sigma_j^2)\xi}$$
$$\times\Big[\sigma_i^2(x_a-x_c)\big(\sigma_j^2(y_b-y_a)+\sigma_i^2(y_b-y_c)\big)+\sigma_i^2(y_a-y_c)\big(\sigma_j^2(x_a-x_b)+\sigma_i^2(x_c-x_b)\big)\Big]$$
$$+\frac{k^2\sigma_i^2\sigma_j^2\big(J_0(k\xi)-J_2(k\xi)\big)}{\xi^2}\left(\frac{\sigma_j^2x_a+\sigma_i^2x_c}{\sigma_i^2+\sigma_j^2}-x_b\right)\left(\frac{\sigma_j^2y_a+\sigma_i^2y_c}{\sigma_i^2+\sigma_j^2}-y_b\right)\Big\} \tag{2.101}$$

For 2 s orbitals,

$$-\frac{1}{\pi\sigma_i\sigma_j}\int\exp[-\frac{|\vec{r}_e-\vec{r}_a|^2}{2\sigma_i^2}]\Big(|\vec{r}_e-\vec{r}_b|^2+d^2\Big)^{-1/2}\exp[-\frac{|\vec{r}_e-\vec{r}_c|^2}{2\sigma_j^2}]d\vec{r}_e$$
$$=-\frac{2\sigma_i\sigma_j}{\sigma_i^2+\sigma_j^2}\exp\Big[-\frac{|\vec{r}_a-\vec{r}_c|^2}{2(\sigma_i^2+\sigma_j^2)}\Big]\int_0^\infty dk\exp\Big[-kd-\frac{\sigma_i^2\sigma_j^2}{2(\sigma_i^2+\sigma_j^2)}k^2\Big]J_0(k\xi) \tag{2.102}$$

For s and p_x orbitals,

$$-\frac{1}{\pi\sigma_i\sigma_j}\int\exp[-\frac{|\vec{r}_e-\vec{r}_a|^2}{2\sigma_i^2}]\Big(|\vec{r}_e-\vec{r}_b|^2+d^2\Big)^{-1/2}(x_e-x_c)\exp[-\frac{|\vec{r}_e-\vec{r}_c|^2}{2\sigma_j^2}]d\vec{r}_e$$
$$=\frac{2\sigma_i\sigma_j^3}{\sigma_i^2+\sigma_j^2}\exp\Big[-\frac{|\vec{r}_a-\vec{r}_c|^2}{2(\sigma_i^2+\sigma_j^2)}\Big]\Big\{\frac{\sigma_i^2}{\xi(\sigma_i^2+\sigma_j^2)}\left(\frac{\sigma_j^2x_a+\sigma_i^2x_c}{\sigma_i^2+\sigma_j^2}-x_b\right)$$
$$\times\int_0^\infty dkk\exp\Big[-kd-\frac{\sigma_i^2\sigma_j^2}{2(\sigma_i^2+\sigma_j^2)}k^2\Big]J_1(k\xi)-\frac{2(x_a-x_c)}{2\sigma_i^2+2\sigma_j^2}$$
$$\times\int_0^\infty dk\exp\Big[-kd-\frac{\sigma_i^2\sigma_j^2}{2(\sigma_i^2+\sigma_j^2)}k^2\Big]J_0(k\xi)\Big\} \tag{2.103}$$

2.6.2.4 Electron-electron matrix element

We start from

$$\frac{1}{\pi^2\sigma_i\sigma_j\sigma_k\sigma_l}\int\int(x_{e1}-x_a)^a\exp[-\frac{|\vec{r}_{e1}-\vec{r}_a|^2}{2\sigma_i^2}](x_{e1}-x_b)^b\exp[-\frac{|\vec{r}_{e1}-\vec{r}_b|^2}{2\sigma_j^2}]$$
$$\times\frac{1}{|\vec{r}_{e1}-\vec{r}_{e2}|}(x_{e2}-x_c)^c\exp[-\frac{|\vec{r}_{e2}-\vec{r}_c|^2}{2\sigma_k^2}](x_{e2}-x_d)^d\exp[-\frac{|\vec{r}_{e2}-\vec{r}_d|^2}{2\sigma_l^2}]d\vec{r}_{e1}d\vec{r}_{e2}$$
$$=\frac{d^a}{d\gamma_1^a}\frac{d^b}{d\gamma_2^b}\frac{d^c}{d\gamma_3^c}\frac{d^d}{d\gamma_4^d}\Big\{\frac{4\sigma_i\sigma_j\sigma_k\sigma_l\exp[(\sigma_i^2\gamma_1^2+\sigma_j^2\gamma_2^2+\sigma_k^2\gamma_3^2+\sigma_l^2\gamma_4^2)/2]}{(\sigma_i^2+\sigma_j^2)(\sigma_k^2+\sigma_l^2)}$$
$$\times\exp\Big[-\frac{|\vec{r}_a+\sigma_i^2\gamma_1\hat{x}-\vec{r}_b-\sigma_j^2\gamma_2\hat{x}|^2}{2\sigma_i^2+2\sigma_j^2}-\frac{|\vec{r}_c+\sigma_k^2\gamma_3\hat{x}-\vec{r}_d-\sigma_l^2\gamma_4\hat{x}|^2}{2\sigma_k^2+2\sigma_l^2}-\frac{(\sigma_i^2+\sigma_j^2)(\sigma_k^2+\sigma_l^2)}{4\Sigma}\Gamma\Big]$$
$$\times\sqrt{\frac{\pi(\sigma_i^2+\sigma_j^2)(\sigma_k^2+\sigma_l^2)}{2\Sigma}}\mathrm{I}_0\Big(\frac{(\sigma_i^2+\sigma_j^2)(\sigma_k^2+\sigma_l^2)}{4\Sigma}\Gamma\Big)\Big\} \tag{2.104}$$

where

$$\Sigma=\sigma_i^2\sigma_j^2\sigma_k^2+\sigma_i^2\sigma_j^2\sigma_l^2+\sigma_i^2\sigma_k^2\sigma_l^2+\sigma_j^2\sigma_k^2\sigma_l^2 \tag{2.105}$$

$$\Gamma=\left|\frac{\sigma_j^2(\vec{r}_a+\sigma_i^2\gamma_1\hat{x})+\sigma_i^2(\vec{r}_b+\sigma_j^2\gamma_2\hat{x})}{\sigma_i^2+\sigma_j^2}-\frac{\sigma_l^2(\vec{r}_c+\sigma_k^2\gamma_3\hat{x})+\sigma_k^2(\vec{r}_d+\sigma_l^2\gamma_4\hat{x})}{\sigma_k^2+\sigma_l^2}\right|^2 \tag{2.106}$$

and $\mathrm{I}_0$is the zeroth-order modified Bessel function of the first kind.

For $a=b=c=d=0$ (i.e. all s orbitals),

$$\frac{1}{\pi^2\sigma_i\sigma_j\sigma_k\sigma_l}\int\int\exp[-\frac{|\vec{r}_{e1}-\vec{r}_a|^2}{2\sigma_i^2}]\exp[-\frac{|\vec{r}_{e1}-\vec{r}_b|^2}{2\sigma_j^2}]\frac{1}{|\vec{r}_{e1}-\vec{r}_{e2}|}$$
$$\times\exp[-\frac{|\vec{r}_{e2}-\vec{r}_c|^2}{2\sigma_k^2}]\exp[-\frac{|\vec{r}_{e2}-\vec{r}_d|^2}{2\sigma_l^2}]d\vec{r}_{e1}d\vec{r}_{e2}$$
$$=\frac{4\sigma_i\sigma_j\sigma_k\sigma_l}{(\sigma_i^2+\sigma_j^2)(\sigma_k^2+\sigma_l^2)}\exp\Big[-\frac{|\vec{r}_a-\vec{r}_b|^2}{2\sigma_i^2+2\sigma_j^2}-\frac{|\vec{r}_c-\vec{r}_d|^2}{2\sigma_k^2+2\sigma_l^2}-\frac{(\sigma_i^2+\sigma_j^2)(\sigma_k^2+\sigma_l^2)}{4\Sigma}\zeta\Big]$$
$$\times\sqrt{\frac{\pi(\sigma_i^2+\sigma_j^2)(\sigma_k^2+\sigma_l^2)}{2\Sigma}}\mathrm{I}_0\Big(\frac{(\sigma_i^2+\sigma_j^2)(\sigma_k^2+\sigma_l^2)}{4\Sigma}\zeta\Big) \tag{2.107}$$

where

$$\zeta=\left|\frac{\sigma_j^2\vec{r}_a+\sigma_i^2\vec{r}_b}{\sigma_i^2+\sigma_j^2}-\frac{\sigma_l^2\vec{r}_c+\sigma_k^2\vec{r}_d}{\sigma_k^2+\sigma_l^2}\right|^2 \tag{2.108}$$

For $a = 1$ and $b = c = d = 0$,

$$\begin{aligned}
&\frac{1}{\pi^2\sigma_i\sigma_j\sigma_k\sigma_l}\int\int(x_{e1}-x_a)\exp[-\frac{|\vec{r}_{e1}-\vec{r}_a|^2}{2\sigma_i^2}]\exp[-\frac{|\vec{r}_{e1}-\vec{r}_b|^2}{2\sigma_j^2}]\frac{1}{|\vec{r}_{e1}-\vec{r}_{e2}|}\\
&\times\exp[-\frac{|\vec{r}_{e2}-\vec{r}_c|^2}{2\sigma_k^2}]\exp[-\frac{|\vec{r}_{e2}-\vec{r}_d|^2}{2\sigma_l^2}]d\vec{r}_{e1}d\vec{r}_{e2}\\
&=\frac{\sqrt{2\pi}\sigma_i^3\sigma_j\sigma_k\sigma_l(\sigma_k^2+\sigma_l^2)}{\big((\sigma_i^2+\sigma_j^2)(\sigma_k^2+\sigma_l^2)\Sigma\big)^{3/2}}\exp\Big[-\frac{|\vec{r}_a-\vec{r}_b|^2}{2\sigma_i^2+2\sigma_j^2}-\frac{|\vec{r}_c-\vec{r}_d|^2}{2\sigma_k^2+2\sigma_l^2}-\frac{(\sigma_i^2+\sigma_j^2)(\sigma_k^2+\sigma_l^2)}{4\Sigma}\zeta\Big]\\
&\times\Big\{-\Big(2\Sigma(x_a-x_b)+\sigma_j^2\big((\sigma_k^2+\sigma_l^2)(\sigma_j^2x_a+\sigma_i^2x_b)-(\sigma_i^2+\sigma_j^2)(\sigma_l^2x_c+\sigma_k^2x_d)\big)\Big)\\
&\times\mathrm{I}_0\Big(\frac{(\sigma_i^2+\sigma_j^2)(\sigma_k^2+\sigma_l^2)}{4\Sigma}\zeta\Big)+\sigma_j^2\big((\sigma_k^2+\sigma_l^2)(\sigma_j^2x_a+\sigma_i^2x_b)-(\sigma_i^2+\sigma_j^2)(\sigma_l^2x_c+\sigma_k^2x_d)\big)\Big)\\
&\times\mathrm{I}_1\Big(\frac{(\sigma_i^2+\sigma_j^2)(\sigma_k^2+\sigma_l^2)}{4\Sigma}\zeta\Big)\Big\}
\end{aligned}\tag{2.109}$$

If $b = 1$ and $a = c = d = 0$, we make the replacements $\sigma_i \to \sigma_j$, $\sigma_j \to \sigma_i$, $x_a \to x_b$, and $x_b \to x_a$. For $c = 1$ and $a = b = d = 0$,

$$\begin{aligned}
&\frac{1}{\pi^2\sigma_i\sigma_j\sigma_k\sigma_l}\int\int\exp[-\frac{|\vec{r}_{e1}-\vec{r}_a|^2}{2\sigma_i^2}]\exp[-\frac{|\vec{r}_{e1}-\vec{r}_b|^2}{2\sigma_j^2}]\frac{1}{|\vec{r}_{e1}-\vec{r}_{e2}|}\\
&\times(x_{e2}-x_c)\exp[-\frac{|\vec{r}_{e2}-\vec{r}_c|^2}{2\sigma_k^2}]\exp[-\frac{|\vec{r}_{e2}-\vec{r}_d|^2}{2\sigma_l^2}]d\vec{r}_{e1}d\vec{r}_{e2}\\
&=\frac{\sqrt{2\pi}\sigma_i\sigma_j\sigma_k^3\sigma_l(\sigma_i^2+\sigma_j^2)}{\big((\sigma_i^2+\sigma_j^2)(\sigma_k^2+\sigma_l^2)\Sigma\big)^{3/2}}\exp\Big[-\frac{|\vec{r}_a-\vec{r}_b|^2}{2\sigma_i^2+2\sigma_j^2}-\frac{|\vec{r}_c-\vec{r}_d|^2}{2\sigma_k^2+2\sigma_l^2}-\frac{(\sigma_i^2+\sigma_j^2)(\sigma_k^2+\sigma_l^2)}{4\Sigma}\zeta\Big]\\
&\times\Big\{-\Big(2\Sigma(x_c-x_d)+\sigma_l^2\big((\sigma_i^2+\sigma_j^2)(\sigma_l^2x_c+\sigma_k^2x_d)-(\sigma_k^2+\sigma_l^2)(\sigma_j^2x_a+\sigma_i^2x_b)\big)\Big)\\
&\times\mathrm{I}_0\Big(\frac{(\sigma_i^2+\sigma_j^2)(\sigma_k^2+\sigma_l^2)}{4\Sigma}\zeta\Big)+\sigma_l^2\big((\sigma_i^2+\sigma_j^2)(\sigma_l^2x_c+\sigma_k^2x_d)-(\sigma_k^2+\sigma_l^2)(\sigma_j^2x_a+\sigma_i^2x_b)\big)\Big)\\
&\times\mathrm{I}_1\Big(\frac{(\sigma_i^2+\sigma_j^2)(\sigma_k^2+\sigma_l^2)}{4\Sigma}\zeta\Big)\Big\}
\end{aligned}\tag{2.110}$$

The $d = 1$ and $a = b = c = 0$ case can be obtained through analogous replacements. Also, if a p_y orbital is used, then each x-coordinate should be a y-coordinate.

2.7 Appendix: optimal scaling factors

Table 2.1 contains the optimal scaling factors for our Gaussian basis set for indirect excitons when calculating biexciton states. The values were optimized for two excitons separated by the equilibrium biexciton bond length R_{eq}. We first optimized the 1s states by computing the biexciton energy on a grid of ξ with a spacing of $\Delta\xi = 0.1$ and choosing the value which

d (a_{ex})	1s factor	$2p_x$ factor	$2p_y$ factor	2s factor	R_{eq} (a_{ex})
0	1.3	0.8	1.0	4.6	0.4
0.05	1.2	0.6	5.0	3.7	0.55
0.1	1.1	3.8	4.1	3.2	0.7
0.2	1.1	3.1	3.4	2.7	1.0
0.3	1.0	2.5	2.8	2.5	1.3
0.4	1.0	2.3	2.5	2.2	1.7
0.5	1.0	2.1	2.3	2.0	2.0
0.6	1.0	2.0	2.2	1.9	2.3
0.7	1.0	1.9	2.1	1.7	2.7
0.8	1.0	1.8	1.9	1.5	3.1
0.9	1.0	1.7	1.8	1.3	3.8

Table 2.1: Optimal scaling factors for our Gaussian basis sets.

minimized the energy. We then worked up to the 2p and 2s states, and we included the previously optimized states at each level. After a first pass, we re-optimized the factors until we found a local minimum in the biexciton energy.

Chapter 3

A pair of 2D quantum liquids: the electron-hole liquid in a bilayer geometry

3.1 Introduction

In this chapter, we consider the electron-hole liquid formed by indirect excitons. The EHL has been studied using nearly every method applicable to studying the degenerate electron gas: Green's-function techniques [33,68,69], the many-body variational approach [70], and path integral Monte Carlo [39], to name a few. We take the first approach, first calculating the ground-state energy within the random-phase approximation and finding good agreement between the binding energy per particle in the EHL and the photoluminescence red-shift measured by Bar-Joseph *et al.* [42,43]. Notably, we determine that the classical mean-field capacitor term dictates how the total energy varies with the bilayer separation. Proceeding to finite temperatures, we calculate the correlation free energy using the linked cluster expansion.

3.2 Model

We consider N electrons and N holes restricted to their own infinitely-thin planes of area $A = L^2$ separated by d (see Fig. 1.4). In this Chapter, we neglect bound exciton states. We solve the law of mass action in Chapter 4 to determine the fraction of free carriers relative to the total number of carriers at thermal equilibrium. We will see that no excitons are present at the high densities of the electron-hole liquid, allowing us to safely neglect bound excitons.

The first-quantized Hamiltonian is a straightforward extension of the indirect biexciton

or triexciton Hamiltonians given by Eq. (2.1) or (2.38):

$$H = -\frac{\hbar^2}{2m_e}\sum_{i=1}^{N}\nabla_{e,i}^2 - \frac{\hbar^2}{2m_h}\sum_{i=1}^{N}\nabla_{h,i}^2 + \frac{e^2}{2(4\pi\epsilon_0\epsilon)}\sum_{i,\neq j}^{N}\frac{1}{|\mathbf{r}_{e,i}-\mathbf{r}_{e,j}|} + \frac{e^2}{2(4\pi\epsilon_0\epsilon)}\sum_{i\neq j}^{N}\frac{1}{|\mathbf{r}_{h,i}-\mathbf{r}_{h,j}|} - \frac{e^2}{(4\pi\epsilon_0\epsilon)}\sum_{i,j}^{N}\frac{1}{\sqrt{|\mathbf{r}_{e,i}-\mathbf{r}_{h,j}|^2+d^2}} \tag{3.1}$$

To utilize Green's function methods, we recast this Hamiltonian in second quantization. For a general all-electron Hamiltonian [18],

$$H = \sum_i T(r_i) + \frac{1}{2}\sum_{i\neq j} V(r_i - r_j) \tag{3.2}$$

is written in second quantization as

$$H = \sum_{r,s}\langle r|\,T\,|s\rangle\, a_r^\dagger a_s + \frac{1}{2}\sum_{r,s,t,u}\langle rs|\,V\,|tu\rangle\, a_r^\dagger a_s^\dagger a_u a_t \tag{3.3}$$

where $a_r^\dagger$ (a_r) creates (destroys) an electron indexed by the quantum number(s) r. These fermionic creation and annihilation operators are completely defined by the anticommutation rule

$$\{a_k, a_{k'}^\dagger\} = a_k a_{k'}^\dagger + a_{k'}^\dagger a_k \tag{3.4}$$

$$= \delta_{k,k'} \tag{3.5}$$

For our two-component system, we must also introduce the operators $b_r^\dagger$ and b_r which create and destroy a hole, respectively. These operators obey a similar anticommutation rule.

Because our system is translationally invariant, we enforce periodic boundary conditions and take our single-particle basis to be plane waves:

$$\psi_{k,\xi}(\mathbf{r}) = \frac{1}{\sqrt{A}}e^{i\mathbf{k}\cdot\mathbf{r}}\eta_\xi \tag{3.6}$$

The allowed wavevectors are

$$k_i = \frac{2\pi n_i}{L} \quad n_i = 0, \pm1, \pm2, ... \tag{3.7}$$

the spin functions indexed by the quantum number ξ are

$$\eta_\uparrow = \begin{bmatrix} 1 \\ 0 \end{bmatrix} \tag{3.8}$$

$$\eta_\downarrow = \begin{bmatrix} 0 \\ 1 \end{bmatrix} \tag{3.9}$$

and the non-interacting single-particle energies are

$$\varepsilon_{i,k} = \frac{\hbar^2 k^2}{2m_i} \tag{3.10}$$

where m_i is the mass of a particle of type i.

Since our basis is a set of plane waves, the matrix elements in Eq. (3.3) are the Fourier transforms of the kinetic and potential energies. The kinetic energy matrix elements are just the single-particle energies. On the other hand, the Fourier transform of the potential energy terms is more complicated and subtle.

3.2.1 Capacitor term

Before evaluating the potential energy matrix element, we introduce exponential convergence factors to regularize the Coulomb interactions. Specifically, each Coulombic term in Eq. (3.1) individually diverges in the thermodynamic limit, but their sum is finite. After dropping the factors of $e^2/(4\pi\epsilon_0\epsilon)$, the potential energy in first quantization is

$$V = \frac{1}{2}\sum_{i\neq j}^{N} \frac{\exp[-\mu|\mathbf{r}_{e,i}-\mathbf{r}_{e,j}|]}{\epsilon|\mathbf{r}_{e,i}-\mathbf{r}_{e,j}|} + \frac{1}{2}\sum_{i\neq j}^{N} \frac{\exp[-\mu|\mathbf{r}_{h,i}-\mathbf{r}_{h,j}|]}{\epsilon|\mathbf{r}_{h,i}-\mathbf{r}_{h,j}|} - \sum_{i,j}^{N} \frac{\exp[-\mu|\mathbf{r}_{e,i}-\mathbf{r}_{h,j}|]}{\epsilon\sqrt{|\mathbf{r}_{e,i}-\mathbf{r}_{h,j}|^2+d^2}} \tag{3.11}$$

We now turn to the required matrix element.

$$\begin{aligned}\langle \mathbf{k}_1\xi_1\mathbf{k}_2\xi_2|\, V\, |\mathbf{k}_3\xi_3\mathbf{k}_4\xi_4\rangle = \frac{1}{\epsilon A^2}\delta_{\xi_1,\xi_3}\delta_{\xi_2,\xi_4}\int d\mathbf{r}_1\int d\mathbf{r}_2 \exp[-i(\mathbf{k}_1\cdot\mathbf{r}_1+\mathbf{k}_2\cdot\mathbf{r}_2)] \\ \times \exp[i(\mathbf{k}_3\cdot\mathbf{r}_1+k_4\cdot\mathbf{r}_2)]\Big\{\frac{\exp[-\mu|\mathbf{r}_1-\mathbf{r}_2|]}{|\mathbf{r}_1-\mathbf{r}_2|} - \frac{\exp[-\mu|\mathbf{r}_1-\mathbf{r}_2|]}{\sqrt{|\mathbf{r}_1-\mathbf{r}_2|^2+d^2}}\Big\}\end{aligned} \tag{3.12}$$

Let $\mathbf{r} = \mathbf{r}_2$ and $\mathbf{y} = \mathbf{r}_1 - \mathbf{r}_2$, so

$$\begin{aligned}\langle \mathbf{k}_1\xi_1\mathbf{k}_2\xi_2|\, V\, |\mathbf{k}_3\xi_3\mathbf{k}_4\xi_4\rangle = \frac{1}{\epsilon A^2}\delta_{\xi_1,\xi_3}\delta_{\xi_2,\xi_4}\int d\mathbf{r}\exp[-i(\mathbf{k}_1+\mathbf{k}_2-\mathbf{k}_3-\mathbf{k}_4)\cdot\mathbf{r}] \\ \times \int d\mathbf{y}\exp[i(\mathbf{k}_3-\mathbf{k}_1)\cdot\mathbf{y}]\Big\{\frac{\exp[-\mu y]}{y} - \frac{\exp[-\mu y]}{\sqrt{y^2+d^2}}\Big\}\end{aligned} \tag{3.13}$$

The $\mathbf{r}$-integral gives an area times a Kronecker δ-function which guarantees momentum conservation. Let $\mathbf{q} = \mathbf{k}_1 - \mathbf{k}_3$ be the momentum transferred in the two-particle interaction.

$$\begin{aligned}\langle \mathbf{k}_1\xi_1\mathbf{k}_2\xi_2|\, V\, |\mathbf{k}_3\xi_3\mathbf{k}_4\xi_4\rangle = \frac{1}{\epsilon A}\delta_{\xi_1,\xi_3}\delta_{\xi_2,\xi_4}\delta_{\mathbf{k}_1+\mathbf{k}_2,\mathbf{k}_3+\mathbf{k}_4} \\ \times \int_0^\infty dy\int_0^{2\pi} d\theta\, y\exp[-iqy\cos\theta]\Big\{\frac{\exp[-\mu y]}{y} - \frac{\exp[-\mu y]}{\sqrt{y^2+d^2}}\Big\}\end{aligned} \tag{3.14}$$

Let's first address the $q = 0$ case. After evaluating the θ-integral,

$$\langle \mathbf{k}_1\xi_1\mathbf{k}_2\xi_2|\, V\, |\mathbf{k}_3\xi_3\mathbf{k}_4\xi_4\rangle = \frac{1}{\epsilon A^2}\delta_{\xi_1,\xi_3}\delta_{\xi_2,\xi_4}\delta_{\mathbf{k}_1+\mathbf{k}_2,\mathbf{k}_3+\mathbf{k}_4} \times \int_0^\infty dy\Big\{ \exp[-\mu y] - \frac{y\exp[-\mu y]}{\sqrt{y^2+d^2}}\Big\} \quad \text{for } q=0 \tag{3.15}$$

Turning to the y-integral, we first consider

$$\int_0^L dy \frac{y}{\sqrt{y^2+d^2}} \tag{3.16}$$

where we will later take $L \to \infty$. Letting $u = y^2$,

$$\int_0^L dy \frac{y}{\sqrt{y^2+d^2}} = \frac{1}{2}\int_0^{L^2} du \frac{u}{\sqrt{u+d^2}} \tag{3.17}$$

$$= \sqrt{u+d^2}\Big|_{u=0}^{u=L^2} \tag{3.18}$$

$$= \sqrt{L^2+d^2} - d \tag{3.19}$$

$$= L\Big(1 + \frac{1}{2}\big(\frac{d}{L}\big)^2 + ...\Big) - d \tag{3.20}$$

In the thermodynamic limit (*i.e.*, large L/d),

$$\int_0^L dy \frac{y}{\sqrt{y^2+d^2}} = L - d \tag{3.21}$$

so

$$\lim_{L\to\infty}\int_0^L dy\Big\{1 - \frac{y}{\sqrt{y^2+d^2}}\Big\} = d \tag{3.22}$$

We can add the convergence factor without effect:

$$\lim_{\mu\to 0}\int_0^\infty dy\Big\{ \exp[-\mu y] - \frac{y\exp[-\mu y]}{\sqrt{y^2+d^2}}\Big\} = d \tag{3.23}$$

Therefore,

$$\langle \mathbf{k}_1\xi_1\mathbf{k}_2\xi_2|\, V\, |\mathbf{k}_3\xi_3\mathbf{k}_4\xi_4\rangle = \frac{2\pi d}{\epsilon A}\delta_{\xi_1,\xi_3}\delta_{\xi_2,\xi_4}\delta_{\mathbf{k}_1+\mathbf{k}_2,\mathbf{k}_3+\mathbf{k}_4} \tag{3.24}$$

For the $q \neq 0$ case, we can set $\mu = 0$ in Eq. (3.14) and introduce a Bessel function of order zero to get

$$\langle \mathbf{k}_1\xi_1\mathbf{k}_2\xi_2|\, V\, |\mathbf{k}_3\xi_3\mathbf{k}_4\xi_4\rangle = \frac{2\pi}{\epsilon A}\delta_{\xi_1,\xi_3}\delta_{\xi_2,\xi_4}\delta_{\mathbf{k}_1+\mathbf{k}_2,\mathbf{k}_3+\mathbf{k}_4}\int_0^\infty dy J_0(qy)\Big\{1 - \frac{y}{\sqrt{y^2+d^2}}\Big\} \quad \text{for } q\neq 0 \tag{3.25}$$

$$= \frac{2\pi}{\epsilon A}\delta_{\xi_1,\xi_3}\delta_{\xi_2,\xi_4}\delta_{\mathbf{k}_1+\mathbf{k}_2,\mathbf{k}_3+\mathbf{k}_4}\Big\{\frac{1}{q} - \frac{\exp[-qd]}{q}\Big\} \tag{3.26}$$

Putting everything together and reintroducing the factors of $e^2/(4\pi\epsilon_0\epsilon)$, the second-quantized Coulomb interaction is

$$V = \frac{e^2\pi}{4\pi\epsilon_0\epsilon A}\sum_{\mathbf{k}\neq 0}\sum_{\mathbf{k},\mathbf{p}}\sum_{\xi_1,\xi_2}\Big\{\frac{1}{q}a^\dagger_{\mathbf{k}+\mathbf{q},\xi_1}a^\dagger_{\mathbf{p}-\mathbf{q},\xi_2}a_{\mathbf{p},\xi_2}a_{\mathbf{k},\xi_1} + \frac{1}{q}b^\dagger_{\mathbf{k},\xi_1}b^\dagger_{\mathbf{p},\xi_2}b_{\mathbf{p}-\mathbf{q},\xi_2}b_{\mathbf{k}+\mathbf{q},\xi_1} - \frac{2\exp[-qd]}{q}a^\dagger_{\mathbf{k}+\mathbf{q},\xi_1}b^\dagger_{\mathbf{p},\xi_2}b_{\mathbf{p}-\mathbf{q},\xi_2}a_{\mathbf{k},\xi_1}\Big\} + \frac{2\pi e^2N^2d}{4\pi\epsilon_0\epsilon A} \tag{3.27}$$

and the total Hamiltonian is

$$\begin{aligned} H = &\sum_{\mathbf{k}}\frac{\hbar^2k^2}{2m_e}a^\dagger_{\mathbf{k}}a_{\mathbf{k}} + \sum_{\mathbf{k}}\frac{\hbar^2k^2}{2m_h}b^\dagger_{\mathbf{k}}b_{\mathbf{k}} \\ &+ \frac{e^2\pi}{4\pi\epsilon_0\epsilon A}\sum_{\mathbf{q}\neq 0}\sum_{\mathbf{k},\mathbf{p}}\sum_{\xi_1,\xi_2}\Big\{\frac{1}{q}a^\dagger_{\mathbf{k}+\mathbf{q},\xi_1}a^\dagger_{\mathbf{p}-\mathbf{q},\xi_2}a_{\mathbf{p},\xi_2}a_{\mathbf{k},\xi_1} + \frac{1}{q}b^\dagger_{\mathbf{k},\xi_1}b^\dagger_{\mathbf{p},\xi_2}b_{\mathbf{p}-\mathbf{q},\xi_2}b_{\mathbf{k}+\mathbf{q},\xi_1} \\ &- \frac{2\exp[-qd]}{q}a^\dagger_{\mathbf{k}+\mathbf{q},\xi_1}b^\dagger_{\mathbf{p},\xi_2}b_{\mathbf{p}-\mathbf{q},\xi_2}a_{\mathbf{k},\xi_1}\Big\} + \frac{2\pi e^2N^2d}{4\pi\epsilon_0\epsilon A} \end{aligned} \tag{3.28}$$

The last term– the $q = 0$ contribution to the potential energy– is a classical mean-field result. It is the energy associated with two parallel plates separated by d each possessing a uniform charge density which is equal and opposite in sign (*i.e.*, the energy of a parallel plate capacitor). We now write this in terms of Ry_{ex}, defined in Eq. (1.7). Instead of working with the carrier density $n = N/A$, it is customary to use r_s, the dimensionless interparticle spacing measured in a_{ex}, defined in Eq. (1.4). In two dimensions, these are related by

$$N\pi r_s^2 a_{ex}^2 = A \tag{3.29}$$

$$na_{ex}^2 = \frac{1}{\pi r_s^2} \tag{3.30}$$

The density is also related to the Fermi wavevector k_F, the largest wavevector accessed by non-interacting particles at zero temperature. To derive this relation, we start by calculating the total number of particles:

$$N = \sum_{k,\lambda} f(k,\beta,\mu) \tag{3.31}$$

where the Fermi-Dirac distribution for a general particle of type i is

$$f_i(k,\beta,\mu) = \frac{\exp[-\beta(\varepsilon_{i,k}-\mu)]}{\exp[-\beta(\varepsilon_{i,k}-\mu)]+1} \tag{3.32}$$

$\beta^{-1} = k_BT$, and μ is the chemical potential. At zero temperature, the distributions for both the electrons and holes reduce to a Heaviside step function, so

$$N_i = \sum_{k,\xi}\Theta(k-k_{F_i}) \tag{3.33}$$

In the thermodynamic limit, the spacing between wavevectors vanishes (*cf.* Eq. (3.7) as $L \to \infty$), so we can replace the momentum sum with an integral following the rule

$$\sum_{k,\xi} h(k) \to \sum_{\xi} \frac{L^d}{(2\pi)^d} \int d^d k h(k) \tag{3.34}$$

where $d = 2$ is the dimensionality of the system [18]. Thus,

$$N_i = \sum_{\xi} \frac{A}{(2\pi)^2} \int d^2 k \Theta(k - k_{F_i}) \tag{3.35}$$

$$= \frac{2A}{(2\pi)^2} \int_0^{k_{F_i}} 2\pi k dk \tag{3.36}$$

$$= \frac{A k_{F_i}^2}{2\pi} \tag{3.37}$$

$$n_i = \frac{k_{F_i}^2}{2\pi} \tag{3.38}$$

For a general system with ν_i bands for particle i [71],

$$\frac{n_i}{\nu_i} = \frac{k_{F_i}^2}{2\pi} \tag{3.39}$$

Combining Eq. (3.30) and (3.38), we get

$$k_F a_{ex} = \frac{\sqrt{2}}{r_s} \tag{3.40}$$

or in general,

$$k_{F_i} a_{ex} = \frac{\sqrt{2}}{\sqrt{\nu_i} r_s} \tag{3.41}$$

Therefore, the capacitor energy per particle is

$$E_{\text{cap}} = \frac{4d'}{r_s^2} Ry_{ex} \tag{3.42}$$

where $d' = d/a_{ex}$.

3.3 Zero temperature theory

There are four contributions to the ground state energy of Eq. (3.28):

$$E_{\text{tot}} = E_{\text{kin}} + E_{\text{exch}} + E_{\text{cor}} + E_{\text{cap}} \tag{3.43}$$

The kinetic and exchange energies (E_{kin} and E_{exch}, respectively) can be computed exactly. In contrast, the correlation energy (E_{cor}) can be written as an infinite series in the coupling constant of the Coulomb potential and can only be solved approximately. In this section, we use the random-phase approximation and sum all possible ring diagrams [18,72]. One can improve upon these calculations by taking into account the immediate surroundings of each electron (*i.e.*, the exchange-correlation hole). Hubbard [73], Nozieres & Pines [74], and Singwi *et al.* [75] have each proposed local field or vertex corrections to the polarization rings. Alternatively, one can evaluate the thermodynamic potential for arbitrary T and chemical potential μ and then take the limit $T \to 0$. Using the linked-cluster theorem [72], the thermodynamic potential is expressed in terms of ring diagrams similar to the zero temperature case in addition to new anomalous diagrams. This approach includes more diagrams and is more accurate because it uses the exact chemical potential for the interacting system. In contrast, the zero temperature approach uses the Fermi energy of the unperturbed system [18].

3.3.1 Kinetic energy

To calculate the total kinetic energy of an electron-hole liquid at zero temperature, we simply add up the contributions from each electron and hole [33]:

$$E_{\text{kin}} = \sum_{i=e,h} \nu_i \xi_i \sum_{k<k_{F_i}} \frac{\hbar^2 k^2}{2m_i} \tag{3.44}$$

We can write the sum as an integral following Eq. (3.34).

$$E_{\text{kin}} = \sum_{i=e,h} \nu_i \xi_i \frac{\hbar^2}{2m_i} \frac{A}{(2\pi)^2} \int_0^{k_{F_i}} 2\pi k(k^2) dk \tag{3.45}$$

$$= \sum_{i=e,h} \nu_i \xi_i \frac{\hbar^2}{2m_i} \frac{A}{2\pi} \frac{k_{F_i}^4}{4} \tag{3.46}$$

Using Eq. (3.39),

$$E_{\text{kin}} = \sum_{i=e,h} \nu_i \xi_i \frac{\hbar^2 k_{F_i}^2}{2m_i} \frac{N}{\nu_i 4} \tag{3.47}$$

$$\frac{E_{kin}}{N} = \frac{\hbar^2}{2} \Big(\frac{\xi_e k_{F_e}^2}{2m_e} + \frac{\xi_h k_{F_h}^2}{2m_h} \Big) \tag{3.48}$$

Using Eq. (3.40), this can be written in Ry_{ex} as

$$\frac{E_{\text{kin}}}{N} = \frac{1}{4r_s^2} \Big(\frac{\xi_e}{\nu_e} \frac{1}{\sigma+1} + \frac{\xi_h}{\nu_h} \frac{\sigma}{\sigma+1} \Big) Ry_{ex} \tag{3.49}$$

For our model, $\nu_e = \nu_h = 1$ and $\xi_e = \xi_h = 2$, so

$$\frac{E_{\text{kin}}}{N} = \frac{1}{r_s^2} Ry_{ex} \tag{3.50}$$

3.3.2 Exchange energy

To compute the zero-temperature exchange energy to first order, we evaluate the potential energy matrix element with the Hartree-Fock state. For an all-electron system, this is a Slater determinant of the single-particle states given by Eq. (3.6). For the EHL, the Hartree-Fock state is a product of two of these determinants: one for the electrons and one for the holes. The matrix element reduces to two terms: one is the capacitor energy (sometimes called the "direct" term) and the other is the exchange energy [18,33]

$$E_{\text{exch}} = -\sum_{i=e,h} \frac{\nu_i \xi_i}{2A} \sum_{\mathbf{k},\mathbf{p}} U^0(\mathbf{k}-\mathbf{p}) f_i(k, \beta \to \infty, \mu) f_i(p, \beta \to \infty, \mu) \tag{3.51}$$

where we have the Fourier transform of the statically-screened two-dimensional Coulomb interaction

$$U^0(k) = \frac{2\pi e^2}{4\pi\epsilon_0 \epsilon k} \tag{3.52}$$

As before, the Fermi distributions reduce to Heaviside step functions at zero temperature. The result is [76]

$$\frac{E_{\text{exch}}}{N} = -\sum_{i=e,h} \frac{8\sqrt{2}}{3\pi r_s} Ry_{ex} \tag{3.53}$$

$$= -\frac{2.401}{r_s} Ry_{ex} \tag{3.54}$$

3.3.3 Correlation energy

The difference between the total ground state energy and the energy calculated using the non-interacting Hartree-Fock state is defined as the correlation energy. For $q = 0$, the correlation energy is equivalent to the capacitor energy. In strictly two dimensions ($d = 0$), the $q \neq 0$ contribution is given exactly by [18]

$$E_{\text{cor}} = \frac{\hbar i A}{2(2\pi)^3} \int_0^1 \frac{d\lambda}{\lambda} \int d^2k \int d\omega \Big[\epsilon_\lambda(k,\omega)^{-1} - 1 - \lambda U^0(k) \big(\Pi_e^0(k,\omega) + \Pi_h^0(k,\omega) \big) \Big] \tag{3.55}$$

λ is a coupling constant that scales the bare Coulomb interactions, Eq. (3.52), ω is the frequency, Π_i^0 is the lowest-order polarization for particle i,

$$\epsilon_\lambda(k,\omega) = 1 - \lambda U^0(k) \big(\Pi_e^{\lambda,*}(k,\omega) + \Pi_h^{\lambda,*}(k,\omega) \big) \tag{3.56}$$

is the dielectric function, and $\Pi_i^{\lambda,*}(k,\omega)$ the proper polarization for particle i. Working within the random-phase approximation, we approximate the proper polarization to lowest order and subsequently suppress the superscript: $\Pi^* \approx \Pi^0 \equiv \Pi$. In this case, Eq. (3.55) can be written as

$$E_{\text{cor}} = \frac{\hbar i A}{2(2\pi)^3} \int d^2k \int d\omega \int_0^1 d\lambda \frac{\lambda \big(U_{ee}^0 \big)^2}{1 - \big(\Pi_e + \Pi_h \big) \lambda U_{ee}^0} \Big(\Pi_e + \Pi_h \Big)^2 \tag{3.57}$$

The λ integral is

$$\int_0^1 \frac{\lambda}{1-\lambda a} d\lambda = -\frac{\ln(1-a)+a}{a^2} \tag{3.58}$$

so

$$E_{\rm cor} = -\frac{\hbar i A}{2(2\pi)^3}\int d^2k \int d\omega \Big[\ln(1-\big(\Pi_e+\Pi_h\big)U^0_{ee}) + \big(\Pi_e+\Pi_h\big)U^0_{ee}\Big] \tag{3.59}$$

For $d \neq 0$, the electrons and holes reside in different regions of space, so they screen each other differently. In this case, we must solve the generalized equation

$$E_{\rm cor} = \frac{\hbar i A}{2(2\pi)^3}\int_0^1 \frac{d\lambda}{\lambda}\int d^2k \int d\omega \left[\begin{array}{cc} \Pi_e & \Pi_h \end{array}\right] \left[\begin{array}{cc} U^\lambda_{ee}\lambda U^0_{ee} & U^\lambda_{eh}\lambda U^0_{eh} \\ U^\lambda_{eh}\lambda U^0_{eh} & U^\lambda_{hh}\lambda U^0_{hh} \end{array}\right] \left[\begin{array}{c} \Pi_e \\ \Pi_h \end{array}\right] \tag{3.60}$$

where

$$U^0_{ij} = \begin{cases} \frac{2\pi e^2}{k} & i=j \\ -\frac{2\pi e^2}{k}\exp[-kd] & i\neq j \end{cases} \tag{3.61}$$

and U^λ_{ij} are the dynamically-screened effective interactions. Within the random-phase approximation, these are given by the following Dyson-like or Ornstein-Zernike-like equations [69]

$$U^\lambda_{ee} = \lambda U^0_{ee} + \lambda U^0_{ee}\Pi_e U^\lambda_{ee} + \lambda U^0_{eh}\Pi_h U^\lambda_{eh} \tag{3.62}$$

$$U^\lambda_{hh} = \lambda U^0_{hh} + \lambda U^0_{eh}\Pi_e U^\lambda_{eh} + \lambda U^0_{hh}\Pi_h U^\lambda_{hh} \tag{3.63}$$

$$U^\lambda_{eh} = \lambda U^0_{eh} + \lambda U^0_{ee}\Pi_e U^\lambda_{eh} + \lambda U^0_{eh}\Pi_h U^\lambda_{hh} \tag{3.64}$$

or in matrix form,

$$\left[\begin{array}{cc} U^\lambda_{ee} & U^\lambda_{eh} \\ U^\lambda_{eh} & U^\lambda_{hh} \end{array}\right] = \lambda \left[\begin{array}{cc} U^0_{ee} & U^0_{eh} \\ U^0_{eh} & U^0_{hh} \end{array}\right] + \lambda \left[\begin{array}{cc} \Pi_e U^0_{ee} & \Pi_h U^0_{eh} \\ \Pi_e U^0_{eh} & \Pi_h U^0_{hh} \end{array}\right] \left[\begin{array}{cc} U^\lambda_{ee} & U^\lambda_{eh} \\ U^\lambda_{eh} & U^\lambda_{hh} \end{array}\right] \tag{3.65}$$

We first factor out U^0_{ee} from Eq. (3.60) and use

$$\frac{U^0_{ii}}{U^0_{ee}} = 1 \qquad \frac{U^0_{ij}}{U^0_{ee}} = -\exp[-kd] \tag{3.66}$$

to obtain

$$\begin{aligned} E_{\rm cor} =& \frac{\hbar i A}{2(2\pi)^3}\int_0^1 \frac{d\lambda}{\lambda} U^0_{ee}\int d^2k \int d\omega \left[\begin{array}{cc} \Pi_e & \Pi_h \end{array}\right] \\ & \times \left[\begin{array}{cc} U_{ee} & -U_{eh}\exp[-kd] \\ -U_{eh}\exp[-kd] & U_{hh} \end{array}\right] \left[\begin{array}{c} \Pi_e \\ \Pi_h \end{array}\right] \end{aligned} \tag{3.67}$$

In Section 3.7, I derive this matrix of effective interactions in terms of the bare electron-electron interaction. Substitution of this result leads to

$$E_{\rm cor} = \frac{\hbar i A}{2(2\pi)^3}\int d^2k \int d\omega \int_0^1 \frac{d\lambda}{\lambda} \frac{(\lambda U^0_{ee})^2}{1-\lambda\big(\Pi_e+\Pi_h\big)U^0_{ee}+\lambda^2\big(1-\exp[-4kd]\big)\Pi_e\Pi_h\big(U^0_{ee}\big)^2} \tag{3.68}$$
$$\times \left[\begin{array}{cc} \Pi_e & \Pi_h \end{array}\right] \left[\begin{array}{cc} 1+\lambda\big(\exp[-4kd]-1\big)\Pi_h U^0_{ee} & \exp[-2kd] \\ \exp[-2kd] & 1+\lambda\big(\exp[-4kd]-1\big)\Pi_e U^0_{ee} \end{array}\right] \left[\begin{array}{c} \Pi_e \\ \Pi_h \end{array}\right]$$

If $d = 0$, we recover the usual result when the electron-electron and electron-hole interactions are equal.

$$E_{\rm cor} = \frac{\hbar i A}{2(2\pi)^3}\int d^2k \int d\omega \int_0^1 \frac{d\lambda}{\lambda} \frac{(\lambda U^0_{ee})^2}{1-\lambda\big(\Pi_e+\Pi_h\big)U^0_{ee}} \left[\begin{array}{cc} \Pi_e & \Pi_h \end{array}\right] \left[\begin{array}{cc} 1 & 1 \\ 1 & 1 \end{array}\right] \left[\begin{array}{c} \Pi_e \\ \Pi_h \end{array}\right] \tag{3.69}$$

$$= \frac{\hbar i A}{2(2\pi)^3}\int d^2k \int d\omega \int_0^1 \frac{d\lambda}{\lambda} \frac{(\lambda U^0_{ee})^2}{1-\lambda\big(\Pi_e+\Pi_h\big)U^0_{ee}} \Big(\Pi_e+\Pi_h\Big)^2 \tag{3.70}$$

In the other asymptotic limit ($d \to \infty$), the electrons and holes no longer interact with each other. From Eq. (3.68), we have

$$E_{\rm cor} = \frac{\hbar i A}{2(2\pi)^3}\int d^2k \int d\omega \int_0^1 \frac{d\lambda}{\lambda} \frac{(\lambda U^0_{ee})^2}{1-\lambda\big(\Pi_e+\Pi_h\big)U^0_{ee}+\lambda^2\Pi_e\Pi_h\big(U^0_{ee}\big)^2} \left[\begin{array}{cc} \Pi_e & \Pi_h \end{array}\right]$$
$$\times \left[\begin{array}{cc} 1-\lambda\Pi_h U^0_{ee} & 0 \\ 0 & 1-\lambda\Pi_e U^0_{ee} \end{array}\right] \left[\begin{array}{c} \Pi_e \\ \Pi_h \end{array}\right] \tag{3.71}$$

$$= \frac{\hbar i A}{2(2\pi)^3}\int d^2k \int d\omega \int_0^1 \frac{d\lambda}{\lambda} \frac{(\lambda U^0_{ee})^2}{(1-\lambda\Pi_e U^0_{ee})(1-\lambda\Pi_h U^0_{ee})} \left[\begin{array}{cc} \Pi_e & \Pi_h \end{array}\right]$$
$$\times \left[\begin{array}{cc} 1-\lambda\Pi_h U^0_{ee} & 0 \\ 0 & 1-\lambda\Pi_e U^0_{ee} \end{array}\right] \left[\begin{array}{c} \Pi_e \\ \Pi_h \end{array}\right] \tag{3.72}$$

$$= \frac{\hbar i A}{2(2\pi)^3}\int d^2k \int d\omega \int_0^1 \frac{d\lambda}{\lambda} \left[\begin{array}{cc} \Pi_e & \Pi_h \end{array}\right]$$
$$\times \left[\begin{array}{cc} (\lambda U^0_{ee})^2/(1-\lambda\Pi_e U^0_{ee}) & 0 \\ 0 & (\lambda U^0_{ee})^2/(1-\lambda\Pi_h U^0_{ee}) \end{array}\right] \left[\begin{array}{c} \Pi_e \\ \Pi_h \end{array}\right] \tag{3.73}$$

$$= \frac{\hbar i A}{2(2\pi)^3}\int d^2k \int d\omega \int_0^1 \frac{d\lambda}{\lambda} \Big\{ \frac{\big(\lambda\Pi_e U^0_{ee}\big)^2}{1-\lambda\Pi_e U^0_{ee}} + \frac{\big(\lambda\Pi_h U^0_{ee}\big)^2}{1-\lambda\Pi_h U^0_{ee}} \Big\} \tag{3.74}$$

This last equation is the correlation energy for two non-interacting electron and hole gases.

We now return to Eq. (3.68) and consider intermediate bilayer separations. To express this in Ry_{ex}, we scale lengths by a_{ex}, wavevectors by k_F, and frequencies by $\hbar^2 k_F^2/(2m_{red})$.

Using Eq. (3.40) and (3.30),

$$\frac{E_{\rm cor}}{N} = \frac{i}{\pi r_s^2}\int_0^\infty dk \int_0^\infty d\omega \int_0^1 d\lambda \frac{k\lambda\big(U_{ee}^0\big)^2}{1-\lambda\big(\Pi_e+\Pi_h\big)U_{ee}^0+\lambda^2\big(1-\exp[-4\sqrt{2}kd/r_s]\big)\Pi_e\Pi_h\big(U_{ee}^0\big)^2}$$
$$\times \left[\begin{array}{cc}\Pi_e & \Pi_h\end{array}\right]\left[\begin{array}{cc}1+\lambda\big(\exp[-4\sqrt{2}kd/r_s]-1\big)\Pi_h U_{ee}^0 & \exp[-2\sqrt{2}kd/r_s] \\ \exp[-2\sqrt{2}kd/r_s] & 1+\lambda\big(\exp[-4\sqrt{2}kd/r_s]-1\big)\Pi_e U_{ee}^0\end{array}\right]$$
$$\times \left[\begin{array}{c}\Pi_e \\ \Pi_h\end{array}\right] Ry_{ex} \tag{3.75}$$

The result of the matrix multiplication is

$$\begin{aligned}\frac{E_{\rm cor}}{N} =& \frac{i}{\pi r_s^2}\int_0^\infty dk \int_0^\infty d\omega \int_0^1 d\lambda k \frac{\lambda}{1-\lambda\big(\Pi_e+\Pi_h\big)U_{ee}^0+\lambda^2\big(1-\exp[-4\sqrt{2}kd/r_s]\big)\Pi_e\Pi_h\big(U_{ee}^0\big)^2} \\ &\times\Big(\big(U_{ee}^0\big)^2\big(\Pi_e^2+\Pi_h^2\big)+2\big(U_{ee}^0\big)^2\Pi_e\Pi_h\exp[-2\sqrt{2}kd/r_s] \\ &+\lambda\big(\exp[-4\sqrt{2}kd/r_s]-1\big)\big(U_{ee}^0\big)^3\big(\Pi_e+\Pi_h\big)\Pi_e\Pi_h\Big)Ry_{ex}\end{aligned} \tag{3.76}$$

The λ integral we need to solve for arbitrary d is

$$\int_0^1 \frac{\lambda}{1-a\lambda+b\lambda^2}\big(c+f\lambda\big)d\lambda \tag{3.77}$$

I outline how to compute it in Section 3.8.

3.3.3.1 Zeroth-order zero temperature polarizability in two dimensions

To solve for the correlation energy given by Eq. (3.76), we need the electron and hole polarizabilities. Stern was the first to calculate the two-dimensional lowest-order polarizability for the electron gas [77], and Kuramoto and Kamimura were the first to utilize these polarizabilities to study the two-dimensional EHL [78]. For a particle of type i, the real part is

$$\mathrm{Re}\Pi_i(k,\omega) = \frac{m_i}{\hbar^2\pi}\Big[-1-\frac{\omega-k^2}{2k^2}\sqrt{1-\big(\frac{2k}{\omega-k^2}\big)^2}+\frac{\omega+k^2}{2k^2}\sqrt{1-\big(\frac{2k}{\omega+k^2}\big)^2}\Big] \tag{3.78}$$

and the imaginary part is

$$\mathrm{Im}\Pi_i(k,\omega) = -\frac{m_i}{\hbar^2\pi k}\Big[\sqrt{1-\big(\frac{\omega-k^2}{2k}\big)^2}-\sqrt{1-\big(\frac{\omega+k^2}{2k}\big)^2}\Big] \tag{3.79}$$

In both cases, each square root must be set to zero when they acquire a negative argument.

Polarizabilities are always multiplied by a bare Coulomb interaction U^0. Using Eq. (3.40) and

$$m_{red} = \frac{m_e}{\sigma+1} \tag{3.80}$$

$$= \frac{\sigma m_h}{\sigma+1} \tag{3.81}$$

we have

$$U^0(k)\mathrm{Re}\Pi_e(k,\omega) = (\sigma+1)A(k,(\sigma+1)\omega,r_s) \tag{3.82}$$

$$U^0(k)\mathrm{Im}\Pi_e(k,\omega,) = (\sigma+1)\Sigma(k,(\sigma+1)\omega,r_s) \tag{3.83}$$

$$U^0(k)\mathrm{Re}\Pi_h(k,\omega) = \frac{(\sigma+1)}{\sigma}A(k,\frac{(\sigma+1)}{\sigma}\omega,r_s) \tag{3.84}$$

$$U^0(k)\mathrm{Im}\Pi_h(k,\omega) = \frac{(\sigma+1)}{\sigma}\Sigma(k,\frac{(\sigma+1)}{\sigma}\omega,r_s) \tag{3.85}$$

where

$$A(k,\omega,r_s) = \frac{\sqrt{2}r_s}{k}\Big[-1-\frac{\omega-k^2}{2k^2}\sqrt{1-\big(\frac{2k}{\omega-k^2}\big)^2}+\frac{\omega+k^2}{2k^2}\sqrt{1-\big(\frac{2k}{\omega+k^2}\big)^2}\Big] \tag{3.86}$$

and

$$\Sigma(k,\omega,r_s) = -\frac{\sqrt{2}r_s}{k^2}\Big[\sqrt{1-\big(\frac{\omega-k^2}{2k}\big)^2}-\sqrt{1-\big(\frac{\omega+k^2}{2k}\big)^2}\Big] \tag{3.87}$$

Figure 3.1 shows A and Σ as functions of q and ω.

As mentioned earlier, one may improve upon RPA calculations by including a "local field" correction which takes into account correlations between like particles [68]. In two dimensions [78], Hubbard's correction involves replacing the RPA polarizabilities with

$$A_{Hubbard} = \Big(1-\frac{k}{4(k+k_F)}\Big)A \tag{3.88}$$

$$\Sigma_{Hubbard} = \Big(1-\frac{k}{4(k+k_F)}\Big)\Sigma \tag{3.89}$$

3.4 Zero temperature results

We evaluate the double integral in Eq. (3.76) evaluated using Simpson's rule. Figure 3.2 shows the correlation energy using Hubbard's correction of a $\sigma = 1$ 2D EHL at $r_s = 0.5$ as a function of the integration step size $\Delta\omega$ for various Δq. The integrals are converged when the step sizes are both approximately 0.01. Figure 3.3 shows how the ω-integral varies with ω_{max} as a function of q (again using Hubbard's correction). While most of the integral lies

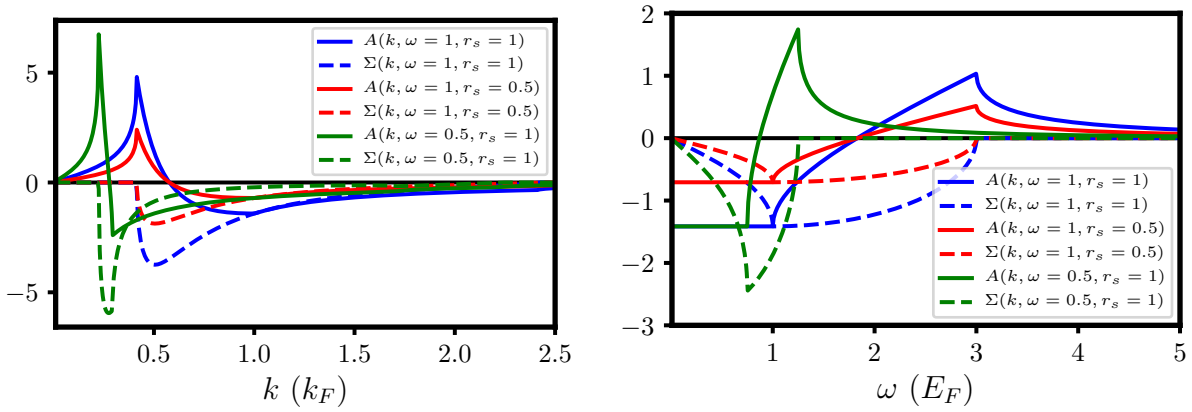

Figure 3.1: Plots of the real and imaginary parts of the 2D RPA polarizability multiplied by the Coulomb potential.

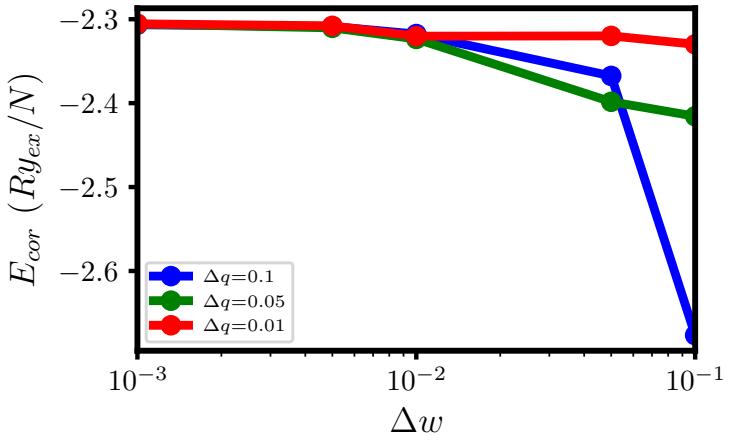

Figure 3.2: Correlation energy of a $\sigma = 1$ 2D EHL at $r_s = 0.5$ as a function of the integration step size $\Delta\omega$ for various Δq.

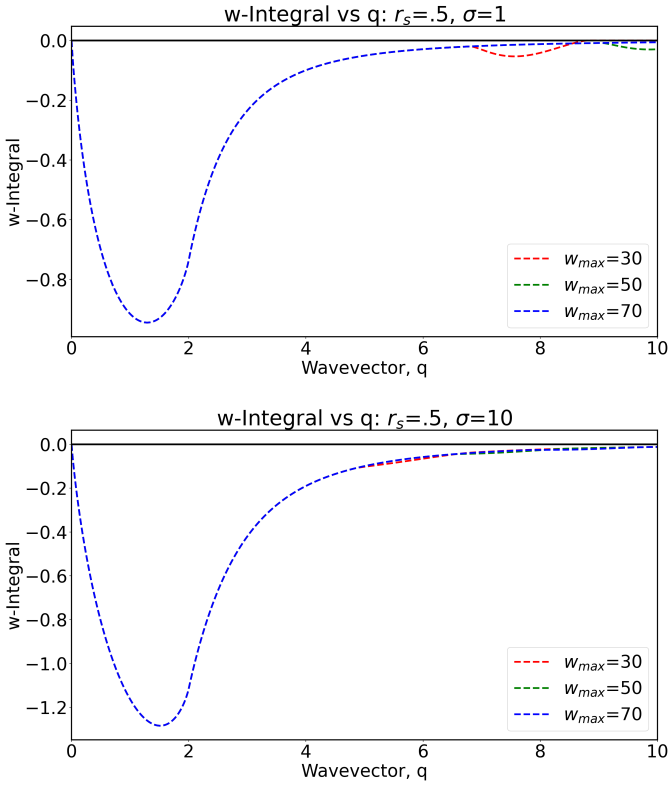

Figure 3.3: Correlation energy as a function of q_{max} for various ω_{max}.

within $q < 10$ and $\omega < 30$, we noticed that there can be significant contributions at larger q and ω, especially for $\sigma \neq 1$. We typically used $q_{max} = 30$, $\omega_{max} = 60$, $\Delta\omega = \Delta q = 0.01$, and $q_{min} = \omega_{min} = 0.01$.

The ground state energy (per particle) of the bilayer electron-hole liquid is given by the sum of the kinetic energy (Eq. (3.50)), exchange energy (Eq. (3.54)), correlation energy (Eq. (3.76)), and capacitor energy (Eq. (3.42)). Figure 3.4 shows these contributions as a function of the interparticle spacing r_s for $\sigma = 1$ and $d = 0$. Similar to the degenerate electron gas, the exchange and correlation energy stabilizes the condensed phase while the kinetic energy (and possibly the capacitor energy) destabilizes it.

Figure 3.5 shows the total energy per particle as a function of r_s for $d = 0$ and various electron-hole mass ratios σ. The total energy is minimized as σ decreases from unity, similar to how the biexciton energy decreases by lowering σ.

The total energy depends on the bilayer separation only through the correlation and capacitor terms. In Figure 3.6, we show their sum for various d. The energy increases as the electrons and holes are separated from each other due to two effects. Firstly, the electrons and holes cannot effectively screen one another as they reside in distinct planes. Secondly

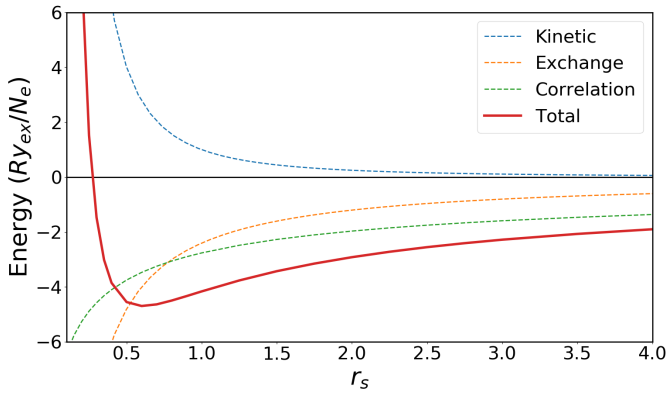

Figure 3.4: Contributions to the total energy for the 2D $\sigma = 1$ electron-hole liquid.

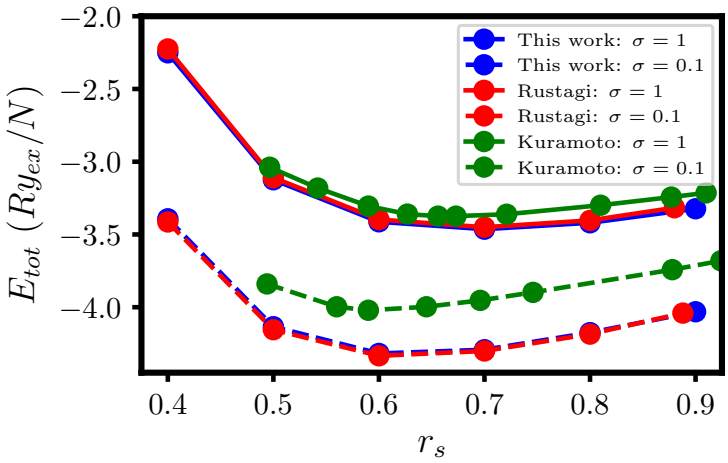

Figure 3.5: Total energy of 2D EHL as a function of interparticle spacing for $\sigma = 1$ and 0.1. "Rustagi" comes from [33] and "Kuramoto" comes from [78].

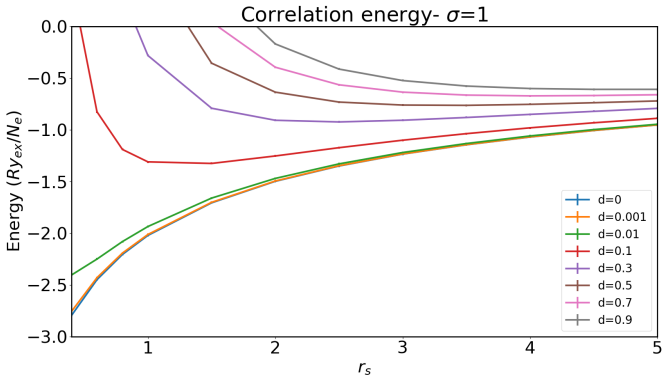

Figure 3.6: Correlation energy (including the $q = 0$ contribution) per particle as a function of interparticle spacing for $\sigma = 1$ and various d.

and more notably, there is an energetic cost for pulling apart two oppositely-charged planes; this is the capacitor term.

Figure 3.7 show the total energy versus $r_0 = r_s a_{ex}$ for various d. As expected, the equilibrium interparticle spacing (*i.e.*, the value of r_0 which minimizes the energy) increases as d increases. However, these values remain near unity for $0 \leq \frac{d}{a_{ex}} \leq 1.5$, so this condensed phase is clearly in the degenerate regime.

The minimum of the total energy is often defined as the binding energy for a carrier in the EHL. As d increases and the electrons and holes are separated, this binding energy decreases, as shown in the top panel of Figure 3.7. Interestingly, if we remove the capacitor's contribution, the $d \neq 0$ curves nearly match the $d = 0$ curve (see the bottom panel of Figure 3.7). While there is some d-dependence in the $q \neq 0$ correlation energy, it is almost negligible compare to the kinetic and exchange energies. Therefore, the classical mean-field capacitor term dictates how the ground state energy of the electron-hole liquid changes by separating the electrons from the holes.

As seen in Eq. (1.4) and (1.7), the length and energy scales (a_{ex} and Ry_{ex}) change with the electron-hole mass ratio. To compare systems with different σ on equal footing, we fix

$$m_e^* = m_0 \tag{3.90}$$

so

$$Ry_{ex}^{\sigma} = \frac{1}{\sigma + 1} Ry_{ex}^{\sigma=0} \tag{3.91}$$

and

$$a_{ex}^{\sigma} = (\sigma + 1) a_{ex}^{\sigma=0} \tag{3.92}$$

Figure 3.8 shows the binding energy of various exciton phases as function of bilayer separation. As before, the binding energy of an EHL is just the minimum of the total energy

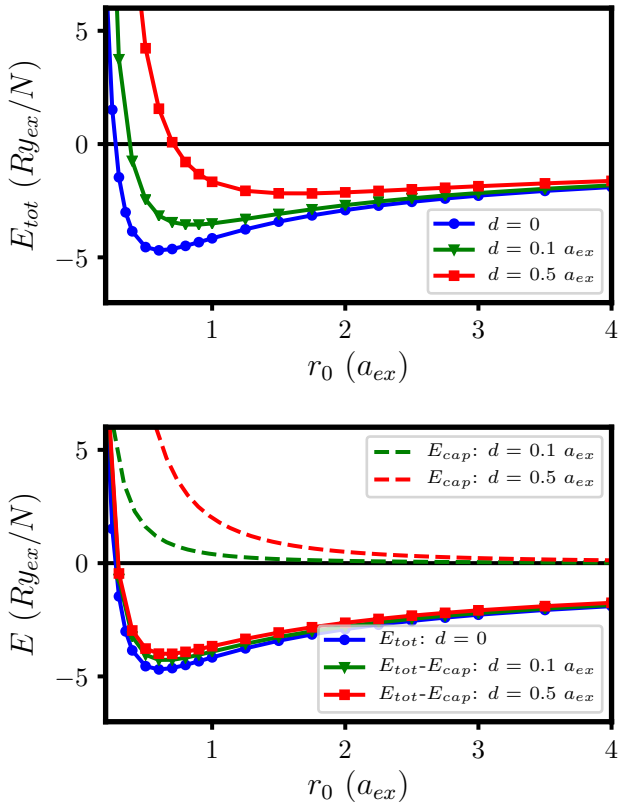

Figure 3.7: Total energy of EHL for various d. In the second figure, we remove the contribution from the capacitor term.

consisting of kinetic, exchange, correlation, and capacitor contributions. Here, we define the binding energy of a gas of excitons as their ground state energy plus a capacitor contribution to include their interactions at the mean-field level. To compare the stability of these phases at the same high densities, we evaluate the capacitor energy at the same equilibrium interparticle spacing. The binding energy of a gas of biexcitons is defined similarly. The energy difference between the $\sigma = 0.1$ EHL and an exciton gas for $d = 1.5a_{ex}$ is about 1 Ry_{ex}, which is approximately the same value as the photoluminescence red-shift Bar-Joseph and co-workers observed [42,43]. Motivated by this close agreement, we now turn to our finite temperature calculations.

3.5 Finite temperature theory

To study the electron-hole liquid at finite temperatures, we follow most of the same steps as in the zero temperature case with some key differences. Instead of working in the mi-

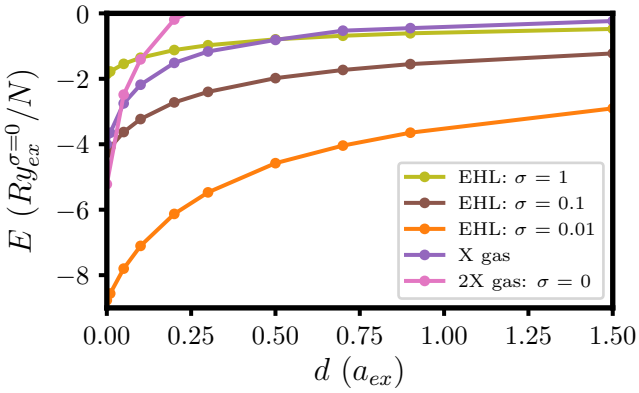

Figure 3.8: Electron-hole liquid binding energies as a function of bilayer separation.

crocanonical ensemble, it is convenient to now work in the grand canonical ensemble. We first calculate the chemical potential for non-interacting fermions starting from the grand canonical partition function. Next, we evaluate the exchange contribution to the thermodynamic potential as well as the Helmholtz free energy. Finally, using the linked cluster expansion [33,72], we incorporate correlation effects by summing the same "ring diagrams" as in the zero temperature case. However, in order to access finite temperatures, we sum over discrete Matsubara frequencies rather than integrate over the previously continuous frequencies. The $q = 0$ contribution to the correlation free energy– the capacitor term– is independent of temperature.

3.5.1 Ideal chemical potential

In the grand canonical ensemble, the partition function for N non-interacting particles is

$$\Xi = \sum_{n_1,n_2,\ldots,n_k,\ldots} \exp\Big[-\beta \sum_k (\varepsilon_k - \mu) n_k\Big] \tag{3.93}$$

where n_k are occupation numbers and $\varepsilon_{i,k}$ are the single-particle energies given in Eq. (3.10). For non-interacting fermions, the exponential factorizes, so we get

$$\Xi = \prod_k \Big\{ \sum_{n_k=0}^{1} \exp\Big[-\beta(\epsilon_k - \mu) n_k\Big]\Big\} \tag{3.94}$$

$$= \prod_k \Big\{1 + \exp\Big[-\beta(\epsilon_k - \mu)\Big]\Big\} \tag{3.95}$$

The total number of particles is calculated using

$$\langle N\rangle = \frac{\partial \ln \Xi}{\partial(\beta\mu)} \tag{3.96}$$

$$= \sum_k \frac{\exp[\beta(\mu-\varepsilon_k)]}{1+\exp[\beta(\mu-\varepsilon_k)]} \tag{3.97}$$

$$= \sum_k f(k,\beta,\mu) \tag{3.98}$$

where f is the Fermi-Dirac distribution given by Eq. (3.32). For particle i with ν_i bands and ξ_i spin degeneracies, we have

$$\langle N_i\rangle = \nu_i\xi_i \sum_k f_i(k,\beta,\mu) \tag{3.99}$$

Previously, we've used Eq. (3.98) to relate the Fermi wavevector k_F to the density by taking $\beta\to\infty$. Here, we evaluate it for general β. After writing the sum over wavevectors as an integral using Eq. (3.34), we have

$$\langle N_i\rangle = \frac{\nu_i\xi_i A}{(2\pi)^2}\int d^2k \frac{\exp[\beta(\mu-\varepsilon_{i,k})]}{1+\exp[\beta(\mu-\varepsilon_{i,k})]} \tag{3.100}$$

$$= \frac{\nu_i\xi_i A}{2\pi}\int_0^\infty \frac{\exp[\beta(\mu-\varepsilon_{i,k})]}{1+\exp[\beta(\mu-\varepsilon_{i,k})]} k dk \tag{3.101}$$

We now use a u-substitution: $u = \exp[\beta(\mu-\varepsilon_{i,k})]$.

$$\langle N_i\rangle = \frac{\nu_i\xi_i A}{2\pi}\frac{m_i}{\hbar^2\beta}\int_0^{\exp[\beta\mu]} \frac{1}{1+y} dy \tag{3.102}$$

$$= \frac{\nu_i\xi_i A}{\lambda_i^2}\ln\left(1+\exp[\beta\mu]\right) \tag{3.103}$$

where we have the thermal de Broglie wavelength

$$\lambda_i^2 = \frac{2\pi\hbar^2\beta}{m_i} \tag{3.104}$$

After some algebra, we obtain the chemical potential for N non-interacting particles of type i:

$$\beta\mu_0^i = \ln\left(\exp[n\lambda_i^2/(\nu_i\xi_i)]-1\right) \qquad \text{fermions} \tag{3.105}$$

The classical, non-degenerate limit is recovered when $n\lambda_i^2 \ll 1$; this occurs at high temperatures or low densities. By Taylor expanding the exponential, we get the chemical potential for a classical gas:

$$\beta\mu_0^i =_{n\lambda_i^2\ll 1} \ln(n\lambda_i^2/(\nu_i\xi_i)) \tag{3.106}$$

In the opposite highly degenerate regime ($n\lambda_i^2 \gg 1$), we have

$$\beta\mu_0^i =_{n\lambda_i^2\gg 1} \frac{n\lambda_i^2}{\nu_i\xi_i} \tag{3.107}$$

$$\mu_0^i =_{n\lambda_i^2\gg 1} \frac{n2\pi\hbar^2}{\nu_i\xi_i m_i} \tag{3.108}$$

The chemical potential for ideal fermions becomes independent of temperature and proportional to density.

For bosons, the grand partition function given by Eq. (3.93) becomes

$$\Xi = \prod_k \Big(1 - \exp[\beta(\mu - \varepsilon_k)]\Big)^{-1} \tag{3.109}$$

Following the same steps as above, we get

$$\langle N_i\rangle = \nu_i\xi_i \sum_k \frac{\exp[\beta(\mu-\varepsilon_{i,k})]}{1-\exp[\beta(\mu-\varepsilon_{i,k})]} \tag{3.110}$$

$$= \frac{\nu_i\xi_i A}{2\pi}\frac{m_i}{\hbar^2\beta}\int_0^{\exp[\beta\mu]} \frac{1}{1-y}dy \tag{3.111}$$

$$= -\frac{\nu_i\xi_i A}{\lambda_i^2}\ln\big(1-\exp[\beta\mu]\big) \tag{3.112}$$

Hence, the chemical potential for bosons is

$$\beta\mu_0^i = \ln\big(1-\exp[-n_i\lambda_i^2/(\nu_i\xi_i)]\big) \qquad \text{bosons} \tag{3.113}$$

3.5.2 Exchange free energy

The first-order exchange contribution to the thermodynamic potential is a generalization of Eq. (3.51):

$$\Omega_{exch}(\beta,\mu) = -\sum_{i=e,h}\frac{\nu_i\xi_i}{2A}\sum_{\mathbf{k},\mathbf{p}}\frac{2\pi e^2}{4\pi\epsilon_0\epsilon|\mathbf{k}-\mathbf{p}|}f_i(k,\beta,\mu)f_i(p,\beta,\mu) \tag{3.114}$$

where f_i is the Fermi-Dirac distribution for particle i, given in Eq. (3.32). This equation is exact when we use the chemical potential for the interacting system, μ. Following previous work [33,76], we replace this exact chemical potential by the one corresponding to the non-interacting system, Eq. (3.105). Perrot and Dharma-Wardana have evaluated the higher-order corrections to this approximation [86]. Because we now write Eq. (3.115) in terms of densities, it becomes a Helmholtz free energy:

$$F_{exch}(\beta,n) = -\sum_{i=e,h}\frac{\nu_i\xi_i}{2A}\sum_{\mathbf{k},\mathbf{p}}\frac{2\pi e^2}{4\pi\epsilon_0\epsilon|\mathbf{k}-\mathbf{p}|}f_i\big(k,\beta,\mu_0(n)\big)f_i\big(p,\beta,\mu_0(n)\big) \tag{3.115}$$

We now introduce dimensionless quantities. Let $k' = k/k_F$ and $t = T/T_F$, where the Fermi temperature is

$$T_F = \frac{\hbar^2 k_F^2}{2m_{red}k_B} \tag{3.116}$$

The ideal chemical potentials become

$$\beta\mu_0^i = \begin{cases} \ln\left[\exp\left(\frac{1}{t(\sigma+1)}\right) - 1\right] & i = e \\ \ln\left[\exp\left(\frac{\sigma}{t(\sigma+1)}\right) - 1\right] & i = h \end{cases} \tag{3.117}$$

and the Fermi-Dirac distributions become

$$f_i(k', t, n) = \begin{cases} \frac{\exp\left[1/\left(t(\sigma+1)\right)\right]-1}{\exp\left[k'^2/\left(t(\sigma+1)\right)\right]+\exp\left[1/\left(t(\sigma+1)\right)\right]-1} & i = e \\ \frac{\exp\left[\sigma/\left(t(\sigma+1)\right)\right]-1}{\exp\left[k'^2\sigma/\left(t(\sigma+1)\right)\right]+\exp\left[\sigma/\left(t(\sigma+1)\right)\right]-1} & i = h \end{cases} \tag{3.118}$$

Note that when the electrons and holes have different masses, they feel two different effective temperatures:

$$t_i = \begin{cases} t(\sigma+1) & i = e \\ t(\sigma+1)/\sigma & i = h \end{cases} \tag{3.119}$$

In these reduced units, the density dependence enters only through the reduced temperature.

We now set $\nu_e = \nu_h = 1$ and $\xi_e = \xi_h = 2$. Dividing by N and converting the sums in Eq. (3.115) to integrals using Eq. (3.34), we get

$$\frac{F_{exch}(t)}{N} = -\sum_{i=e,h} \frac{k_F e^2}{(2\pi)^2} \int d^2k' \int d^2p' \frac{f_i(k', t) f_i(p', t)}{4\pi\epsilon_0\epsilon|\mathbf{k}' - \mathbf{p}'|} \tag{3.120}$$

In [76], Phatisena and co-workers write the exchange free energy of a two-dimensional electron gas (2DEG) relative to its exchange energy at zero temperature, E_X, given by eq. (3.54).

$$\frac{F_{exch}^{2DEG}(t)}{E_X} = 3\int_0^\infty dx x^2 f(x, t) \int_0^1 dz f(xz, t) K(z) \tag{3.121}$$

$$= C(t) \tag{3.122}$$

where $K(z)$ is the complete elliptic integral of the first kind. To apply this result for our two-component system, we evaluate it at the previously defined effective temperatures:

$$\frac{F_{exch}(t)}{N} = -\sum_{i=e,h} \frac{1.2004}{r_s} C(t_i) Ry_{ex} \tag{3.123}$$

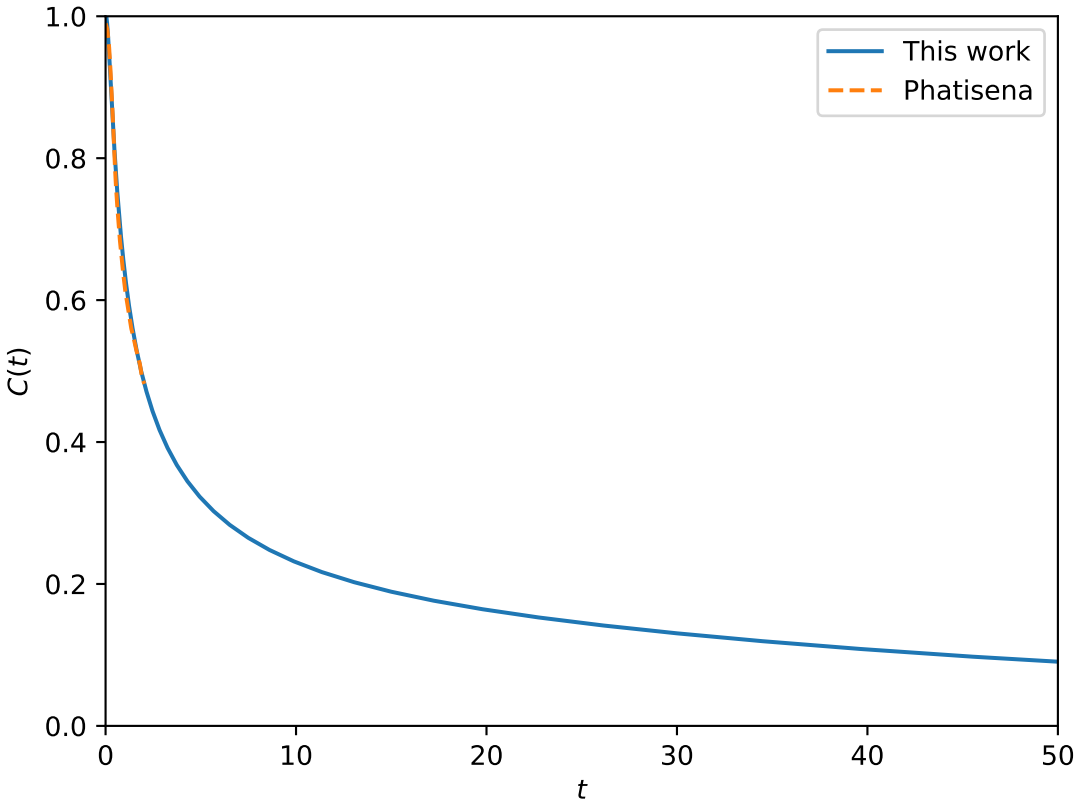

Figure 3.9: Temperature-dependent correction to the exchange energy of a two-dimensional electron gas.

We computed the double integral in Eq. (3.121) using Simpson's rule. Our integration parameters were as follows: $x_{min} = 0$, x_{max} =2 for $t < 0.1$ and x_{max} =10 for $t > 0.1$, Δx=0.05, $y_{min} = 0$, $y_{max} = 1 - 10^{-16}$, and $\Delta y = 0.001$. Figure 3.9 shows $C(t)$, the temperature-dependent correction to the exchange energy of a two-dimensional electron gas. As one should expect, the exchange free energy decreases as we move to the classical regime of high temperatures.

3.5.3 Correlation free energy

Using the linked-cluster expansion [33], the correlation thermodynamic potential for a bilayer electron-hole liquid is the finite temperature generalization of Eq. (3.60):

$$\Omega_{cor}(\beta,\mu) = -\frac{1}{2\beta}\sum_{\omega_l,k}\int_0^1 \frac{d\lambda}{\lambda}\left[\begin{array}{cc}\Pi_e & \Pi_h\end{array}\right]\left[\begin{array}{cc} U_{ee}(\lambda,k)U^0_{ee}(\lambda,k) & U_{eh}(\lambda,k)U^0_{eh}(\lambda,k) \\ U_{eh}(\lambda,k)U^0_{eh}(\lambda,k) & U_{hh}(\lambda,k)U^0_{hh}(\lambda,k)\end{array}\right] \times \left[\begin{array}{c}\Pi_e(k,\omega_l,\beta)\\ \Pi_h(k,\omega_l,\beta)\end{array}\right] \tag{3.124}$$

$$= -\frac{A}{2\beta(2\pi)^2}\sum_{\omega_l}\int d^2k\int_0^1 d\lambda U^0_{ee}\frac{\lambda U^0_{ee}}{1-\lambda\big(\Pi_e+\Pi_h\big)U^0_{ee}+\lambda^2\big(1-\exp[-4kd]\big)\Pi_e\Pi_h\big(U^0_{ee}\big)^2} \times\left[\begin{array}{cc}\Pi_e & \Pi_h\end{array}\right]\left[\begin{array}{cc}1+\lambda\big(\exp[-4kd]-1\big)\Pi_h U^0_{ee} & \exp[-2kd]\\ \exp[-2kd] & 1+\lambda\big(\exp[-4kd]-1\big)\Pi_e U^0_{ee}\end{array}\right]\left[\begin{array}{c}\Pi_e\\ \Pi_h\end{array}\right] \tag{3.125}$$

In lieu of integrating over a continuous frequency, we now must sum over discrete bosonic Matsubara frequencies

$$\omega_l = \frac{2\pi l}{\beta} \quad l = 0, \pm1, \pm2, ... \tag{3.126}$$

Using the same dimensionless quantities as before and Eq. (3.40), we obtain the correlation free energy per particle:

$$\frac{F_{cor}(t,r_s)}{N} = -\frac{t}{r_s^2}\sum_{\omega_l}\int_0^\infty dk\int_0^1 d\lambda \times\Big\{\frac{k\lambda}{1-\lambda\big(\Pi_e+\Pi_h\big)U^0_{ee}+\lambda^2\big(1-\exp[-4\sqrt{2}kd'/r_s]\big)\Pi_e\Pi_h\big(U^0_{ee}\big)^2} \times\Big(\big(U^0_{ee}\big)^2\big(\Pi_e^2+\Pi_h^2\big)+2\big(U^0_{ee}\big)^2\Pi_e\Pi_h\exp[-2\sqrt{2}kd'/r_s] +\lambda\big(\exp[-4\sqrt{2}kd'/r_s]-1\big)\big(U^0_{ee}\big)^3\big(\Pi_e+\Pi_h\big)\Pi_e\Pi_h\Big)\Big\}Ry_{ex} \tag{3.127}$$

The polarizabilities are even functions of ω_l, so we sum over $l = 0, 1, 2, ...$ and multiply the $l \neq 0$ terms by two. This is the same λ integral as in the zero-temperature case; it is evaluated in Section 3.8. The k-integral was evaluated using Simpson's rule and the same integration parameters as in the zero-temperature case.

Figure 3.10 shows the contribution of each Matsubara frequency to the correlation energy of a $\sigma = 1$ $d = 0$ electron-hole liquid at two different reduced temperatures t. As noted in [76], for $t > 10$, the frequency sum converges rapidly and we only need to sum over the first 21 frequencies. In contrast, the convergence is very slow for $t \approx 0.1$, so we include the first 301 frequencies.

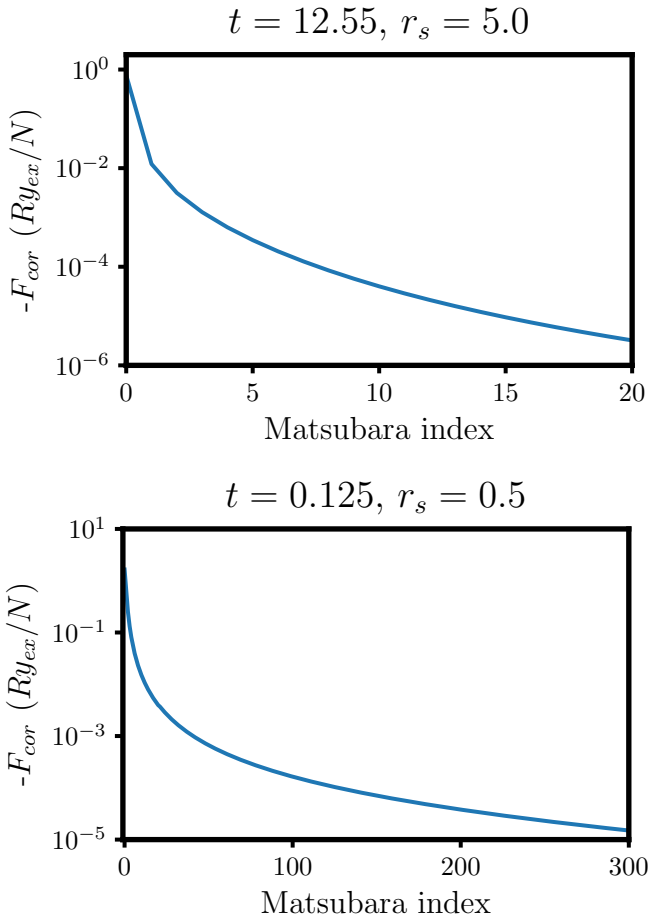

Figure 3.10: Contribution of each Matsubara frequency to the correlation energy of a $d = 0$, $\sigma = 1$ electron-hole liquid.

3.5.3.1 Zeroth-order finite temperature polarizability in two dimensions

The finite-temperature lowest-order polarizability in two dimensions for particle j is

$$\Pi_j(k, \omega_l, \beta) = -2 \int \frac{d^2p}{(2\pi)^2} \frac{f_j(\mathbf{p}+\mathbf{k}, \beta, \mu) - f_j(p, \beta, \mu)}{i\hbar\omega_l - \left(\frac{\hbar^2|\mathbf{p}+\mathbf{k}|^2}{2m_j} - \frac{\hbar^2 p^2}{2m_j}\right)} \tag{3.128}$$

We replace the true chemical potential by one corresponding to an ideal system, divide all wavevectors by k_F, and divide all temperatures by the same Fermi temperature as before. After dividing by the Fermi energy present in the denominator, Eq. (3.128) becomes

$$\Pi_j(k, \omega_l, t) = -\frac{m_r}{\pi^2\hbar^2} \int d^2p \frac{f_j(\mathbf{p}+\mathbf{k}, t) - f_j(p, t)}{i2\pi lt - \frac{m_r}{m_j}\left(|\mathbf{p}+\mathbf{k}|^2 - p^2\right)} \tag{3.129}$$

or

$$\Pi_j(k,\omega_l,t) = -\frac{m_j}{\pi^2\hbar^2}\int d^2p \frac{f_j(\mathbf{p}+\mathbf{k},t) - f_j(p,t)}{i2\pi l t_j - \left(|\mathbf{p}+\mathbf{k}|^2 - p^2\right)} \tag{3.130}$$

The Fermi-Dirac distributions are given in Eq. (3.118); their reduced temperature is the same t_j as in the denominator.

After evaluating the angular integral, the static ($l = 0$) and dynamic ($l \neq 0$) polarizabilities can be simplified as [76]

$$\Pi_j(k, l=0, t) = -\frac{4m_j}{\pi\hbar^2 k}\int_0^{k/2} dx \frac{x f(x,t_j)}{\sqrt{k^2-4x^2}} \tag{3.131}$$

and

$$\Pi_j(k, l\neq 0, t) = -\frac{4m_j}{\pi\hbar^2}\int_0^{\infty} dx \frac{x f_j(x,t)\cos\phi}{\left[\left(k^4 - 4x^2k^2 - 4l^2\pi^2t_j^2\right)^2 + 16l^2\pi^2t_j^2k^4\right]^{1/4}} \tag{3.132}$$

where

$$\tan(2\phi) = \frac{4k^2 l\pi t_j}{k^4 - 4x^2k^2 - 4l^2\pi^2t_j^2} \tag{3.133}$$

When computing ϕ, we must use "atan2(y,x)," the two-argument arctangent function which yields the angle between the positive x-axis and the point (x,y). Both integrals were computed using Simpson's rule. For the static case, we used $x_{min} = 0$, $x_{max} = k/2 - 10^{-8}$, and $\Delta x = 3\times 10^{-5}$. For the dynamic case, we used $x_{min} = 0$, $x_{max} = 5$ for $t < 0.01$ and $x_{max} = 30$ for $t > 0.01$, and $\Delta x = 0.1$. Some finite-temperature polarizabilities are shown in Figures 3.11 and 3.12. To directly compare with the results of Phatisena *et al.* [76], we set $\hbar = 1$ and $m_j = 0.5$ for plotting purposes.

We computed these polarizabilities for $k = 0.01, 0.02, ..., 30$ and $l = 0, 1, ..., 300$. For $l < 20$, the polarizabilities depend strongly on t, so we computed them for 100 values of t following a geometric progression starting from 10^{-4} and with a common ratio of 1.26. For larger l, we used 25 values of t following a geometric progression starting from 10^{-4} and with a common ratio of 1.83. We then linearly interpolated each polarizability across t at each wavevector k.

3.6 Finite temperature results

In the previous section, we evaluated contributions to the free energy per particle, F. The corresponding chemical potentials are

$$\mu = F + \left(\frac{\partial F}{\partial n}\right)_{T,A} n \tag{3.134}$$

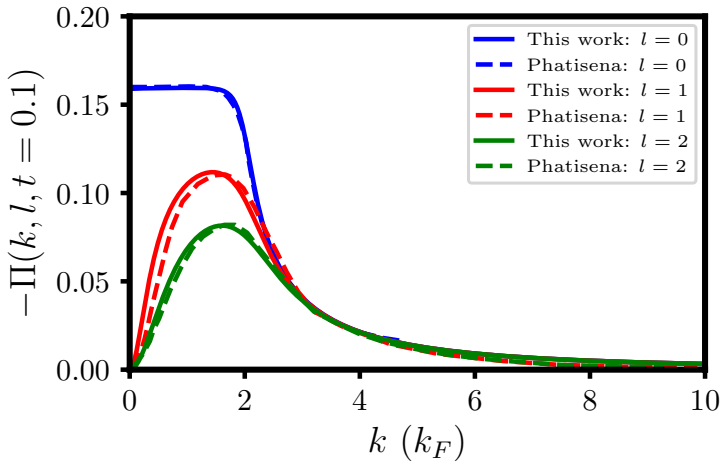

Figure 3.11: Static and dynamic polarizabilities as functions of k. "Phatisena" comes from [76].

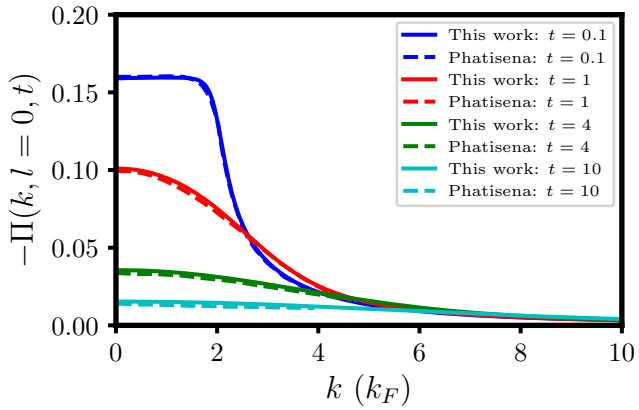

Figure 3.12: Static polarizability as a function of k for various reduced temperatures t. "Phatisena" comes from [76].

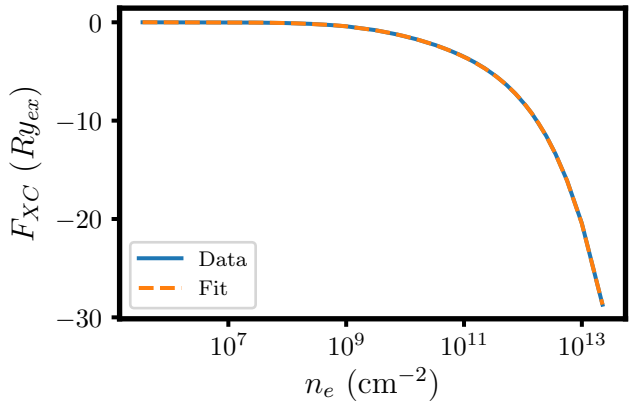

Figure 3.13: Exchange-correlation free energy as a function of free carrier density. The exact values as well as the fit given by Eq. (3.136) are shown.

The capacitor's contribution can be computed exactly:

$$\mu_{cap} = \frac{8d'}{r_s^2} Ry_{ex} \tag{3.135}$$

where $d' = d/a_{ex}$. In order to obtain smooth exchange and correlation chemical potentials, we first fit these free energies to the function

$$F_{fit}(n; n_C) = \begin{cases} \sum_{j=0}^{N} a_j n^{j/2} & n < n_C \\ \sum_{j=N+1}^{2N+2} a_j (\ln n)^{j-N-1} & n \geq n_C \end{cases} \tag{3.136}$$

n_C is the density threshold where we change the functional form. (We typically used 10^9 cm^{-2}.) The low-density classical regime is described by Debye-Hückel theory; in two dimensions the free energy is proportional to $\sqrt{n}$. The fit in the high-density regime is inspired by density functional theory exchange-correlation functionals within the local-density approximation. The fit is shown in Figure 3.13, and the derivation and numerical implementation is provided in Section 3.9.

Figure 3.14 shows the total chemical potential μ_{tot} for a $\sigma = 1$, $d = 0$ electron-hole liquid as a function of the free carrier density. At low densities, the exchange-correlation contribution is zero, and the ideal contribution can be described classically by Eq. (3.106). Between 10^9 and 10^{11} cm^{-2}, the non-ideal exchange-correlation piece dominates, causing μ_{tot} to decrease. Here, the thermodynamic stability criterion

$$\left(\frac{\partial \mu}{\partial n}\right)_{T,A} > 0 \tag{3.137}$$

is not met [79]. To resolve this, the system phase separates into low and high densities regions in order to stabilize. In Chapter 4, we will correct this and map the liquid-gas phase diagrams by Maxwell equal-area constructions.

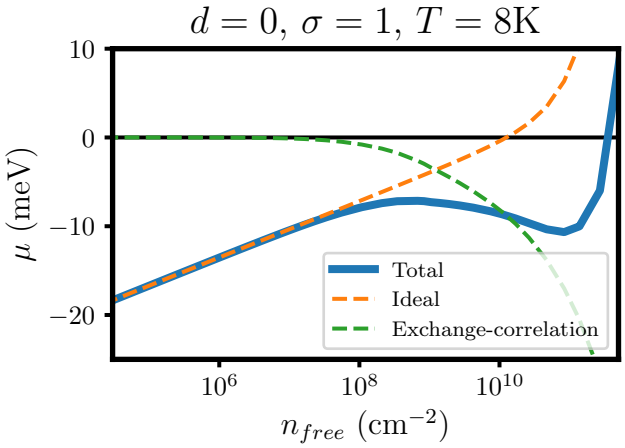

Figure 3.14: Chemical potential for a $\sigma = 1$, $d = 0$ electron-hole liquid at 8 K. The ideal and non-ideal contributions are separated.

The temperature dependence of the total chemical potential is shown in Figure 3.15. The linear behavior (on the log-x scale) at low densities can be described classically by Eq. (3.106); here, the chemical potential is proportional to temperature. At high densities, all three systems experience pressure due to quantum degeneracy; the chemical potentials become independent of temperature and proportional to density, as seen in Eq. (3.108). Finally, we note that the chemical potential is a monotonically non-decreasing function for $T = 16$ K; this is approximately the critical temperature for the liquid-gas transition of free electrons and holes.

In Figure 3.16, we compare the total chemical potential for a $\sigma = 0.1$ EHL at T=14 K for three different bilayer separations. Similar to the zero-temperature case, the d-dependence of the total chemical potential only enters through the correlation and capacitor terms. Since these pieces are only relevant at high densities, all three μ_{tot} are equal at low densities. Additionally, if we remove the capacitor's contribution, the chemical potentials are strikingly similar; the $d = 0$ case is slightly different because the electrons and holes reside in the same plane and can effectively screen one another.

As discussed earlier with the zero-temperature results, the energy scale (Ry_{ex}) increases and the length scale (a_{ex}) decreases as the electron-hole mass ratio deviates from unity. Thus, for smaller $\sigma < 1$, the exchange-correlation contributions are magnified and influence μ_{tot} at slightly lower densities. This is reflected in Figure 3.17, which shows chemical potentials for a $d = 0$ EHL at $T = 8$ K for σ =1, 0.1, and 0.01.

In this Chapter, we studied the energetics of Keldysh's electron-hole liquid in a bilayer geometry using a field-theoretic (*i.e.*, Green's-function) approach. First considering zero temperatures, we calculated the binding energy of this condensed state and compared it to the energy of a gas of indirect excitons. For the same bilayer separation and electron-hole

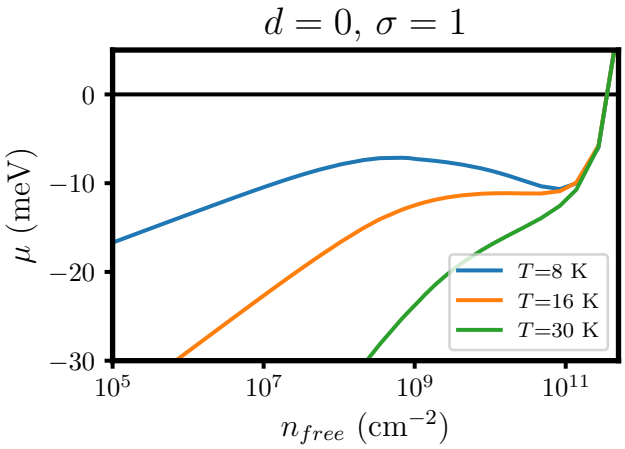

Figure 3.15: Chemical potentials for a $\sigma = 1$, $d = 0$ electron-hole liquid at three different temperatures.

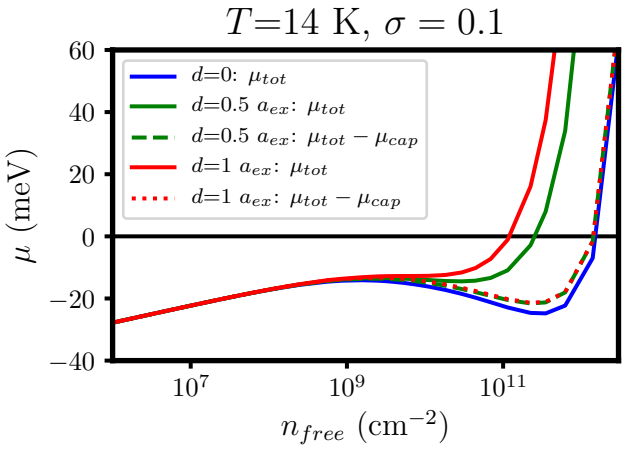

Figure 3.16: Chemical potentials for a $\sigma = 0.1$ electron-hole liquid at T=14 K and d=0, 0.5, and 1 a_{ex}. The capacitor contributions are removed for $d \neq 0$.

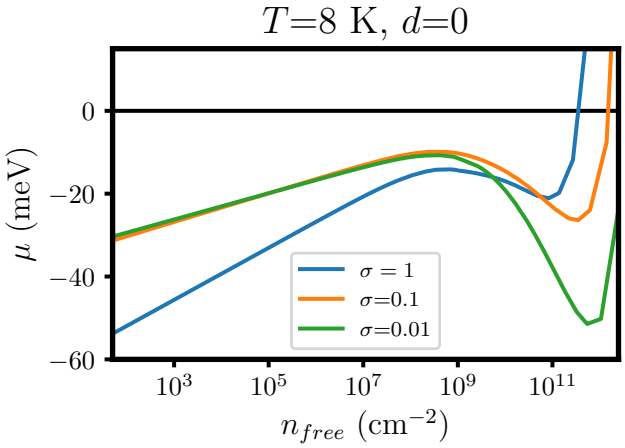

Figure 3.17: Chemical potentials for a $d = 0$ electron-hole liquid at T=8 K for three different mass ratios.

mass ratio as in Bar-Joseph experiments, we find the energy difference between the quantum EHL and IX gas to be approximately equal to the photoluminescence red-shift they measured. Next, we evaluated free energies and chemical potentials. As shown in Figures 3.14-3.17, if the temperature is below some critical value, the chemical potential violates the stability criterion Eq. (3.137), over a certain range of densities. In Chapter 4, we will map the phase diagram using Maxwell equal-area constructions. Additionally, we will check the validity of neglecting bound indirect excitons.

3.7 Appendix: deriving effective Coulomb interactions for the bilayer geometry

The equation we need to solve is

$$\begin{bmatrix} U_{ee} & -U_{eh}\exp[-kd] \\ -U_{eh}\exp[-kd] & U_{hh} \end{bmatrix} = \begin{bmatrix} U^0_{ee} & -U^0_{eh}\exp[-kd] \\ -U^0_{eh}\exp[-kd] & U^0_{hh} \end{bmatrix} \tag{3.138}$$

$$+ \begin{bmatrix} \Pi_e U^0_{ee} & -\Pi_h U^0_{eh}\exp[-kd] \\ -\Pi_e U^0_{eh}\exp[-kd] & \Pi_h U^0_{hh} \end{bmatrix} \begin{bmatrix} U_{ee} & -U_{eh}\exp[-kd] \\ -U_{eh}\exp[-kd] & U_{hh} \end{bmatrix}$$

$$\begin{bmatrix} 1-\Pi_e U^0_{ee} & \Pi_h U^0_{eh}\exp[-kd] \\ \Pi_e U^0_{eh}\exp[-kd] & 1-\Pi_h U^0_{hh} \end{bmatrix} \begin{bmatrix} U_{ee} & -U_{eh}\exp[-kd] \\ -U_{eh}\exp[-kd] & U_{hh} \end{bmatrix}$$

$$= \begin{bmatrix} U^0_{ee} & -U^0_{eh}\exp[-kd] \\ -U^0_{eh}\exp[-kd] & U^0_{hh} \end{bmatrix} \tag{3.139}$$

We invert the leftmost matrix to get

$$\begin{aligned}
&\begin{bmatrix} U_{ee} & -U_{eh}\exp[-kd] \\ -U_{eh}\exp[-kd] & U_{hh} \end{bmatrix} \\
&= \Big\{\big(1-\Pi_e U^0_{ee}\big)\big(1-\Pi_h U^0_{hh}\big) - \Pi_e\Pi_h\big(U^0_{eh}\big)^2\exp[-2kd]\Big\}^{-1} \\
&\times \begin{bmatrix} 1-\Pi_h U^0_{hh} & -\Pi_h U^0_{eh}\exp[-kd] \\ -\Pi_e U^0_{eh}\exp[-kd] & 1-\Pi_e U^0_{ee} \end{bmatrix} \begin{bmatrix} U^0_{ee} & -U^0_{eh}\exp[-kd] \\ -U^0_{eh}\exp[-kd] & U^0_{hh} \end{bmatrix}
\end{aligned} \tag{3.140}$$

We then factor out U^0_{ee} from the rightmost matrix.

$$\begin{bmatrix} U_{ee} & -U_{eh}\exp[-kd] \\ -U_{eh}\exp[-kd] & U_{hh} \end{bmatrix} = \frac{U^0_{ee}}{\big(1-\Pi_e U^0_{ee}\big)\big(1-\Pi_h U^0_{hh}\big) - \Pi_e\Pi_h\big(U^0_{eh}\big)^2\exp[-2kd]} \tag{3.141}$$

$$\begin{aligned}
&\times \begin{bmatrix} 1-\Pi_h U^0_{hh} & -\Pi_h U^0_{eh}\exp[-kd] \\ -\Pi_e U^0_{eh}\exp[-kd] & 1-\Pi_e U^0_{ee} \end{bmatrix} \begin{bmatrix} 1 & \exp[-2kd] \\ \exp[-2kd] & 1 \end{bmatrix} \\
&= \frac{U^0_{ee}}{\big(1-\Pi_e U^0_{ee}\big)\big(1-\Pi_h U^0_{hh}\big) - \Pi_e\Pi_h\big(U^0_{eh}\big)^2\exp[-2kd]} \\
&\times \begin{bmatrix} A & B \\ C & D \end{bmatrix}
\end{aligned}$$

where

$$A = 1-\Pi_h U^0_{hh} - \Pi_h U^0_{eh}\exp[-3kd] \tag{3.142}$$

$$B = \exp[-2kd] - \Pi_h U^0_{hh}\exp[-2kd] - \Pi_h U^0_{eh}\exp[-kd] \tag{3.143}$$

$$C = \exp[-2kd] - \Pi_e U^0_{ee}\exp[-2kd] - \Pi_e U^0_{eh}\exp[-kd] \tag{3.144}$$

$$D = 1-\Pi_e U^0_{ee} - \Pi_e U^0_{eh}\exp[-3kd] \tag{3.145}$$

We can write this in terms of only U^0_{ee}.

$$\begin{bmatrix} U_{ee} & -U_{eh}\exp[-kd] \\ -U_{eh}\exp[-kd] & U_{hh} \end{bmatrix} = \frac{U^0_{ee}}{1-\big(\Pi_e+\Pi_h\big)U^0_{ee} + \big(1-\exp[-4kd]\big)\Pi_e\Pi_h\big(U^0_{ee}\big)^2} \tag{3.146}$$

$$\times \begin{bmatrix} 1+\big(\exp[-4kd]-1\big)\Pi_h U^0_{ee} & \exp[-2kd] \\ \exp[-2kd] & 1+\big(\exp[-4kd]-1\big)\Pi_e U^0_{ee} \end{bmatrix}$$

3.8 Appendix: solution to the λ-integral for the bilayer geometry

The integral we need to compute is

$$\int_0^1 \frac{\lambda}{1-a\lambda+b\lambda^2}\big(c+f\lambda\big)d\lambda = \int_0^1 \left\{\frac{c\lambda}{1-a\lambda+b\lambda^2} + \frac{f}{b} + \frac{af\lambda/b - f/b}{1-a\lambda+b\lambda^2}\right\} d\lambda \tag{3.147}$$

for complex a, b, c, and f. To start, let's only consider the first term in the integrand. We first decompose it in terms of partial fractions. Assuming that $a^2 \neq 4b$,

$$\frac{c\lambda}{1-a\lambda+b\lambda^2} = \frac{A}{\lambda-\lambda_1} + \frac{B}{\lambda-\lambda_2} \tag{3.148}$$

where

$$\lambda_1 = \frac{a+\sqrt{a^2-4b}}{2b} \qquad \lambda_2 = \frac{a-\sqrt{a^2-4b}}{2b} \tag{3.149}$$

$$A = \frac{c\lambda_1}{2b\lambda_1 - a} \qquad B = \frac{c\lambda_2}{2b\lambda_2 - a} \tag{3.150}$$

Since λ_1 and λ_2 are complex, we need to make the denominators of (3.148) purely real. Multiplying by the denominators' complex conjugates, we get

$$\frac{c\lambda}{1-a\lambda+b\lambda^2} = \frac{A(\lambda-\bar{\lambda_1})}{\lambda^2-(\lambda_1+\bar{\lambda_1})\lambda+\lambda_1\bar{\lambda_1}} + \frac{B(\lambda-\bar{\lambda_2})}{\lambda^2-(\lambda_2+\bar{\lambda_2})\lambda+\lambda_2\bar{\lambda_2}} \tag{3.151}$$

where $\bar{x}$ is the complex conjugate of x. These integrals are in Gradshteyn & Ryzhik [80]:

$$\int_0^1 \frac{M\lambda+N}{O+2P\lambda+Q\lambda^2}d\lambda = \frac{M}{2Q}\ln|O+2P+Q| + \frac{NQ-MP}{Q\sqrt{OQ-P^2}}\arctan\left(\frac{Q+P}{\sqrt{OQ-P^2}}\right) \tag{3.152}$$

$$-\frac{M}{2Q}\ln|O| - \frac{NQ-MP}{Q\sqrt{OQ-P^2}}\arctan\left(\frac{P}{\sqrt{OQ-P^2}}\right) \quad OQ > P^2$$

$$= \frac{M}{2Q}\ln|O+2P+Q| + \frac{NQ-MP}{2Q\sqrt{OQ-P^2}}\ln\left(\frac{Q+P-\sqrt{P^2-OQ}}{Q+P+\sqrt{P^2-OQ}}\right) \tag{3.153}$$

$$-\frac{M}{2Q}\ln|O| - \frac{NQ-MP}{2Q\sqrt{OQ-P^2}}\ln\left(\frac{P-\sqrt{P^2-OQ}}{P+\sqrt{P^2-OQ}}\right) \quad OQ < P^2$$

$$= \frac{N-MP/Q}{P} - \frac{N-MP/Q}{P+Q} + \frac{M}{Q}\ln\left|1+\frac{P}{Q}\right| - \frac{M}{Q}\ln\left|\frac{P}{Q}\right| \quad OQ = P^2 \tag{3.154}$$

If $a^2 = 4b$,

$$\frac{c\lambda}{1 - a\lambda + b\lambda^2} = \frac{ac/(2b^2)}{\left(\lambda - a/(2b)\right)^2} + \frac{c/b}{\lambda - a/(2b)} \tag{3.155}$$

and

$$\int_0^1 \frac{c\lambda}{1 - a\lambda + b\lambda^2} d\lambda = -\frac{c}{b} - \frac{ca}{2b^2(1 - \frac{a}{2b})} + \frac{c}{b} \ln\left|1 - \frac{a}{2b}\right| - \frac{c}{b} \ln\left|\frac{a}{2b}\right| \tag{3.156}$$

The second term is trivial. Assuming $a^2 \neq 4b$, the third can be written as

$$\frac{af\lambda/b - f/b}{1 - a\lambda + b\lambda^2} = \frac{\tilde{A}}{\lambda - \lambda_1} + \frac{\tilde{B}}{\lambda - \lambda_2} \tag{3.157}$$

where

$$\tilde{A} = \frac{af\lambda_1/b - f/b}{2b\lambda_1 - a} \qquad \tilde{B} = \frac{af\lambda_2/b - f/b}{2b\lambda_2 - a} \tag{3.158}$$

We again multiply by the denominators' complex conjugates and use the same Gradshteyn & Ryzhik integrals. If $a^2 = 4b$,

$$\int_0^1 \frac{af\lambda/b - f/b}{1 - a\lambda + b\lambda^2} d\lambda = -\frac{af}{b} + \frac{2f}{a} - \frac{a^2 f/(2b^2) - f/b}{1 - a/(2b)} + \frac{af}{b} \ln\left|1 - \frac{a}{2b}\right| - \frac{af}{b} \ln\left|\frac{a}{2b}\right| \tag{3.159}$$

3.9 Appendix: fitting exchange-correlation free energies

Given exchange and correlation free energies F_{XC} at various densities $\{n_\alpha\}$, we seek the optimal fit function

$$F_{fit}(n; n_C) = \begin{cases} \sum_{j=0}^{N} a_j n^{j/2} & n < n_C \\ \sum_{j=N+1}^{2N+2} a_j (\ln n)^{j-N-1} & n \geq n_C \end{cases} \tag{3.160}$$

N is the order of both polynomials and n_C is the density cutoff, above which we fit the data using a polynomial of $\ln n$. By defining

$$c_j(n; n_C) = \begin{cases} n^{j/2} & j \leq N \text{ and } n < n_C \\ 0 & j \leq N \text{ and } n \geq n_C \\ 0 & j > N \text{ and } n < n_C \\ (\ln n)^{j-N-1} & j > N \text{ and } n \geq n_C \end{cases} \tag{3.161}$$

and $\vec{a}$ as our vector of desired fitting coefficients, (1) is more compactly written as

$$F_{fit}(n; n_C) = \vec{c}(n; n_C) \cdot \vec{a} \tag{3.162}$$

At n_C, we require the values and first derivatives of the polynomials to the left and right to be equal:

$$\sum_{j=0}^{N} a_j (n_C)^{j/2} = \sum_{j=N+1}^{2N+2} a_j (\ln n_C)^{j-N-1} \tag{3.163}$$

$$\frac{d}{dn}\left(\sum_{j=0}^{N} a_j (n)^{j/2}\right)_{n=n_C} = \frac{d}{dn}\left(\sum_{j=N+1}^{2N+2} a_j (\ln n)^{j-N-1}\right)_{n=n_C} \tag{3.164}$$

If we define

$$d_{1j} = \begin{cases} n_C^{j/2} & j \leq N \\ -(\ln n_C)^{j-N-1} & j > N \end{cases} \tag{3.165}$$

$$d_{2j} = \begin{cases} \frac{j}{2} n_C^{j/2-1} & j \leq N \\ -\frac{(j-N-1)}{n_C} (\ln n_C)^{j-N-2} & j > N \end{cases} \tag{3.166}$$

our constraints become

$$\vec{d_1} \cdot \vec{a} = 0 \tag{3.167}$$

$$\vec{d_2} \cdot \vec{a} = 0 \tag{3.168}$$

To minimize the squared residual error

$$\mathcal{E} = \sum_{\alpha=1}^{N_{\text{density}}} \left(F_{fit}(n_\alpha; n_C) - F_{XC}(n_\alpha)\right)^2 \tag{3.169}$$

subject to our constraints, we introduce two Lagrange multipliers, λ_1 and λ_2. Our Lagrangian is

$$\mathcal{L}(\{n_\alpha\}, n_C, \lambda_1, \lambda_2) = \sum_{\alpha=1}^{N_{\text{density}}} \left(F_{fit}(n_\alpha; n_C) - F_{XC}(n_\alpha)\right)^2 - \lambda_1 \vec{d_1} \cdot \vec{a} - \lambda_2 \vec{d_2} \cdot \vec{a} \tag{3.170}$$

To find $\vec{a}$ which minimizes $\mathcal{L}$, we set its derivative equal to 0:

$$\frac{\partial \mathcal{L}}{\partial a_i} = 0 \tag{3.171}$$

$$= 2 \sum_{\alpha=1}^{N_{\text{density}}} \left(F_{fit}(n_\alpha; n_C) - F_{XC}(n_\alpha)\right)^2) \left.\frac{\partial F_{fit}}{\partial a_i}\right|_{n=n_\alpha} - \lambda_1 d_{1i} - \lambda_2 d_{2i} \tag{3.172}$$

Note that

$$\left.\frac{\partial F_{fit}}{\partial a_i}\right|_{n=n_\alpha} = c_i(n_\alpha; n_C) \tag{3.173}$$

Let's define

$$\chi_{ij}^{-1} = 2 \sum_{\alpha=1}^{N_{\text{density}}} c_i(n_\alpha; n_C) c_j(n_\alpha; n_C) \tag{3.174}$$

and

$$b_i = 2 \sum_{\alpha=1}^{N_{\text{density}}} F_{XC}(n_\alpha) c_i(n_\alpha) \tag{3.175}$$

(3.172) becomes

$$\chi^{-1} \cdot \vec{a} = \vec{b} + \lambda_1 \vec{d_1} + \lambda_2 \vec{d_2} \tag{3.176}$$

so our desired coefficients are given by

$$\vec{a} = \chi \cdot \vec{b} + \lambda_1 \chi \cdot \vec{d_1} + \lambda_2 \chi \cdot \vec{d_2} \tag{3.177}$$

The Lagrange multipliers are determined by

$$0 = \vec{d_1} \cdot \vec{a} \tag{3.178}$$

$$= \vec{d_1} \cdot \chi \cdot \vec{b} + \lambda_1 \vec{d_1} \cdot \chi \cdot \vec{d_1} + \lambda_2 \vec{d_1} \cdot \chi \cdot \vec{d_2} \tag{3.179}$$

$$0 = \vec{d_2} \cdot \vec{a} \tag{3.180}$$

$$= \vec{d_2} \cdot \chi \cdot \vec{b} + \lambda_1 \vec{d_2} \cdot \chi \cdot \vec{d_1} + \lambda_2 \vec{d_2} \cdot \chi \cdot \vec{d_2} \tag{3.181}$$

If we define

$$g_{ij} = \vec{d_i} \cdot \chi \cdot \vec{d_j} \tag{3.182}$$

and

$$h_i = -\vec{d_i} \cdot \chi \cdot \vec{b} \tag{3.183}$$

we have

$$G \cdot \vec{\lambda} = \vec{h} \tag{3.184}$$

so

$$\vec{\lambda} = G^{-1} \cdot \vec{h} \tag{3.185}$$

Chapter 4

A tale of two phase transitions: the exciton Mott transition and EHL-gas transition in a bilayer geometry

4.1 Introduction

Equipped with exchange and correlation chemical potentials, we are finally in a position to investigate phase transitions. In Section 3.6, we showed chemical potentials for a collection of free electrons and holes and identified density regimes where the first derivative was negative. This is thermodynamically unstable [79], so the carriers stabilize by coexisting in a dilute gas phase and a condensed degenerate state. At this point, we could use a Maxwell equal-area construction to map EHL-gas phase diagrams in the plane of temperature and free carrier density n_{free}. However, at the low temperatures in consideration [42,43,45], we should expect a strong tendency for electrons and holes to associate as bound excitons. Therefore, we first solve the law of mass action to calculate α, the fraction of free carriers relative to the total number of carriers. This allows us to translate our phase diagrams to the plane of temperature and total density n_{tot}, which is more relevant to experiments as it is proportional to the laser power.

Below a critical temperature, the order parameter, α, suddenly changes as the density, n_{tot}, crosses some threshold value: this is the exciton Mott transition. Below a critical temperature and at high densities, indirect excitons begin to dissociate, provide improved screening for other excitons, and cause an "ionization avalanche." We find that the bilayer separation does not change the nature of this phase transition, but only the density and temperature scales where it occurs. This agrees with earlier theoretical studies on single and double quantum wells [81,82] as well as experimental studies on CQWs [34,83]. We find that the transition to the liquid phase is always heralded by the Mott transition. The impetus for both the exciton Mott and the EHL-gas transition is the exchange and correlation contributions of free degenerate electrons and holes. As charge-neutral species, excitons do

not participate in the transition to the condensed state; they just act as a reservoir that reduces the density of free carriers that truly drive the transition.

4.2 Methodology

The binding of electrons and holes into excitons may be described by the chemical reaction

$$e^- + h^+ \rightleftharpoons X \tag{4.1}$$

We only consider optical excitations, so the electron and hole densities are equal: $n_e = n_h = n_{free}$. At equilibrium, the chemical potentials for the free carriers and the bound excitons are equal:

$$\mu_{tot}^{free} = \mu_{tot}^{X} \tag{4.2}$$

where

$$\mu_{tot}^{free} = \mu_0^e + \mu_0^h + \mu_{exch}^{eh} + \mu_{cor}^{eh} + \mu_{cap}^{eh} \tag{4.3}$$

and

$$\mu_{tot}^{X} = \mu_0^X + \mu_{cap}^X \tag{4.4}$$

We neglect exchange and correlation effects for excitons. However, the exchange interaction is repulsive for bosons, and in Chapter 3 we saw that the energetic contributions due to exchange and correlation are similar in magnitude. Thus, neglecting these non-ideal effects is an acceptable approximation.

The ideal chemical potentials for electrons and holes in two dimensions is given by Eq. (3.105):

$$\mu_0^i(n_{free}, \beta) = \beta^{-1} \ln\big(\exp[n_{free}\lambda_i^2/(\nu_i\xi_i)] - 1\big) \tag{4.5}$$

We take $\nu_e = \nu_h = 1$ and $\xi_e = \xi_h = 2$. The exchange and correlation pieces were evaluated in Chapter 3. The capacitor energy is proportional to the total density of carriers, so $\mu_{cap}^{eh} = \mu_{cap}^X$ and this classical mean-field interaction does not influence the binding equilibrium. For non-interacting excitons in (quasi-)two dimensions, their chemical potential is given in Eq. (3.113).

$$\mu_0^X(n_X, \beta, d) = E_X(d) + \ln\big(1 - \exp[-n_X\lambda_i^2/(\nu_X\xi_X)]\big) \tag{4.6}$$

E_X is the exciton binding energy given in Eq. (2.5). We use $\xi_X = 4$ to include one singlet and three triplet states and $\nu_X = 1$.

Returning to Eq. (4.2), our law of mass action reads

$$\frac{1 - \exp[-n_X\lambda_X^2/(\nu_X\xi_X)]}{\big(\exp[n_{free}\lambda_e^2/(\nu_e\xi_e)] - 1\big)\big(\exp[n_{free}\lambda_h^2/(\nu_h\xi_h)] - 1\big)} = K \tag{4.7}$$

K is the equilibrium constant

$$K(n_{free}, \beta, d) \equiv \exp[-\beta\big(E_X(d) - \mu_{exch}^{eh}(n_{free}, \beta) - \mu_{cor}^{eh}(n_{free}, \beta, d)\big)] \tag{4.8}$$

In this form, we see that the exchange-correlation chemical potential reduces the exciton binding energy. Indeed, these non-ideal effects renormalize the band gap [33,84].

We now rewrite n_{free} and n_X in terms of the total carrier density n_{tot} and the ionization ratio $\alpha = n_{free}/n_{tot}$. The law of mass action becomes

$$\begin{aligned}&\frac{1-\exp[-n_{tot}(1-\alpha)\lambda_X^2/(\nu_X\xi_X)]}{\big(\exp[n_{tot}\alpha\lambda_e^2/(\nu_e\xi_e)]-1\big)\big(\exp[n_{tot}\alpha\lambda_h^2/(\nu_h\xi_h)]-1\big)}\\&=\exp[-\beta\big(E_X(d)-\mu_{exch}^{eh}(n_{tot}\alpha,\beta)-\mu_{cor}^{eh}(n_{tot}\alpha,\beta,d)\big)]\end{aligned} \tag{4.9}$$

When $n_{tot}\lambda_e^2 \ll 1$, we can Taylor expand the exponentials to derive the classical analog

$$\frac{(1-\alpha)\nu_e\xi_e\nu_h\xi_h}{\alpha^2 n_{tot}\lambda_{red}^2\nu_X\xi_X}=\exp[-\beta\big(E_X(d)-\mu_{exch}^{eh}(n_{tot}\alpha,\beta)-\mu_{cor}^{eh}(n_{tot}\alpha,\beta,d)\big)] \tag{4.10}$$

where

$$\lambda_{red}^2=\frac{2\pi\hbar^2\beta}{m_{red}} \tag{4.11}$$

In the context of plasmas, this classical law of mass action is called the Saha ionization equation [85].

Given β, n_{tot}, and d, we can solve Eq. (4.9) for α. However, we have found that there can be multiple solutions at high densities. The correct choice is the one that minimizes the system's free energy. The change in Helmholtz free energy due to carriers partitioning into free and bound states is given by

$$dF=\mu_{tot}^{free}dn_{free}+\mu_{tot}^{X}dn_X \tag{4.12}$$

$$=(\mu_{tot}^{free}-\mu_{tot}^{X})n_{tot}d\alpha \tag{4.13}$$

so

$$\frac{dF}{d\alpha}=(\mu_{tot}^{free}-\mu_{tot}^{X})n_{tot} \tag{4.14}$$

Integrating from some arbitrary reference value α_0 leads to

$$F(\alpha)=F(\alpha_0)+n_{tot}\int_{\alpha_0}^{\alpha}\big(\mu_{tot}^{free}(\tilde{\alpha})-\mu_{tot}^{X}(\tilde{\alpha})\big)d\tilde{\alpha} \tag{4.15}$$

Because the location of the minimum doesn't depend on $F(\alpha_0)$ or the factor of n_{tot}, these terms can be neglected.

The ionization ratio that minimizes the free energy is always the correct solution to the law of mass action, Eq. (4.9). Accordingly, the chemical potentials for the free carriers and bounds excitons are equal, so for the electron-hole-exciton system,

$$\begin{aligned}\mu_{tot}(n_{tot},\alpha,\beta,d)=&\,\mu_0^e(\alpha n_{tot},\beta)+\mu_0^h(\alpha n_{tot},\beta)+\mu_{exch}^{eh}(\alpha n_{tot},\beta)\\&+\mu_{cor}^{eh}(\alpha n_{tot},\beta,d)+\mu_{cap}^{eh}(n_{tot},d)\end{aligned} \tag{4.16}$$

After obtaining μ_{tot}, we identify the total carrier densities at which the liquid and gaseous phases coexist via standard Maxwell equal-area constructions [79].

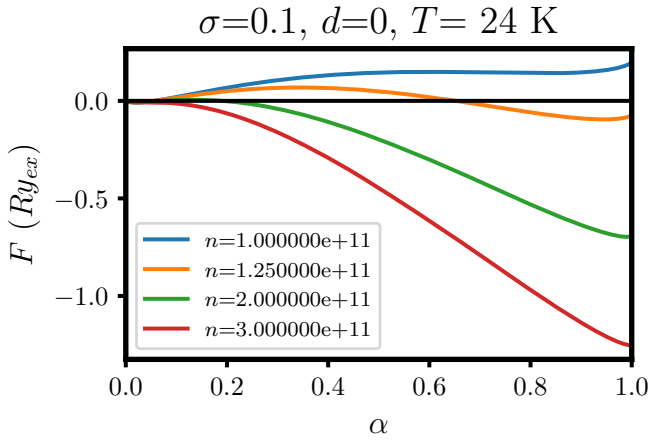

Figure 4.1: Free energy as a function of ionization ratio. The densities in the legend are in units of cm^{-2}. The Mott transition occurs near $n_{tot} \approx 1.25 \times 10^{11}$ cm^{-2}.

4.3 Results for the exciton Mott transition

In Figure 4.1 we show how the free energy varies with α for various densities. Around $n_{tot} \approx 1.25 \times 10^{11}$ cm $^{-2}$, the exciton Mott transition occurs and the free energy minimum suddenly jumps from 0 to 1. This abruptness is characteristic of a first-order phase transition.

In Figures 4.2 and 4.3, we show the fraction of free carriers α as a function of the total density n_{tot} for various temperatures, bilayer separations, and electron-hole mass ratios. Starting with Figure 4.2, we find that the order parameter, α, changes suddenly at n_{tot}=7.2×10^8 cm^{-2} for $T = 4$ K. In contrast, the transition to free carriers is more gradual at higher temperatures. Thus, the critical temperature for the exciton Mott transition at $d = 1.5\ a_{ex}$ and $\sigma = 0.1$ is approximately four Kelvin. A transition from bound excitons to a plasma still occurs above this value, but because the underlying free energy is not discontinuous with respect to n_{tot}, the transition is not first-order.

In the left panel of Figure 4.3, we plot α as a function of n_{tot} for three different bilayer separations. Because the capacitor term does not influence this binding equilibrium and μ_{cor} depends on d weakly, the dependence due to the bilayer separation is mostly contained in the exciton binding energy, $E_X(d)$. As d increases, the IX binding energy decreases which increases the fraction of free carriers for all values of n_{tot}. Similarly, since the critical density for the exciton Mott transition is approximately where the exchange and correlation chemical potentials equal the exciton binding energy, this critical value decreases as d increases.

In the right panel of Figure 4.3, we compare the effect of the electron-hole mass ratio. Recall that the exciton binding energy is independent of σ when expressed in Ry_{ex}. In contrast, the ideal, exchange, and correlation contributions to the chemical potential all have an explicit dependence on σ. Furthermore, as discussed in Chapter 3, the energy scale

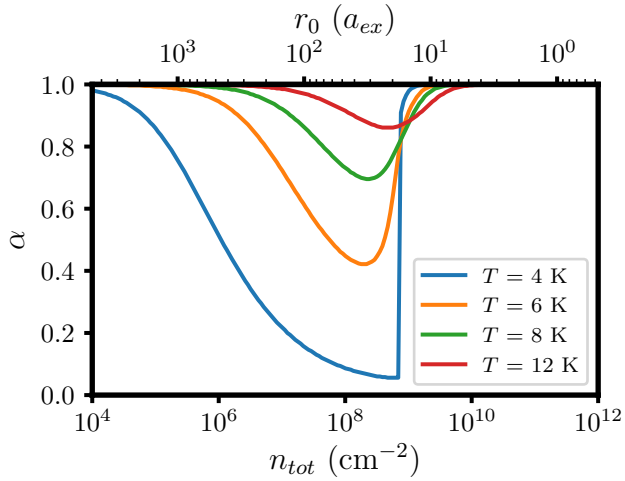

Figure 4.2: Ionization ratio as a function of total carrier density for $\sigma = 0.1$ $d = 1.5$ a_{ex}, and various temperatures.

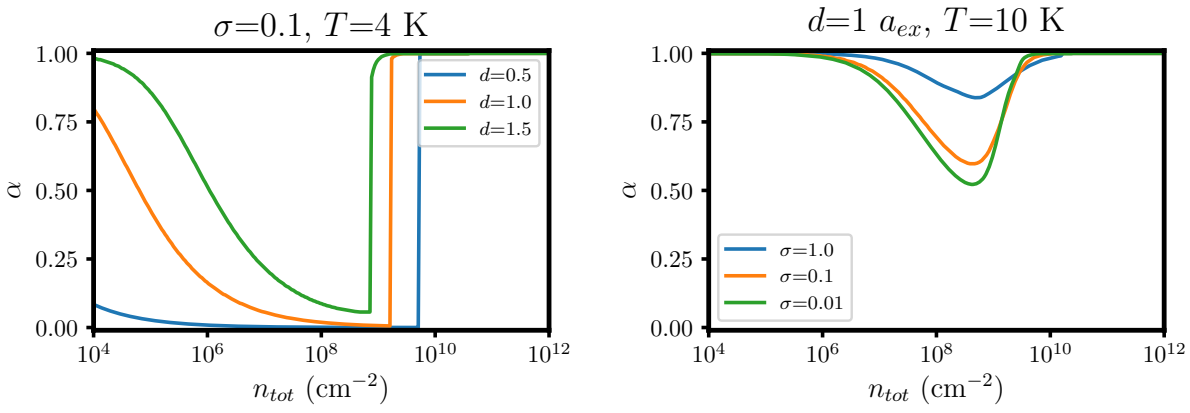

Figure 4.3: Ionization ratio as a function of total carrier density for $\sigma = 0.1$, T=4 K, and various bilayer separations and mass ratios.

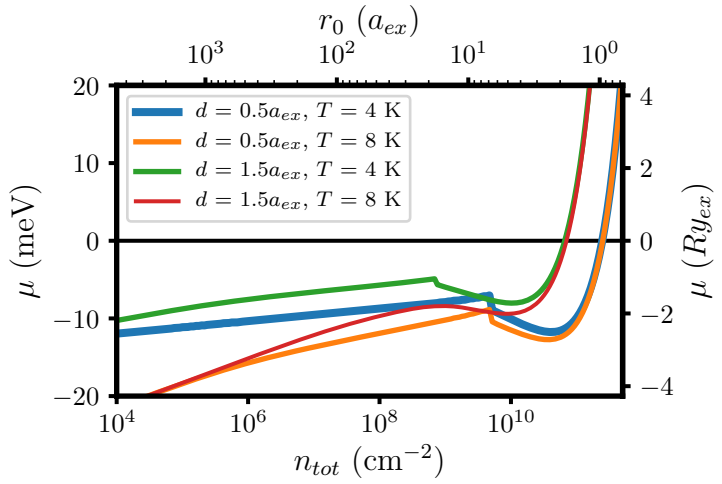

Figure 4.4: Total chemical potentials as a function of total carrier density.

(Ry_{ex}) increases and length scale (a_{ex}) decreases as the electron-hole mass ratio decreases. The major conclusion is that as σ decreases, carriers are more likely to be bound in an IX for intermediate densities.

Figure 4.4 shows chemical potentials for the electron-hole-exciton system, μ_{tot}, as a function of total carrier density for various d and T. In the low-density, classical regime, μ_{tot} is dictated by the ideal contributions given by Eq. (3.106) and which are independent of d. In the high-density, degenerate regime, the capacitor's contribution given by Eq. (3.135) overtakes the ideal, exchange, and correlation contributions. Thus, μ_{tot} is entirely determined by d.

The kinks observed in the green, blue, and orange curves are caused by the exciton Mott transition. Immediately after this transition, the chemical potential does not obey the stability criterion given in Eq. (3.137); in this immediate density regime, the exchange and correlation contributions dominate over the ideal and capacitor contributions. To resolve this instability, the system phase separates into a low- and high-density phase. The low-density phase contains a mixture of free carriers and excitons while the high-density phase consists only of unbound electrons and holes.

4.4 Results for the EHL-gas phase transition

If the chemical potentials, μ_{tot}, disobey the stability criterion $\big($Eq. (3.137)$\big)$, we can use Maxwell equal-area constructions to identify the coexistence densities of the liquid and gaseous phases. Figure 4.5 show the resulting phase diagrams in the T–n_{tot} plane for $\sigma = 0.1$ and three different bilayer separations. As the bilayer separation increases, the electron-hole-

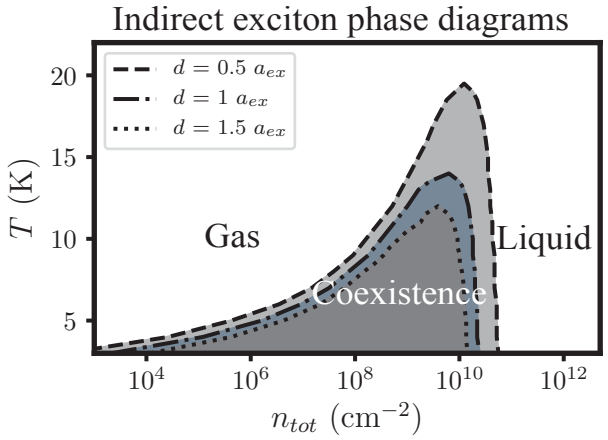

Figure 4.5: Liquid-gas phase diagrams for $\sigma = 0.1$

exciton system destabilizes due to the capacitor's contribution to the chemical potential. This leads to smaller values of the critical temperature, T_C as well as the critical density, n_C.

The experiments of Bar-Joseph and co-workers used coupled quantum wells with $d = 1.5$ a_{ex} and $\sigma = 0.1$. They measured a critical temperature of approximately five Kelvin. Taking into consideration the approximations we have made to calculate these phase diagrams (*e.g.* the isotropic effective mass approximation, using a single-band model, and the random-phase approximation), our estimate of $T_C = 12$ K agrees rather well.

Figures 4.6 summarizes the effect of the bilayer separation on the critical point for the EHL-gas transition. The left panel shows how T_C varies with d, and the right panel shows how n_C varies with d. We also include three different electron-hole mass ratios. In analogy to how a biexciton is stabilized as σ deviates from unity, the electron-hole liquid is stable at higher temperatures as σ decreases from one.

In this Chapter, we synthesized the results of Chapters 2 and 3 to investigate the exciton Mott transition in addition to the phase behavior of the electron-hole liquid. Using the exciton binding energies calculated in Chapter 2 and the exchange and correlation free energies from Chapter 3, we first solved the law of mass action in order to take into account the association equilibrium between free carriers and bound excitons. At temperatures below a critical value and at large densities, we observed the exciton Mott transition, when bound IXs suddenly dissociate. While there is a quantitative dependence on the bilayer separation, we found that the nature of this transition is independent of the geometry. Then, given the fraction of free carriers, we calculated chemical potentials for the electron–hole–exciton system and found regimes in which μ_{tot} violated thermodynamic stability. Using Maxwell equal-area constructions, we mapped the phase diagram for the EHL-gas transition for various bilayer separations.

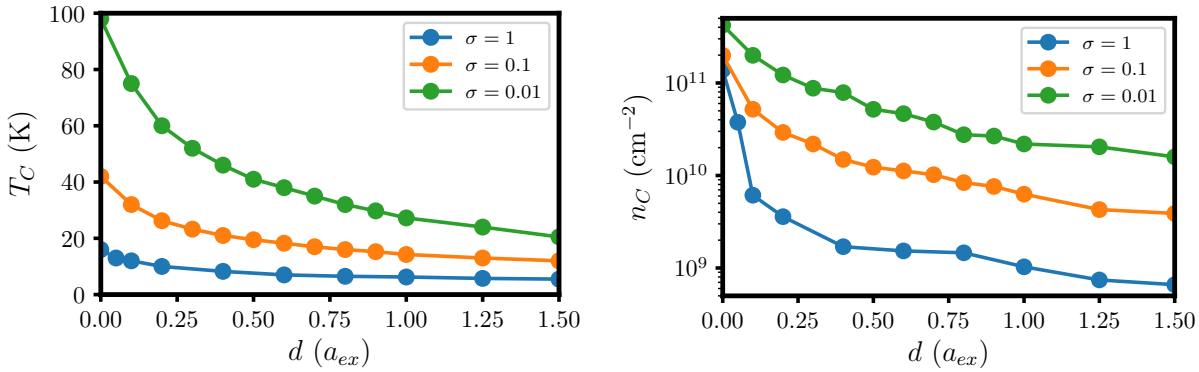

Figure 4.6: Critical temperature and critical density as a function of bilayer separation. Three different electron-hole mass ratios σ are shown.

Bibliography

[1] G. D. Scholes and G. Rumbles. *Nat. Mat.* **5**, 683 (2006).

[2] J. P. Wolfe. *Physics Today* **35**, 46 (1982).

[3] B. J. Schwartz. *Nat. Mat.* **7**, 427 (2008).

[4] T. Mirkovic, E. E. Ostroumov, J. M. Anna, R. van Grondelle, Govindjee, and G. D. Scholes. *Chem. Rev.* 117, 249 (2017).

[5] D. Jérome, T. M. Rice, and W. Kohn. *Phys. Rev.* **158**, 462 (1967).

[6] Y. F. Lu, H. Kono, T. I. Larkin, A. W. Rost, T. Takayama, A. V. Boris, B. Keimer, and H. Takagi. *Nat. Commun.* **8**, 1 (2017).

[7] T. Meng, Y. Zheng, D. Zhao, H. Hu, Y. Zhu, Z. Xu, S. Ju, J. Jing, X. Chen, H. Gao, K. Yang, T. Guo, F. Li, J. Fan, and L. Qian. *Nat. Photonics* **16**, 297 (2022).

[8] B. A. Gregg. *J. Phys. Chem. B* **107**, 4688 (2003).

[9] H. Tsai, W. Nie, J. C. Blancon, C. C. Stoumpos, R. Asadpour, B. Harutyunyan, A. J. Neukirch, R. Verduzco, J. J. Crochet, S. Tretiak, L. Pedesseau, J. Even, M. A. Alam, G. Gupta, J. Lou, P. M. Ajayan, M. J. Bedzyk, M. G. Kanatzidis, and A. D. Mohite. *Nature* **536**, 312 (2016).

[10] H. Goodwin, T. C. Jellicoe, N. J. L. K. Davis, and M. L. Böhm. *Nanophotonics* **7**, 111 (2018).

[11] M. T. Sajjad, A. Ruseckas, and I. D. W. Samuel. *Matter* **3**, 341 (2020).

[12] H. Kim, S. Z. Uddin, N. Higashitarumizu, E. Rabani, and A. Javey. *Science* **373**, 448 (2021).

[13] J. C. Kim, D. R. Wake, and J. P. Wolfe. *Phys. Rev. B* **50**, 15099 (1994).

[14] K. W. Stone, K. Gundogdu, D. B. Turner, X. Li, S. T. Cundiff, and K. A. Nelson. *Science* **324**, 1169 (2009).

[15] A. Esser, E. Runge, R. Zimmermann, and W. Langbein. *Phys. Rev. B* **62**, 8232 (2000).

[16] A. Von Lehmen, D. S. Chemla, J. E. Zucker, and J. P. Heritage. *Opt. Lett.* **11**, 609 (1986).

[17] C. Uihlein, D. Fröhlich, and R. Kenklies. *Phys. Rev. B* **23**, 2731 (1981).

[18] A. L. Fetter and J. D. Walecka. *Quantum Theory of Many-Particle Systems* (Dover Publications, Inc., 2003).

[19] J. M. Blatt, K. W. Böer, and W. Brandt. *Phys. Rev.* **126**, 1691 (1962).

[20] W. C. Stwalley and L. H. Nosanow. *Phys. Rev. Lett.* **36**, 910 (1967).

[21] D. G. Fried, T. C. Killian, L. Willmann, D. Landhuis, S. C. Moss, D. Kleppner, and T. J. Greytak. *Phys. Rev. Lett.* **81**, 3811 (1998).

[22] L. V. Butov, A. C. Gossard, and D. S. Chemla. *Nature* **418**, 751 (2002).

[23] C. W. Lai, J. Zoch, A. C. Gossard, and D. S. Chemla. *Science* **303**, 503 (2004).

[24] N. F. Mott. *Rev. Mod. Phys.* **40**, 677 (1968).

[25] L. V. Keldysh, in *Proceedings of the Ninth International Conference on the Physics of Semiconductors, Moscow, 1968*, edited by S. M. Ryvkin and V. V. Shmastsev (Nauka, Leningrad, 1968), pp. 1303.

[26] C. D. Jeffries. *Science* **189**, 955 (1975).

[27] A. E. Almand-Hunter, H. Li, S. T. Cundiff, M. Mootz, M. Kira, and S. W. Koch. *Nature* **506**, 471 (2014).

[28] V. M. Asnin and A. A. Rogachev. *JETP Lett.* **9**, 248 (1969).

[29] G. A. Thomas, T. M. Rice, and J. C. Hensel. *Phys. Rev. Lett.* **33**, 219 (1974).

[30] A. F. Dite, V. D. Kulakovsii, and V. B. Timofeev. *Sov. Phys. JETP* **45**, 604 (1977).

[31] J. P. Gourley and P. L. Wolfe. *Phys. Rev. Lett.* **40**, 526 (1977).

[32] L. V. Keldysh, *Contemp. Phys.* **27**, 395 (1986).

[33] A. Rustagi and A. F. Kemper. *Nano Lett.* **18**, 455 (2018).

[34] M. Stern, V. Garmider, V. Umansky, and I. Bar-Joseph. *Phys. Rev. Lett.* **100**, 256402 (2008).

[35] M. Okada, A. Kutana, Y. Kureishi, Y. Kobayashi, Y. Saito, T. Saito, K. Watanabe, T. Taniguchi, S. Gupta, Y. Miyata, B. I. Yakobson, H. Shinohara, and R. Kitaura. *ACS Nano* **12**, 2498 (2018).

[36] L. H. Fowler-Gerace, D. J. Choksy, and L. V. Butov. *Phys. Rev. B* **104**, 165302 (2021).

[37] J. J. Su and A. H. MacDonald. *Phys. Rev. B* **95**, 045416 (2017).

[38] R. A. Suris. *JETP* **122**, 602 (2016).

[39] J. Schleede, A. Filinov, M. Bonitz, and H. Fehske. *Contrib. Plasma Phys.* **52**, 819 (2012).

[40] M. M. Fogler, L. V. Butov, and K. S. Novoselov. *Nat. Commun.* **5**, 1 (2014).

[41] B. Laikhtman and R. Rapaport. *Phys. Rev. B* **80**, 195313 (2009).

[42] M. Stern, V. Umansky, and I. Bar-Joseph. *Science* **343** 55, (2014).

[43] S. Misra, M. Stern, A. Joshua, V. Umansky, and I. Bar-Joseph. *Phys. Rev. Lett.* **120**, 047402 (2018).

[44] Y. Furukawa and M. Nakayama. *Phys. Status Solidi C* **13**, 101 (2016).

[45] V. Timofeev, A. Larionov, M. Grassi-Alessi, M. Capizzi, and J. M. Hvam. *Phys. Rev. B* **61**, 8420 (2000).

[46] N. N. Sibeldin. *Phys.-Usp.* **60**, 1147 (2017).

[47] M. L. Cohen and S. G. Louie. *Fundamentals of Condensed Matter Physics* (Cambridge University Press, 2016).

[48] M. S. Hybertsen and S. G. Louie. *Phys. Rev. B* **34**, 5390 (1986).

[49] M. Rohlfing and S. G. Louie. *Phys. Rev. Lett.* **81**, 2312 (1998).

[50] J. P. Philbin and E. Rabani. *J. Phys. Chem. Lett.* **11**, 5132 (2020).

[51] D. Jasrasaria and E. Rabani. *Nano Lett.* **21**, 8741 (2021).

[52] S. Refaely-Abramson, F. H. da Jornada, S. G. Louie, and J. B. Neaton. *Phys. Rev. Lett.* **119**, 267401 (2017).

[53] M. H. Szymanska and P. B. Littlewood. *Phys. Rev. B* **67**, 193305 (2003).

[54] R. Zimmermann and C. Schindler. *Solid State Commun.* **144**, 395 (2007).

[55] C. Schindler and R. Zimmermann. *Phys. Rev. B* **78**, 045313 (2008).

[56] R. M. Lee, N. D. Drummond, and R. J. Needs. *Phys. Rev. B* **79**, 125308 (2009).

[57] I. V. Bondarev and M. R. Vladimirova. *Phys. Rev. B* **97**, 165419 (2018).

[58] S. Okumura and T. Ogawa. *Phys. Rev. B* **65**, 035105 (2002).

[59] M. Y. J. Tan, N. D. Drummond, and R. J. Needs. *Phys. Rev. B* **71**, 033303 (2005).

[60] T. Kato. *Commun. Pure Appl. Math.* **10**, 151 (1957).

[61] R. T. Pack and W. Byers Brown. *J. Chem. Phys.* **45**, 556 (1966).

[62] R. J. Needs, M. D. Towler, N. D. Drummond, P. López Ríos, and J. R. Trail. *J. Chem. Phys.* **152**, 154106 (2020).

[63] D. ter Haar. *Problems in Quantum Mechanics* (Academic Press, Inc., 1960).

[64] P. J. Reynolds, D. M. Ceperley, B. J. Alder, and W. A. Lester, Jr. *J. Chem. Phys.* **77**, 5593 (1982).

[65] A. Szabo and N. S. Ostlund. *Modern Quantum Chemistry* (Dover Publications, Inc., 1996).

[66] T. H. Dunning. *J. Chem. Phys.* **190**, 1007 (1988).

[67] R. Pauncz. *Spin Eigenfunctions* (Plenum Press, 1979).

[68] W. F. Brinkman and T. M. Rice. *Phys. Rev. B* **7**, 1508 (1973).

[69] A. Inagaki and S. Katayama. *J. Phys. Soc. Japan* **72**, 1452 (2003).

[70] T. Chakraborty and P. Pietilainen. *Phys. Rev. Lett.* **49**, 1034 (1982).

[71] M. Combescot and P. Nozieres. *J. Phys. C: Solid State Phys.* **5**, 2369 (1972).

[72] G. D. Mahan. *Many-Particle Physics* (Springer Science, 2000).

[73] J. Hubbard. *Proc. R. Soc. London. A* **243**, 336 (1957).

[74] P. Nozieres and D. Pines. *Phys. Rev.* **111**, 442 (1958).

[75] K. S. Singwi, M. P. Tosi, R. H. Land, and A. Sjölander. *Phys. Rev.* **176**, 589 (1968).

[76] S. Phatisena, R. E. Amritkar, and P. V. Panat. *Phys. Rev. A* **34**, 5070 (1986).

[77] F. Stern. *Phys. Rev. Lett.* **18**, 546 (1967).

[78] Y. Kuramoto and H. Kamimura. *J. Phys. Soc. Jpn.* **37**, 716 (1974).

[79] D. Chandler. *Introduction to Modern Statistical Mechanics* (Oxford University Press, 1987).

[80] I. S. Gradshteyn and I. M. Ryzhik. *Table of Integrals, Series, and Products* (Academic Press, 2007).

[81] V. V. Nikolaev and M. E. Portnoi. *Superlattices Microstruct.* **43**, 460 (2008).

[82] D. Snoke. *Solid State Commun.* **146**, 73 (2008).

[83] G. Kiršanske, P. Tighineanu, R. S. Daveau, J. Miguel-Sánchez, P. Lodahl, and S. Stobbe. *Phys. Rev. B* **94**, 155438 (2016).

[84] H. Kalt and M. Rinker. *Phys. Rev. B* **45**, 1139 (1992).

[85] M. N. Saha. *London, Edinburgh, Dublin Philos. Mag. J. Sci.* **40**, 472 (1920).

[86] F. Perrot and M. W. C. Dharma-Wardana. *Phys. Rev. A* **30**, 2619 (1984).